

NORTHWESTERN UNIVERSITY

Novel *In Situ* Molecular Lubrication Strategies for Controlling Friction, Wear, and  
Contamination

SUBMITTED TO THE GRADUATE SCHOOL  
IN PARTIAL FULFILLMENT OF THE REQUIREMENTS

for the degree

DOCTOR OF PHILOSOPHY

Field of Mechanical Engineering

by

Blake Johnson

EVANSTON, ILLINOIS

December 2017

## Abstract

Most lubricants contain a series of additives that reduce friction and wear, and protect contacting surfaces. The design of these additives must be modernized to meet the challenges involved with high operating temperatures, extreme environmental conditions, and increasingly stringent environmental regulations. This research demonstrates three novel lubricant additive strategies that have been developed and tested in order to address contemporary tribological demands. The additives are molecularly engineered to undergo a specific set of chemical reactions *in situ*, or within the tribological environment, producing a reactant material that is beneficial to lubrication. The findings are a result of a collaborative effort from experts in mechanical engineering, chemistry, and materials science. The first additive is an organosilver molecule that breaks down at high temperatures, depositing lubricious metallic silver on contacting surfaces. The additive successfully maintained lubricity at high temperatures, after the lubricating fluids thermally failed. The next is an organosilane molecule that reacts with external contaminants in the lubricant, successfully reducing contaminant particle agglomeration and mitigating wear. The additive was specially designed, and its interaction with silica was analyzed. Then, the additive successfully reduced spikes in friction and wear due to sand contamination. The final additive is a precursor molecule for carbon tribofilms, which breaks down to during contact to form lubricious graphitic carbon near contacting surfaces. Friction and wear were greatly reduced under a variety of conditions because of the lubricious carbon tribofilms.

## Acknowledgements

I would like to personally thank my friends and colleagues from Northwestern University, who have made this work possible through their guidance, discussion, and encouragement. I would like to especially thank Michael Desanker, Hongxing Wu, Dr. Christina Twist, Dr. Max Delferro, Dr. Xingliang He, and Matt Ford. I would also like to thank my committee members, including my advisor Prof. Q. Jane Wang, as well as Prof. Tobin Marks, and Prof. Yip-Wah Chung, for their guidance and support.

This work was generously supported by the US National Science Foundation (Grant No. CMMI-1662606) and Northwestern University (the McCormick Research Catalyst Awards Fund Grant No. 10038293). Support is also acknowledged from the National Priorities Research Program (NPRP grant no. 5-192-1-046) from the Qatar National Research Fund (a member of the Qatar Foundation), and the U.S. Army Tank-Automotive and Armaments Command (TACOM contract no. W56HZV-09-0341). This work made use of the Keck-II Facility of Northwestern University's NUANCE Center, which has received support from the Keck Foundation, the Soft and Hybrid Nanotechnology Experimental (SHyNE) Resource (NSF ECCS-1542205), the Materials Research Center (NSF DMR-1121262), the McCormick Research Catalyst Awards Fund, Grant No. 10038293, and the International Institute for Nanotechnology (IIN) at Northwestern University. Purchases of the NMR and ESI-MS instrumentation at IMSERC were supported by the National Science Foundation (CHE-1048773 and CHE-0923236, respectively). Microscopy studies made use of the EPIC facility (NUANCE Center-Northwestern University), which has received support from the MRSEC program (NSF DMR-1121262) at the Materials Research Center, and the Nanoscale Science and Engineering Center (EEC-0118025/003), both programs of the National Science Foundation, the State of Illinois, and Northwestern University. Assistance in sample preparation and spectroscopy has been kindly given by Hongxing Wu, Dr. Carla Shute (MatCI), and Dr. Xinqi Chen. (NUANCE).

Dedicated to Dr. Myron Horn

**Table of Contents**

Abstract.....	2
Acknowledgements.....	3
List of Figures.....	6
List of Tables .....	10
Chapter 1: Introduction.....	11
1.1 Background and Motivation .....	11
1.2 Tribology Fundamentals.....	12
1.3 Research Overview .....	18
Chapter 2: Organosilver Solid Lubricant Precursor Molecules.....	21
2.1 Introduction.....	21
2.2 Materials and Methods.....	24
2.3 Results and Discussion .....	28
2.4 Chapter 2 Conclusions .....	43
Chapter 3: Organosilane Sand Dispersant .....	44
3.1 Introduction.....	44
3.2 Materials and Methods.....	46
3.3 Results and Discussion .....	55
3.4 Chapter 3 Conclusions .....	64
Chapter 4: Novel Carbon Tribofilm Additive.....	66
4.1 Introduction.....	66
4.2 Materials and Methods.....	71
4.3 Results and Discussion .....	80
4.4 Chapter 4 Conclusions .....	110
Chapter 5: Conclusions.....	111
Chapter 6: Future Work .....	113
6.1 Organosilver Solid Lubricant Precursor Molecule.....	113
6.2 Organosilane Sand Dispersant .....	113
6.3 Novel Carbon Tribofilm Additive .....	113
References.....	115
Author Vita .....	129

## List of Figures

Figure 1: The Stribeck curve, which demonstrates the three lubrication conditions, and their relation to friction. ....	12
Figure 2: Flow chart for the collaborative effort between mechanical engineering, chemistry, and materials science for novel lubricant additive design, formulation, testing, assessment, and application. ....	20
Figure 3:(a–c) Molecular structures of silver precursor lubricant additives. (d) Molecular structure of current generation-IV silver–pyrazolate additive. ....	23
Figure 4: Diagram outlining the experimental procedure for organosilver solid lubricant precursor. ....	24
Figure 5: Schematic of temperature-controlled CETR UMT-2 ball-on-disk tribometer with used for temperature ramp friction and wear tests. ....	25
Figure 6: (a) Crystal structure of the additive. Hydrogen atoms are omitted for clarity. (b) Molecular packing in the additive. Hydrocarbon chains are omitted for clarity. Intermolecular Ag-Ag distance= 3.216 Å. (c) Side view and (d) top view of crystal packing. ....	28
Figure 7: (a) Thermogravimetric analysis trace for the Gen. III and IV additives. The weight loss data were recorded at the ramp rate of 5 °C min <sup>-1</sup> and a 90 mL min <sup>-1</sup> N <sub>2</sub> flow rate. (b) NMR spectra of the additive before and after 1 hr heating at 275 °C, showing no change in molecular structure. ....	30
Figure 8: Vial of pure PAO4 (left) and a 5 wt % solution of the in PAO4 (right), which shows a yellow tint and no insoluble material. ....	31
Figure 9: Ball-on-disk measurements of friction with increasing loadings of the silver precursor additive in (a) PAO and (b)FF oil. Each data point is the average of a temperature ramp experiment from 180 °C to 350 °C over 30 mins. The red line shows baseline friction for pure PAO and FF oil. ....	32
Figure 10: Ball-on-disk tribometer tests with lubricated contact for 2.5 wt % loading of the additive in (a) PAO4 and (b) FF oil. Temperature is ramped from 180 to 350 °C over 30 minutes. The red line shows baseline friction for pure PAO and FF oil. ....	33
Figure 11: Wear rate measurements for the temperature-ramped ball-on-disk tribometer substrates for 1 in (a) PAO4 and (b) Fully formulated oil. White light interferometry is used to measure the volume of the wear scar at 12 positions, and the volumes for each wear scar are then averaged. The red line shows baseline friction for pure PAO and FF oil. ....	35
Figure 12: Energy dispersive spectroscopy (EDS) on the (a) outside of the post-test wear scar and (b) the inside of the wear scar. ....	36
Figure 13: SEM image (top) and EDS map (bottom) of a silver agglomeration next to a piece of wear debris. ....	37
Figure 14: SEM image (top) and EDS map (bottom) of the area inside a wear scar with deep scars from asperity contact. ....	38
Figure 15: SEM image (top) and EDS map (bottom) at the edge of the wear scar. ....	39

Figure 16: High magnification SEM image (top) and EDS map (bottom) of the silver particles within the wear scar.....	40
Figure 17: The tribochemical reaction and lubrication mechanism for the silver precursor additive. (a) The additive mixes with the lubricant oil and enters the tribological system. (b) The heat and pressure of asperity contact induce thermolysis of the additive, releasing metallic silver. (c) The low shear strength silver is spread across the surface, reducing friction and wear. .	42
Figure 18: The reaction that converts the hydroxyl groups surrounding sand particles with long hydrocarbon chains, thus mitigating the effects of sand contamination in a tribological environment. ....	46
Figure 19: Diagram outlining the experimental procedure for organosilane sand surfactant. Blue boxes indicate physical experiments while green boxes indicate simulations and calculations. ....	47
Figure 20: Configuration of the MD simulation, featuring two silica slabs grafted with hydrocarbon chains. ....	49
Figure 21: The cumulative size distribution of medium and coarse grade sand (a), and (b) the chemical constituents of sand. ....	50
Figure 22: Organosilane additives for sand particle contamination control with 10 and 18 carbon chain lengths. ....	51
Figure 23: The reaction between the additive and the oxide surface of silica that forms a siloxane film on sand particle surfaces.....	53
Figure 24: The MD model calculating repulsive force vs. distance curves (a) and total repulsive energies (b) for various hydrocarbon chain lengths of the organosilane molecule grafted to silica. ....	56
Figure 25: Visual difference between PAO4, PAO4 with sand particles, and PAO4 with sand particles and the additive package. ....	57
Figure 26: FTIR (a) and TGA (b) results for pure silica and silica mixed with the additive and catalyst. The peaks for Alkyl and OH features change after the reaction occurs, suggesting a successful reaction, and only the reacted silica experiences weight loss during heating. ....	58
Figure 27: Wear results for disks lubricated with the pure PAO4 and contaminated PAO4 with and without the additives, using medium (a) and coarse (b) grade sand. ....	60
Figure 28: Average friction results for pure PAO4 and contaminated PAO4 with and without the additives, using medium grade sand (a) and coarse grade sand (b). ....	61
Figure 29: DLS measurements of the average particle size of 1 wt % of medium grade sand in PAOs with and without the C18 additive. Measurements were taken in one minute intervals. ....	63
Figure 30: Viscosity of pure PAO and contaminated PAO, with and without the C18 additive, at room temperature (a) and 90°C (b). ....	64
Figure 31: The bonds directions and crystalline structure of (a) sp <sup>3</sup> - and (b) sp <sup>2</sup> -bonded carbon <sup>120</sup> . ....	67

Figure 32: Diagram outlining the experimental procedure for carbon the tribofilm additive. Blue boxes indicate physical experiments while green boxes indicate simulations and calculations. ....	71
Figure 33: CPCa molecule containing a metastable carbon ring (cyclopropane) as the carbon source and a surface-active group (-COOH) that provides adsorption to the surface. ....	72
Figure 34: Picture of PAO4 and PAO4 + 2.5 wt % CPCa after sitting for 48 hours. No phase separation was observed. ....	73
Figure 35: Shear stress (a) and dynamic viscosity (b) of PAO4 influenced by strain rate with and without the addition of 2.5 wt % CPCa. ....	74
Figure 36: Characteristic peaks for Raman spectroscopy of carbon species, and how shifts in the peak can indicate properties of the peaks.....	77
Figure 37: Illustration of the EA $\mu$ R functioning with the carbon precursor additive.....	78
Figure 38: Wear rates for tests using PAO4 and PAO4+CPCa as lubricants, and a comparison of wear rates averaged over all 20 tests using these two lubricants.....	80
Figure 39: Time-averaged coefficient of friction for tests using PAO4 and PAO4+CPCa as lubricants, and a comparison of friction coefficients averaged over all 20 tests using these lubricants.....	81
Figure 40: Friction-time curves, showing initial rapid friction reduction (a-b), in the presence of CPCa, and in some cases, followed by sudden friction increase, as noted in (c) and (d). ....	82
Figure 41: Friction and wear results from the 2-stage test. Disk A was lubricated with PAO4 for both stages, Disk B was lubricated with PAO4 + 2.5 wt % CPCa for stage 1, and pure PAO4 for stage 2.....	83
Figure 42: Interpolated maps of (a) friction and (b) wear results based on tests using PAO4+CPCa. ....	85
Figure 43: (a) Occurrence of tribofilm failure using PAO4+CPCa at certain speed-load combinations, with an overlay of the contact load ratio. (b) Wear rate vs. contact load ratio. Note the constant wear rate for $L_c$ between 5 and 95 %. ....	86
Figure 44: Optical micrograph obtained from the disk surface after tribotesting at 10 N and 200 mm s <sup>-1</sup> with PAO4+CPCa.....	87
Figure 45: Raman spectra obtained from the untested disk surface, the wear scar, a commercial DLC film, and the colored deposit in the wear track.....	88
Figure 46: Surface roughness of various regions on the post-test surface.....	89
Figure 47: Nanoindentation curves obtained from the disk surface and the carbon tribofilm. ....	90
Figure 48: SEM image of the post-test disk, lubricated with PAO4 and PAO4+CPCa. ....	91
Figure 49: SEM image of the graphitic carbon tribofilm on the post-test surface. ....	92
Figure 50: (a) SEM image of the post-test disk showing the carbon film filling in crevices and growing near scratches.....	93
Figure 51: SEM image with a closer view of the carbon tribofilm growth near the rougher scratch on the post-test surface.....	94

Figure 52: (a) SEM image of the post-test disk showing the smearing of the film along direction of sliding. ....	95
Figure 53: SEM images of dispersed graphitic nanosheets researched as an EP additive <sup>122</sup> (a) compared to the nanoscale carbon flakes present on the post-test disks (b). ....	96
Figure 54: Cross-sectional SEM image of a post-test disk surface etched away using FIB milling, revealing the dark carbonaceous regions on the steel surface, with the protective palladium overlayer. The elemental analysis line scan for carbon is included across the surface boundaries. ....	97
Figure 55: Raman spectra obtained from ball surfaces after testing with PAO4+CPCa. ....	98
Figure 56: Optical micrographs of the ball surface after testing with PAO4+CPCa test at 15 N and 100 mm s <sup>-1</sup> (a) before the jump in friction, and (b) immediately after the jump in friction. ....	99
Figure 57: (a) Raman results for the steel EAμR samples that were processed using no lubricant and lubricants with and without CPCa. (b) Microscope images of the microchannels for each sample. ....	100
Figure 58: Surfaces and Raman spectroscopy after experiencing motionless contact at 100 °C for 30 minutes, with and without 20 N downward pressure. ....	101
Figure 59: TGA (a) with MS (b) results for PAO4 + 2.5 wt % CPCa. ....	103
Figure 60: Mechanism of carbon formation from CPCa. (a) CPCa molecules adsorb on mating surfaces, (b) high flash temperature and pressure trigger tribochemical reaction that produces the carbon tribofilm, and (c) soft carbon tribofilm filling in the surface roughness. ....	104
Figure 61: An example (3N, 200mm s <sup>-1</sup> ) of the COF-time curve that demonstrates the difference between the PAO4 and PAO4 + CPCa samples attributed to carbon tribofilm formation. ....	106
Figure 62: Arrhenius plot of the natural log of the growth rate against the inverse of the absolute temperature, for the 10 N tests performed with disks polished to different roughnesses. ...	108
Figure 63: (a) Arrhenius plots of the natural log of growth rate against the inverse of temperature for different loads; (b) Variation of activation energy for carbon tribofilm formation versus contact pressure. ....	109

**List of Tables**

Table 1: Projected Global Economic and Emissions Savings from Tribological Solutions <sup>8</sup> .....	11
Table 2: Test conditions for the silver precursor additive heat-ramp tribological tests.....	27
Table 3. Formulations of lubricant samples for sand contamination tests.....	52
Table 4: Tribometer Test Conditions for the organosilane additive. ....	54
Table 5: Tribometer Test Conditions for the carbon tribofilm additive .....	75

## Chapter 1: Introduction

### 1.1 Background and Motivation

Tribology is the study of the phenomena that occur at the site of interfaces of interacting surfaces experiencing contact and relative motion. The overall goal of tribological research is to understand how interfacing materials behave from the nano to macro scale, and how this understanding can be applied to develop technologies that improve friction, wear, reliability, and the overall effectiveness in mechanical systems. Tribology has been essential to human civilization throughout history, from the first man-made machines, through the invention of the internal combustion engine, and beyond<sup>1</sup>. Successful lubrication is crucial to modern industries for reliability, repair costs, machine down time, oil consumption, and CO<sub>2</sub> emission<sup>1-5</sup>. Improvements in tribology enable robust new mechanical systems in automotive applications, manufacturing, green energy, and more<sup>6</sup>. It has been reported that 1-1.4 % of an industrialized nation's gross national product can be saved through research and implementation of new lubrication technology, which would also lead to dramatic reductions in prices CO<sub>2</sub> emissions<sup>7-8</sup>. Global projections of the consequences of these savings are shown in Table 1.

Table 1: Projected Global Economic and Emissions Savings from Tribological Solutions<sup>8</sup>.

	<i>5-10 years</i>	<i>15-25 years</i>
<i>Emissions reduction [Tons of CO<sub>2</sub>]</i>	<b>290 million</b>	<b>960 million</b>
<i>Economic Savings [\$]</i>	<b>226 billion</b>	<b>748 billion</b>

## 1.2 Tribology Fundamentals

### 1.2.1 Lubrication Regimes

Lubrication regimes are used to define the characteristic behavior of a tribological system. Lubrication system performance is mainly influenced by the viscosity of the fluid, the speed of relative motion, and the average pressure due to the normal load. The relationship between the coefficient of friction and these factors, in the form of the Hersey number, are classified into lubrication regimes described by the Stribeck curve, shown in Figure 1<sup>9</sup>.

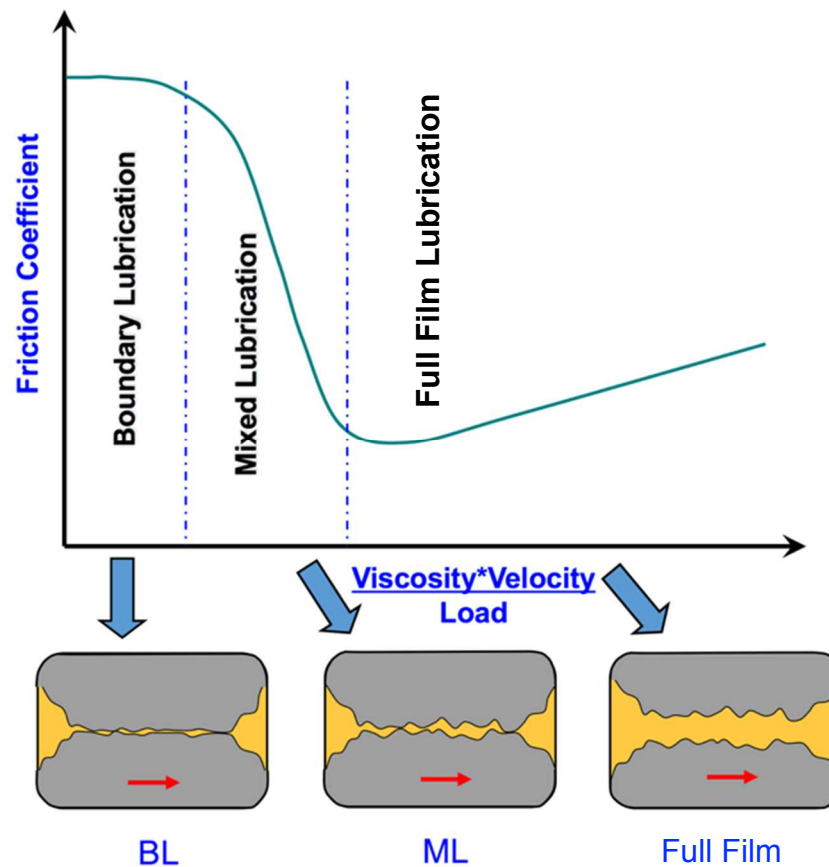


Figure 1: The Stribeck curve, which demonstrates the three lubrication conditions, and their relation to friction.

Under ideal operating conditions, lubricating fluids work by forming a continuous film that hydrodynamically supports the load between mating surfaces. The surfaces may exhibit some elastic deformation, but almost no wear if designed properly. This condition is known as full-film lubrication. During low speed, or under severe loading, the lubricant fails to form a continuous fluid film between mating surfaces, and asperities on the mating surfaces come into direct contact. This condition is known as boundary lubrication (BL). BL is dominated by microscopic contact and wear of asperities due to rubbing in relative motion. Increased roughness of the mating surfaces strongly promotes BL due to increased asperity contact. Phenomena in BL are still not well understood, because it is difficult to quantify influencing factors (i.e. heat, asperity interaction, wear, tribochemistry, catalysis) and isolate these factors experimentally<sup>10-11</sup>. Mixed Lubrication (ML) is the transition regime between BL and the full film lubrication, where some of the load is supported by the fluid and some by solid contact. High flash temperatures, plastic deformation, crystal structure changes, stress-promoted thermochemistry, thermionic emission, and exposure of catalytic nascent metal have all been observed within during BL and ML conditions<sup>12-17</sup>. There is no consensus on a fundamental model for how all of these phenomena interact and influence friction and wear<sup>1</sup>. The development of atomic force microscopy (AFM) has revealed fascinating insights into the physical phenomena of contact, but conclusions are still limited by the small size and time scale of AFM<sup>18-19</sup>. Archard's Law<sup>20</sup>, a well-known methodology for predicting wear based on sliding conditions and surface properties, often fails to predict the wear under ML and BL conditions<sup>21</sup>. Overall, BL and ML are the most challenging targets for friction and wear reduction, and lubrication design for modern machines is focused increasingly on this endeavor<sup>22-23</sup>. Research on BL and ML conditions is especially relevant for hybrid vehicles, which

often experience BL and ML conditions due to low engine speeds and frequent engine stopping each time the drivetrain switches to and from battery power. Many modern vehicles also implement ‘Start-Stop’ automation, a feature that automatically shuts the engine off when the vehicle idles<sup>24-25</sup>.

### **1.2.2 Vehicle Engine Lubrication**

Transportation, which accounts 70 % of petroleum consumption in the US, is an application of special interest in the field of tribology, because of its ubiquity<sup>26-27</sup>. Each 1 % improvement in fuel economy of light-duty vehicles lowers fuel consumption by 100,000 barrels of oil per day in the US<sup>28</sup>. Engine and drive train components involve dozens of sliding surfaces that are lubricated to reduce friction and wear. Modern lightweight and fuel-efficient engines demand increasingly high temperatures, speeds, and pressures compared to older generation engines, and next-generation lubricants must be capable of handling exceedingly severe conditions. Operation during extreme-conditions is also beneficial in emergency and combat situations<sup>23, 29</sup>.

Vehicle engine lubricants typically consist of a base fluid combined with 10-15 % of lubricant additives by weight. The base fluid is typically a synthetic or mineral oil containing olefins of assorted lengths and cross-linkings. A large variety of additive molecules are used to serve different purposes, including friction and wear reduction, anti-oxidation, viscosity modification, particle dispersion, and more. In addition to instant performance enhancement, additives protect the lubricant and mating surfaces over time from changes due to oxidization, contamination, and many other factors that potentially damage or degrade performance<sup>30</sup>. BL and ML conditions often

exhibit temperatures above 180 °C, at which point hydrocarbons in the base fluid are susceptible to degradation via thermolysis and oxidation. This leads to unwanted changes in viscosity, and third-body wear of surfaces<sup>31</sup>, and also releases carcinogenic polycyclic aromatic hydrocarbons through the engine exhaust<sup>32</sup>. Many additives also face challenges from environmental regulations due to hazardous reactivity<sup>33</sup>. Despite the enhancement and protection from lubricant additives, some degradation is inevitable, and engine oils must still be routinely replaced in order to maintain effectiveness and prevent permanent damage to the vehicle. When designing a lubricant formulation, one must consider if any of the additives interfere with the base oil or the function of other additives. Therefore, additives generally must have very good oil-solubility, and additives that can function in low concentrations with minimal reactivity or interaction with other chemicals are desirable.

The current research focuses on three classes of lubricant additives that are especially important to lubricant performance in BL and ML conditions, friction modifiers (FM), extreme pressure (EP) additives, and dispersants. FM additives are used to reduce friction at moderate to high loads. Most FM additives are molecules consisting of a polar moiety attached to a long hydrocarbon chain<sup>34-35</sup>. During lubrication, the polar head adsorbs on metal surfaces. The surface activity and small size of FM molecules allows them to reach areas with the nanoscale roughness grooves of the surface, where base oil hydrocarbons cannot reach<sup>36</sup>. The hydrocarbon chains coating the surface help the film-forming capabilities of the lubricant, and also exhibit anti-compressive behavior by creating a buffer between the asperities of mating surfaces<sup>37</sup>. Dispersants are lubricant additives designed to sequester and remove contaminants or neutralize their abrasive characteristics.

Contaminant particles from oxidation, wear, or external sources significantly reduce the service life of lubricants and tribological surfaces<sup>38</sup>. The friction and wear mechanisms of contamination vary depending on operating conditions and the chemical, thermal, and mechanical properties of the contaminants involved<sup>39</sup>. Three-body abrasion occurs when particles are pressed between mating surfaces, causing plastic deformation and sub-surface stress concentrations. Hard particles can also become embedded in surfaces and scratch the interfacing surface<sup>40</sup>. This is known as embedded two-body abrasion. Two-body abrasion is generally more severe than three-body abrasion, because embedded particles are not free to slide or rotate in between the mating surfaces<sup>41</sup>. Erosion occurs when a pressure gradient within the fluid induces relative motion of particles that impact and damage surfaces<sup>42</sup>. Insoluble contaminant particles can also influence lubricant viscosity, and therefore hinder the performance<sup>43</sup>. Dispersants must be carefully selected in order to optimally combat the expected contaminants in a tribological system. Extreme-pressure (EP) additives are a class of additives designed specifically to protect surfaces and lower friction when contact pressure and temperature become severe. EP additives usually function by chemically reacting with the metal surfaces, forming a lubricious sacrificial film. Zinc dialkyl-dithio-phosphates (ZDDP) is an especially effective and popular EP additive, though its use has been increasingly discouraged due to environmental concerns<sup>33</sup>. During operation, tribological energy breaks ZDDP down, forming a strong, smooth, and lubricious phosphate material in the areas of asperity contact<sup>18</sup>. Though its lubrication mechanisms are not fully understood<sup>1</sup>, researchers have determined that ZDDP activation occurs at around 200 °C and is heavily dependent on shear stress and the catalytic effect of worn down nascent metal<sup>44-45</sup>. Upon breakdown of the ZDDP, a highly viscous organometallic coating forms on the surface and

eventually reaches a steady-state thickness due to continual shear-induced removal and thermally-induced reformation. Such a coating also acts as an anti-oxidant by covering exposed nascent metal surfaces that would otherwise promote oxidation<sup>19</sup>.

### 1.2.3 Tribochemistry and Tribofilms

Reactions between a lubricant and surfaces under BL and ML conditions are referred to as tribochemical reactions. Tribochemical reactions are caused primarily by shear stress, normal stress, and frictional heat<sup>46</sup>. Other factors like catalysis and electron emission also play a role<sup>12</sup>. Fundamental knowledge of tribochemistry is limited and largely empirical, because it is difficult to observe the site of contact<sup>1</sup>. Most conventional lubricant additives are designed around secondary chemical interactions, such as van der Waals forces and hydrogen bonding, and do not consider the stronger covalent and ionic bonds that can arise from tribochemistry. However, through careful selection of lubricant additives, tribochemical reactions can be designed to form specific reactants at the site of contact *in situ*, or during machine operation. Although EP additives often make use of tribochemical reactions during BL conditions, this concept has other untapped benefits in the field of tribology<sup>47</sup>. For example, a major constraint of conventional additives is that they must be oil-soluble so as to not precipitate or agglomerate in engine oils over long periods of storage. This problem can be circumvented using tribochemistry. An oil-soluble precursor molecule can be mixed into engine oil, and during machine operation, the molecule can undergo tribochemical change that releases an oil-insoluble reactant into the fluid or onto the contact surfaces.

Because they occur locally at the site of contact, tribochemical reactions often result in a thin solid film generated on contact surfaces known as a tribofilm. Tribofilm formation involves complex mechanical, chemical, and thermodynamic phenomena that incorporate the surface materials, lubrication, and other environmental species<sup>9</sup>. A tribofilm was first reported in literature in 1958, when an “organic deposit” was observed on palladium contact surfaces<sup>48</sup>. At the time, the film was considered a nuisance, but tribofilms have since been proven to be a crucial tool for friction and wear reduction<sup>49-52</sup>. Many tribofilm-forming lubricant additives are presently used to form smooth layers on surfaces that reduce friction and wear and protect surfaces from oxidation and corrosion. Because they may be generated as a result of frictional energy near roughened asperity contact zones, tribofilms tend to be generated exactly where surface damage is most severe. This localized formation at the site of severe contact may be likened to white blood cells in the body, which seek out areas of biological infection and mitigate the problem at the source. To continue the biological analogy, tribofilm growth can also be likened to the ability of blood platelets to collect near wounds and mend the body. When a tribofilm precursor is added to a worn-out mechanical system, tribofilm formation can build up on the worn contact area and recondition the surface.

### **1.3 Research Overview**

The present research investigates three lubricant additives that are molecularly engineered to utilize tribochemistry for unprecedented performance in friction, wear, and contamination control. The additives serve as oil-soluble precursor molecules that undergo *in-situ* tribochemical transformation into reactants that are helpful to the lubricant. Two of the additive concepts focus

on novel approaches for the generation of lubricious tribofilms, and a third is designed to mitigate lubricant dust contamination.

Lubricant additive design is achieved through a collaborative process that requires knowledge from a variety of fields, including mechanical engineering, chemistry, and materials science. The research methodology for this work is presented in Figure 2. First, concepts are developed through discussion in a multi-disciplinary team, and the initial chemical formulations for a new additive concept are produced. The formulation of a new set of additives is confirmed separately through several characterization techniques. Once confirmed, the additives are mixed into an array of lubricant formulations, and tribological studies are performed. These studies include tests and analyses of friction and wear, viscometry, and surface mechanical and tribochemical properties. Post-test analysis reveals more insight into the additive performance, including nanoscale surface morphology, lubricant properties, and tribochemical phenomena. After the team is satisfied with the performance and characteristics of the additive, the research moves forwards to new and useful applications.

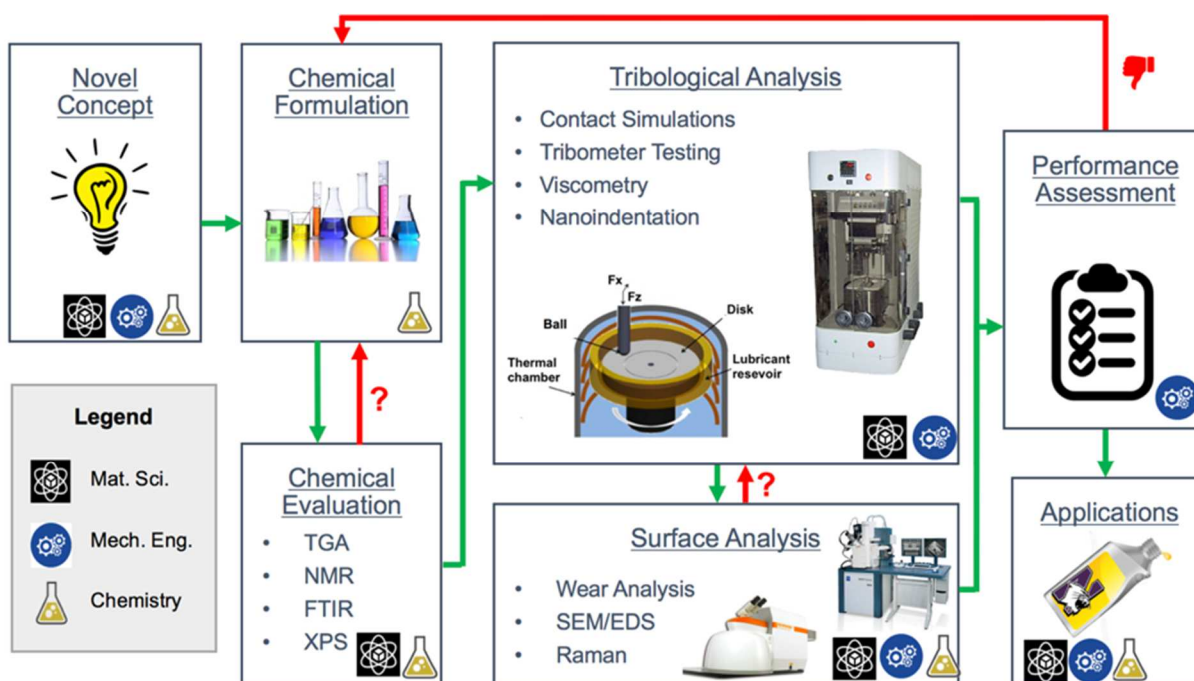


Figure 2: Flow chart for the collaborative effort between mechanical engineering, chemistry, and materials science for novel lubricant additive design, formulation, testing, assessment, and application.

## Chapter 2: Organosilver Solid Lubricant Precursor Molecules

### 2.1 Introduction

In automotive engines, the temperature at the surfaces of critical components reach 100-300 °C, and asperity contact can generate flash temperatures of 300-1000 °C, lasting microseconds<sup>29</sup>. High pressure and flash temperature in contact zones can easily plastically deform or wear away mating surfaces and cause chemical reactions that permanently alter the surfaces and lubricants<sup>46</sup>. Conventional lubricants are susceptible to degradation via thermolysis and oxidation. Furthermore, harsh external conditions or cooling system insufficiency can worsen the degradation of lubricants<sup>31, 53</sup>. A variety of lubricant additives are used in engine oils to reduce the thermal degradation of oil or mitigate its effect through supplemental lubrication<sup>54</sup>.

Solid lubricants, applied either as a surface coating, or suspended in a fluid, are known to maintain effectiveness at high temperatures<sup>55</sup>. Soft noble metals are effective solid lubricants because of their low reactivity, ductility, and low shear strength, which allow the formation of a smooth and lubricious glaze layers on surfaces in contact<sup>56</sup>. Silver coatings on contact surface have demonstrated friction and wear reduction at temperatures up to 750 °C<sup>57-61</sup>. Silver nanoparticles suspensions have been shown to increase surface fatigue life, decrease friction and wear, and work synergistically with other lubricant additives<sup>62-66</sup>. However, soft metal lubricants are generally not utilized in modern engine oils for a variety of reasons. Metal particles suspended in oil typically have poor solubility and agglomerate in storage or during operation<sup>54</sup>. Surface coatings are difficult to replace when damaged, as compared to replacing the lubricant fluid. Also, surface coatings can become embedded with wear debris that will scratch the mating surface<sup>67</sup>. An alternative strategy

for the delivery of lubricious silver is to use an oil-soluble silver precursor molecule as an additive in the lubricating fluid. The precursor molecule consists of a silver molecular core functionalized with a hydrocarbon shell that ensures proper dispersion in oil. The molecule is designed to undergo thermolysis at a designated temperature, depositing a layer of lubricious metallic silver onto contact surfaces. Marks et al. developed three generations of silver precursor molecules and tested their performance as extreme temperature additives in motor oil<sup>68-70</sup>. The gen. I and II additives (Figure 3a-b) demonstrated promising wear reduction in fully formulated (FF) engine oil around 200 °C. However, these molecules contain phosphorus (P) and sulfur (S) atoms, which are undesirable in lubricant additives due to environmental concerns<sup>33</sup>. The Gen. III additive (Figure 3c) is a pyrazole-pyridine complex that has the advantage of being P- and S-free, making it safe for use in automotive systems. However, it requires high loadings (> 20 %) for effective wear and friction reduction, and requires a surfactant in order to be adequately suspended in base oil<sup>71-73</sup>.

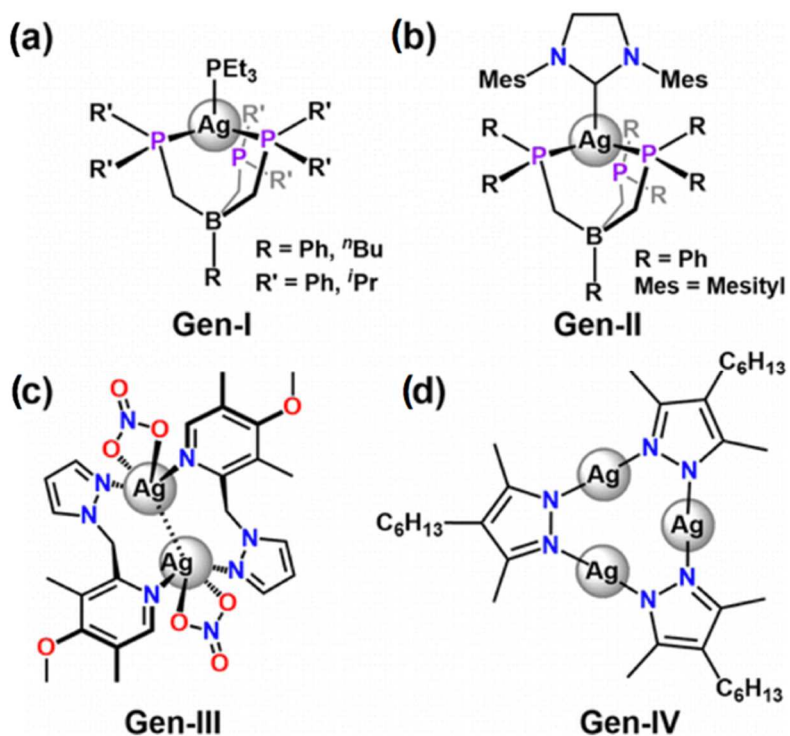


Figure 3:(a–c) Molecular structures of silver precursor lubricant additives. (d) Molecular structure of current generation-IV silver–pyrazolate additive.

For the next generation of the silver precursor additive, lower loadings of these molecules were necessary to reduce costs, ensure solubility, and leave space for other additives in the additive package<sup>74</sup>. The newest generation of the silver precursor additive is a P- and S- free silver-pyrazole molecule functionalized with long alkyl chains (Figure 3d). The addition of a third silver atom in the pyrazole core, compared to the two silver atoms in Gen. III, is intended to increase density of silver in the tribochemical deposition, and the hydrocarbon chains are intended to increase the additive's solubility in oil, improving the additive's dispersion in the lubricant.

## 2.2 Materials and Methods

The silver precursor additive molecule consists of a silver-containing pyrazole core functionalized with three 6-carbon alkane chains to improve oil solubility. The molecule was formulated, characterized, underwent tribological testing, and its performance was analyzed. The experimental methodology for this process is outlined in Figure 4 and described in the following sections.

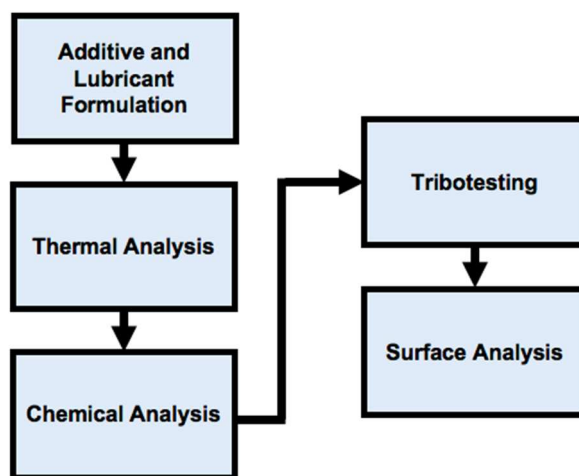


Figure 4: Diagram outlining the experimental procedure for organosilver solid lubricant precursor.

### 2.2.1 Additive and Lubricant Formulation

The silver pyrazole complex was synthesized using a condensation reaction between a pyrazole molecule and silver oxide in methanol<sup>75</sup>. The completed additive molecule was fully characterized using X-ray diffraction (XRD), thermogravimetric analysis (TGA), nuclear magnetic resonance spectroscopy (NMR). The additive was combined with polyalphaolefin (PAO4) and fully-formulated 15W-40 (FF) oils. PAO4 is a commonly used base fluid for commercial engine oils, and the FF oil used is a military grade oil with a standard additive package. For formulation, the

additive was dissolved in the minimal amount of hexane (1.0 mL/ 1.0 g silver additive) and then added to the oils to achieve additive concentrations of 1.0, 2.5, and 5.0 wt %. The oil–silver additive mixtures were stirred with a magnetic stir bar for 30 minutes to ensure homogeneity. Adding the additive to either oil creates a cloudy suspension at 25°C that dissolves fully with heating to 40°C and magnetic stirring.

### 2.2.2 Tribological Investigation

Temperature-ramped ball-on-disk tribological tests were performed to assess friction and wear performance while simulating boundary lubrication in an engine valve train. A schematic of the ball-on-disk tribometer (CETR UMT-2 Tribometer) used in this study is given in Figure 2. A ball made of M50 bearing steel with 62 HRC hardness was used to apply a vertical load ( $F_z$ ) to a 52100 steel disk with 50 HRC hardness, and the friction force ( $F_x$ ) is measured throughout testing. The roughness ( $R_q$ ) of the contacting surfaces was about 30 nm, measured using a Zygo NewView 7100 white-light interferometer (WLI) and SPIP surface analysis software. The surface of the disk was coated with a 2 mL of the lubricant sample before testing.

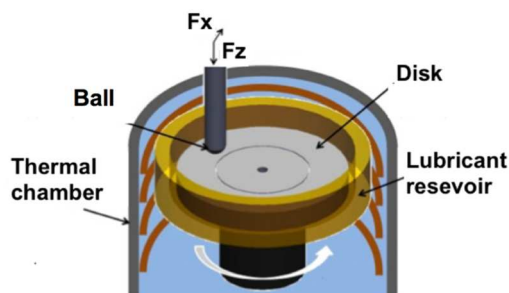


Figure 5: Schematic of temperature-controlled CETR UMT-2 ball-on-disk tribometer with used for temperature ramp friction and wear tests.

The testing temperature range (180-350 °C) refers to the surface temperature of the lower rotating disk in the tribometer, where the heating element in the testing chamber and thermal sensor are located. The increasing temperature simulates the failure of the oil above its thermal limit, and test the silver additive's continued performance at high temperatures. The temperature range was chosen to simulate a temperature transition for a typical -interface in an engine. The modeling of engine tribology<sup>30</sup> reveals that the temperature of valve train components may reach about 200°C under normal conditions. The tests were designed to start below this temperature value, at 180°C, and then ramp up to 350°C. Even though the overall testing temperature starts below the decomposition temperature of the additive complex, asperity contacts are expected to induce flash temperatures sufficient to cause silver deposition throughout the test. An established tribological model<sup>76</sup> was used to calculate the possible flash temperature based on the theory of a moving heat source over a semi-infinite solid<sup>77</sup> with considerations of asperity contact, heat conduction through the surfaces, and convection through fluid flow. This analysis revealed a flash temperature increase of 246 °C above the ambient temperature.

Table 2: Test conditions for the silver precursor additive heat-ramp tribological tests.

<b>Test Parameter</b>	<b>Value</b>
Applied load (N)	25
Hertzian Contact Pressure (GPa)	2.15
Disk rotation speed (rpm)	200
Radial location of contact (mm)	20
Sliding contact speed (m/s)	0.42
Total sliding distance (m)	754
Base oil	PAO4 15W-40
Additive concentration (wt %)	0.0, 1.0, 2.5, 5.0
Temperature range (°C)	180-350
Rate of temperature change (°C/s)	0.1
Test duration (min)	30

### 2.2.3 Surface Analysis

Upon completion of the friction tests, the disks were sonicated in a hexane bath to remove oil residue. The volume of the wear scar was then measured using WLI. Energy-dispersive x-ray spectroscopy (EDS) on Hitachi S4800-II and Hitachi SU8030 scanning electron microscopes (SEMs) was used to examine the morphology of the disk surface and deposited silver content.

## 2.3 Results and Discussion

### 2.3.1 Additive Synthesis and Characterization

The silver additive was fully characterized by XRD and NMR spectroscopy. The crystallographic results reveal that the pyrazolate ligands and silver ions in the additive form a 9-membered ring structure, with each  $\text{Ag}^+$  ion coordinated to two nitrogen centers (Figure 3a). An intermolecular interaction with a bond distance of 3.216 Å is observed, leading to a staggered ladder stacking involving adjacent molecules in the crystal structure (Figure 3b)<sup>75</sup>.

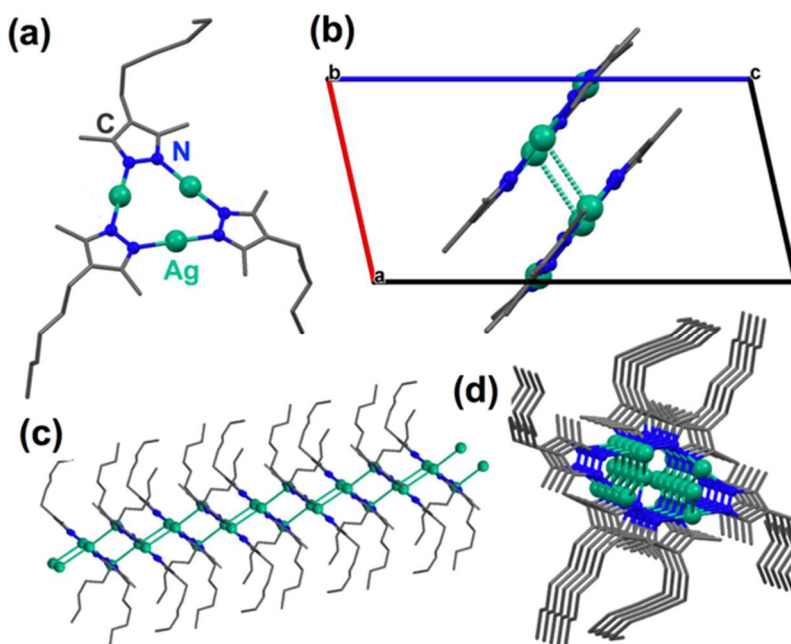


Figure 6: (a) Crystal structure of the additive. Hydrogen atoms are omitted for clarity. (b) Molecular packing in the additive. Hydrocarbon chains are omitted for clarity. Intermolecular Ag-Ag distance= 3.216 Å. (c) Side view and (d) top view of crystal packing.

### 2.3.2 Silver Additive Thermolysis

TGA was performed under nitrogen gas to evaluate the temperature at which thermolysis begins, and the residue produced by thermolysis was then analyzed by NMR. It was found that the additive begins to undergo thermolysis at  $\sim 300$  °C, which is a more desirable thermolysis temperature than the  $\sim 200$  °C of Gen-III additive (Figure 7a)<sup>68, 70</sup>. Ramping temperature experiments have shown that the PAO4 and FF oil used as base oils in these experiments starts to decompose at 275 °C. At the completion of a TGA scan, 38.5 % of the original mass remains. Elemental analysis shows that the additive is 38.02 wt % silver, which means that a majority of the residue remaining after thermolysis (38.5 %) is silver metal. The thermal stability of the additive was also investigated in a hydrocarbon solution by NMR, since this additive is designed for applications in motor oil. An NMR sample in toluene heated at 275 °C for 1 hour shows no changes in structure (Figure 7b), indicating that the additive is stable under this condition.

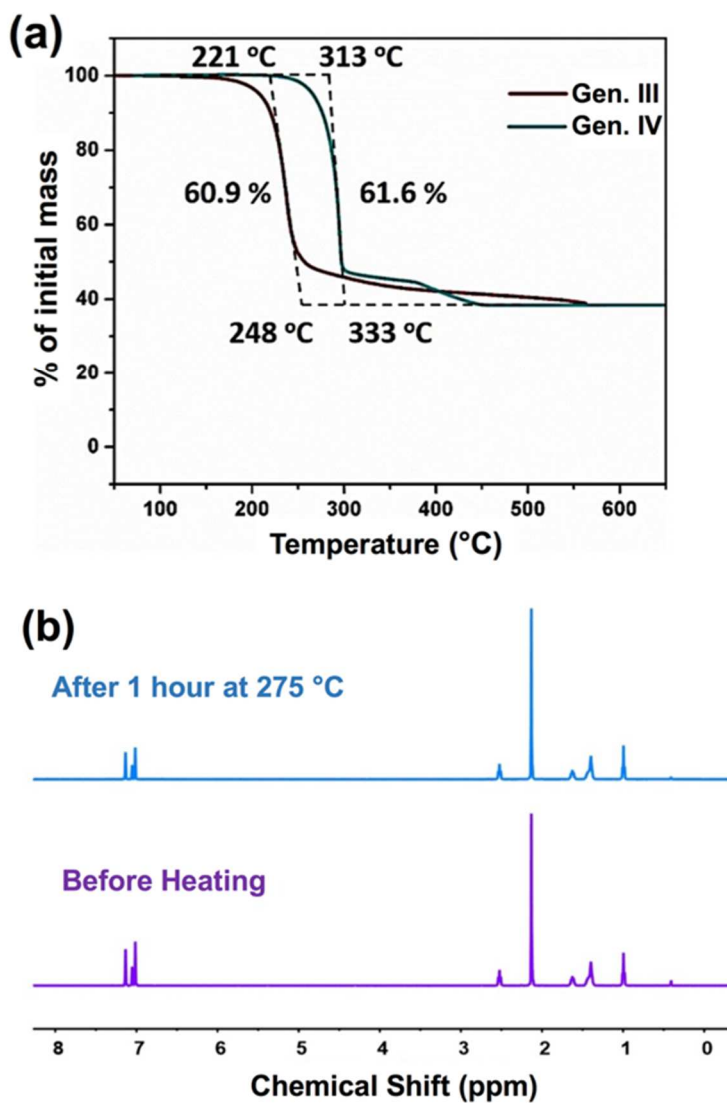


Figure 7: (a) Thermogravimetric analysis trace for the Gen. III and IV additives. The weight loss data were recorded at the ramp rate of  $5\text{ }^{\circ}\text{C min}^{-1}$  and a  $90\text{ mL min}^{-1}$   $\text{N}_2$  flow rate. (b) NMR spectra of the additive before and after 1 hr heating at  $275\text{ }^{\circ}\text{C}$ , showing no change in molecular structure.

### 2.3.3 Solubility of Additive in Base Oil

Heating of the 5 wt % loading of the silver precursor additive at 40 °C in PAO4 yielded a homogeneous solution (Figure 8). Solubility in base oil was a challenge for previous generations of silver-organic additives<sup>70</sup>. The aforementioned Gen. III additive yielded promising results, but large loadings were required (20 wt %) it formed a cloudy, opaque mixture in oil.



Figure 8: Vial of pure PAO4 (left) and a 5 wt % solution of the in PAO4 (right), which shows a yellow tint and no insoluble material.

### 2.3.4 Friction and Wear Behavior

The effects of differing concentrations in PAO4 and FF oil were investigated by ball-on-disk tribometer measurements (Figure 9). The ball-on-disk tribometer was used to ensure that the additive did not have detrimental effects on the coefficient of friction (COF). Figure 9 shows that 1.0, 2.5 and 5 wt % loadings of the additive all reduce friction. A 2.5 wt % loading reduces friction by 20 % in PAO4 and by 30 % in FF oil. Loadings greater than 2.5 wt % do not decrease friction further. A similar friction-additive concentration relationship is also observed in the studies of previous generations of the silver additives.<sup>69-70</sup>

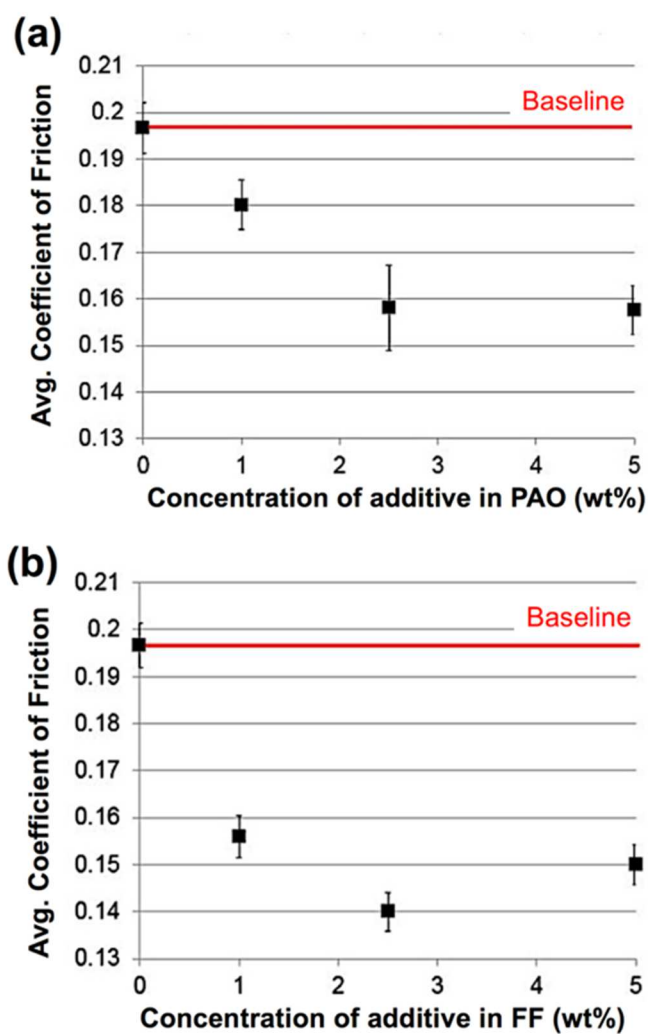


Figure 9: Ball-on-disk measurements of friction with increasing loadings of the silver precursor additive in (a) PAO and (b) FF oil. Each data point is the average of a temperature ramp experiment from 180 °C to 350 °C over 30 mins. The red line shows baseline friction for pure PAO and FF oil.

The time evolution of the ball-on-disk friction tests are shown in Figure 10. Measurement was performed while ramping temperature from 180 to 350 °C over 30 minutes. These plots show a steep increase in COF that begins around 275 °C for both fluids (PAO4 and FF oil). Initial COF measurements range between 0.15 and 0.20 for PAO4 and between 0.10 and 0.15 for FF oil, while the final measurements reach 0.30.

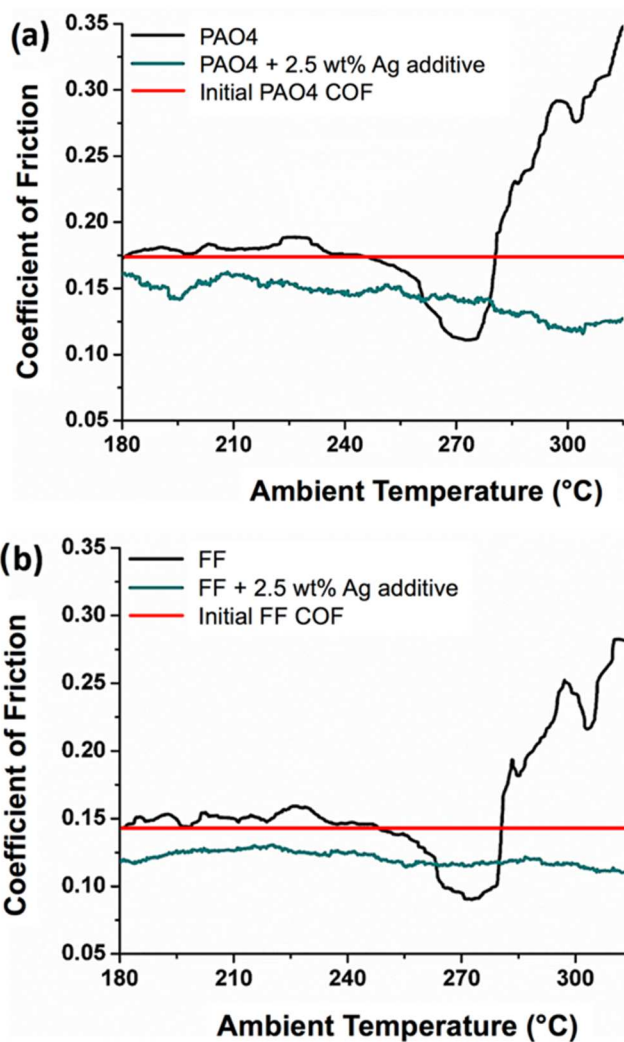


Figure 10: Ball-on-disk tribometer tests with lubricated contact for 2.5 wt % loading of the additive in (a) PAO4 and (b) FF oil. Temperature is ramped from 180 to 350 °C over 30 minutes.

The red line shows baseline friction for pure PAO and FF oil.

Note that FF oil has lower initial COFs because the additive package includes friction modifiers. Both oils exhibit a similar spike in COF at  $\sim 275$  °C, which can be explained by oil degradation at high temperature. However, when a 2.5 wt % loading of the additive is used in either oil, remarkably, the COF does not increase even though the oil begins to degrade above  $\sim 275$  °C. The transition from oil as the primary lubricant to metallic silver as primary lubricant is seamless.

The disks used in the temperature ramp tests were next analyzed by white light interferometry to determine the volume of the wear scars and the material buildup outside of the scar. Results are presented in wear coefficient, the volume of material removed was normalized by load and the distance traveled during the test. It is found that a 2.5 wt % loading of the additive reduces wear by 60 % in PAO4 and by 70 % in FF oil (Figure 11). The trend in wear is similar to the trend in COF (Figure 9), with a 2.5 wt % loading producing the lowest amounts of wear. The Gen. III additive produces comparable friction and wear results at a 20 wt % loading<sup>69</sup>. The comparable effectiveness at such low concentrations is attributable to the increased number of silver atoms per molecule, and the improved solubility in oil.

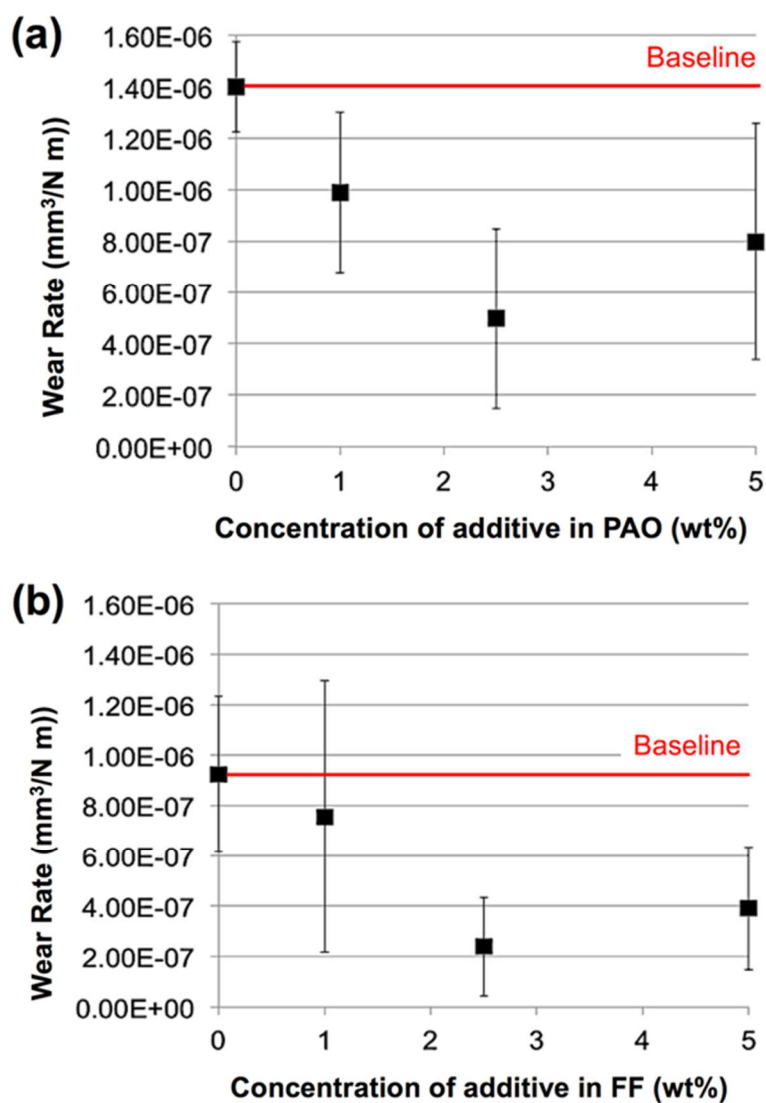


Figure 11: Wear rate measurements for the temperature-ramped ball-on-disk tribometer substrates for 1 in (a) PAO4 and (b) Fully formulated oil. White light interferometry is used to measure the volume of the wear scar at 12 positions, and the volumes for each wear scar are then averaged. The red line shows baseline friction for pure PAO and FF oil.

### 2.3.5 Surface Analysis

Scanning electron microscopy (SEM), coupled with energy-dispersive X-ray spectroscopy (EDS) was used to analyze the elemental composition of the area in and around wear scars of the steel substrates used in the friction and wear tests. Figure 12 shows EDS spectra for areas outside and inside the wear scar after ball-on-disk tests were carried out with a 2.5 wt % loading of the additive in PAO4. Note that the EDS shows a much lower concentration of silver outside the wear scar, indicating that thermolysis and subsequent silver deposition largely occur within the contact area. Neither the PAO4 nor the fully formulated motor oil (FF oil) used has additives containing silver, and it can be concluded that the silver particles deposited on the metal surface result from thermolysis of the additive.

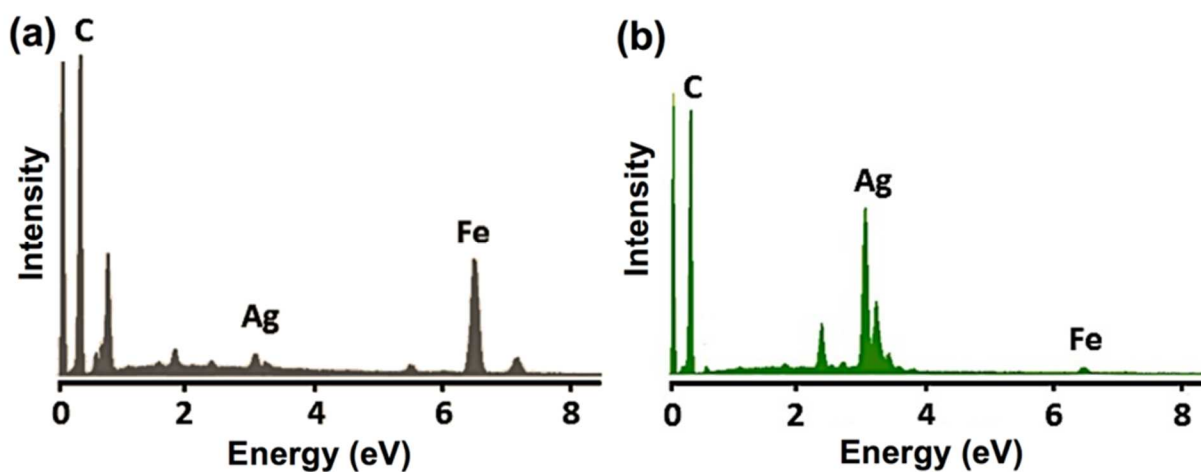


Figure 12: Energy dispersive spectroscopy (EDS) on the (a) outside of the post-test wear scar and (b) the inside of the wear scar.

SEM was used to reveal the size, morphology, and location of the silver particles formed by thermolysis of the additive. The metallic silver is primarily deposited in the form of cloudy-looking 10 - 100  $\mu\text{m}$  diameter particles within the wear scar. The box in the center of Figure 13 highlights an agglomerate of silver next to a piece of wear debris. Two-dimensional elemental mapping of silver (bottom) shows where the silver is present, and that the wear debris contains no silver.

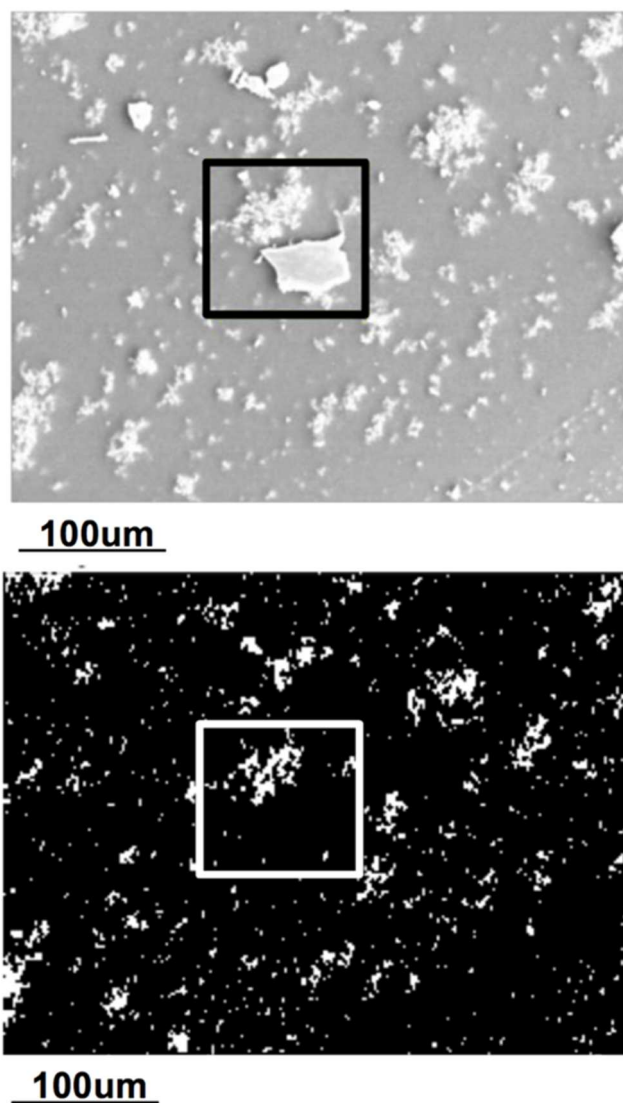


Figure 13: SEM image (top) and EDS map (bottom) of a silver agglomeration next to a piece of wear debris.

Figure 14 shows an image taken entirely within the wear scar. The surface has deep tracks resulting from asperity contacts, and silver particles spotted around the entire surface. Elemental mapping of this region (bottom) shows a higher silver concentration arranged along the line of the scars, demonstrating that the silver is primarily deposited near asperity contact.

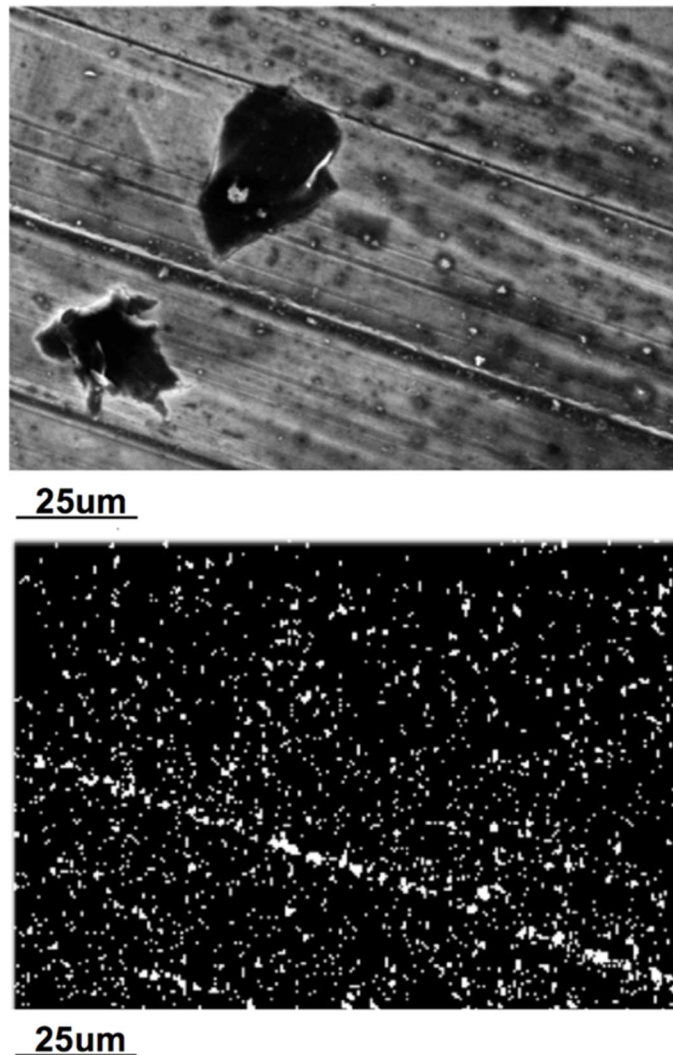


Figure 14: SEM image (top) and EDS map (bottom) of the area inside a wear scar with deep scars from asperity contact.

Figure 15 show a higher magnification image and mapping of silver particles at the edge of the wear scar. The increased silver concentration inside the wear scar on the left side is clearly present. The silver particles form an agglomerate into a cloudy appearance, and some silver particles have scattered outside the contact area.

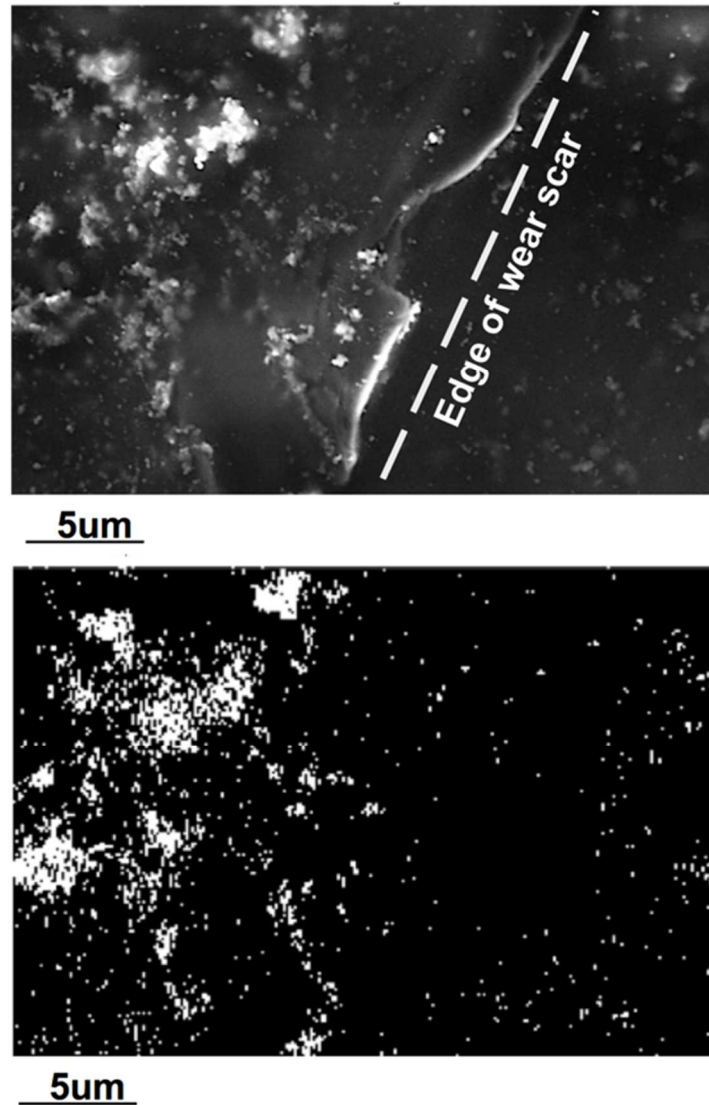
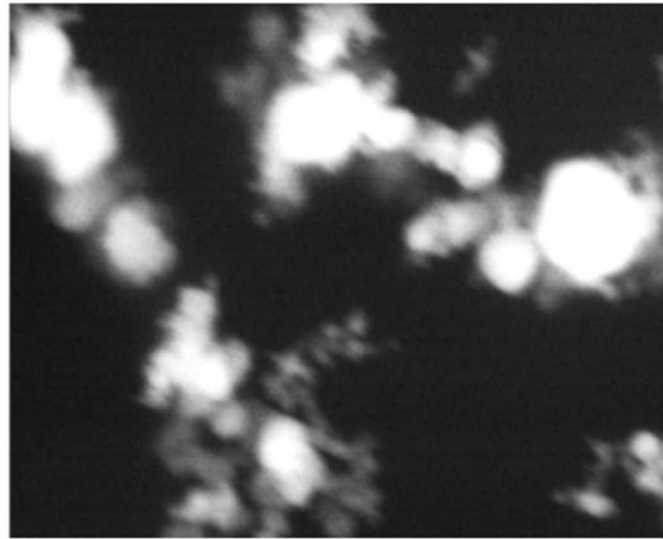
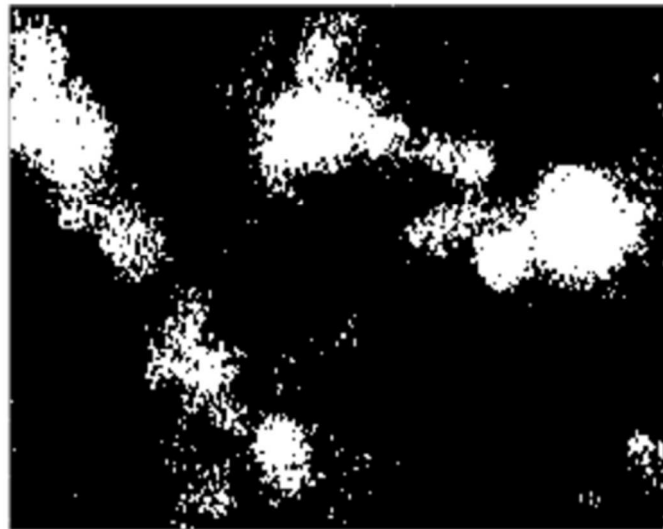


Figure 15: SEM image (top) and EDS map (bottom) at the edge of the wear scar.

Figure 16 shows SEM and elemental mapping of silver particles within the wear scar at higher magnification. From the images, it appears that the particles consist of sub-micron and nano-scale particles that have agglomeration together.



500nm



500nm

Figure 16: High magnification SEM image (top) and EDS map (bottom) of the silver particles within the wear scar.

### 2.3.6 Lubrication Mechanisms

As illustrated in Figure 17, the silver precursor additive undergoes thermolysis at elevated temperatures and pressures to deposit silver particles, which easily shear across the surface and reduce friction and wear. The mechanisms for reducing friction and wear are attributed to the specific properties of silver, particularly its softness and low shear strength. The tribochemical deposition of silver is comparable to previously reported lubricant anti-wear additives, like ZDDP, which form a tribofilm the surface and protecting against wear in the boundary lubrication regime, where interfacial surface asperities come into contact<sup>78-79</sup>. However, the silver product is inert and appears to undergo negligible chemical reaction with the surface. Instead, the it physisorbed via weak interactions. The resulting silver layer lubrication mechanism is also similar to that of silver nanoparticles, which provide anti-wear properties through formation of a boundary film with low shear stress<sup>65</sup>. Silver nanoparticles studied as anti-friction and anti-wear additives have also been shown through XPS and EDS to deposit significant amounts of silver in the pure metallic form. Nevertheless, silver nanoparticles are costly to produce, difficult to suspend in oil, and often require a surfactant to prevent particle agglomeration<sup>54</sup>.

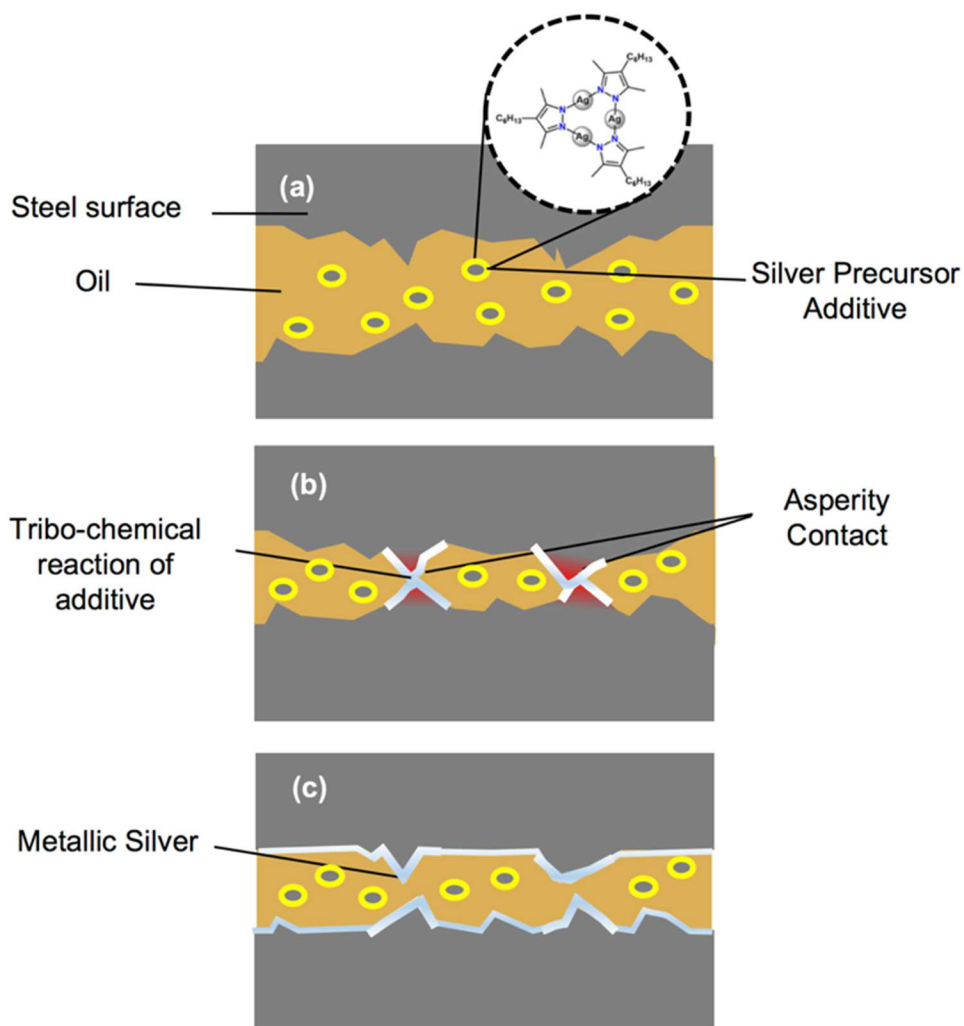


Figure 17: The tribochemical reaction and lubrication mechanism for the silver precursor additive. (a) The additive mixes with the lubricant oil and enters the tribological system. (b) The heat and pressure of asperity contact induce thermolysis of the additive, releasing metallic silver. (c) The low shear strength silver is spread across the surface, reducing friction and wear.

## 2.4 Chapter 2 Conclusions

A S-and-P free silver-organic additive molecule was developed and implemented to deposit metallic silver on tribological surfaces, thereby reducing friction and wear at temperatures where base oil degradation occurs. The following can be concluded.

- 1) The additive represents a new generation of silver lubricant additives that exhibit useful solubility in nonpolar base oil. The additive undergoes thermolysis between 313 and 332 °C. Temperature-ramped ball-on-disk experiments revealed the additive's low-friction performance at temperatures greater than ~275 °C, after both the PAO4 and FF oil failed. The transition from oil as primary lubricant to metallic silver as primary lubricant is seamless.
- 2) SEM and EDS analyses show that metallic silver is primarily deposited in wear scars, indicating that high temperature caused by asperity contacts increases the probability of thermolysis for the additive. The metallic silver acts as a protective buffer material between the contacting surfaces.
- 3) The silver additive is shown to be effective at concentrations from 1 to 5 wt %. The enhanced oil-solubility of the additive over previous generations enabled noteworthy friction and wear and friction reduction at high temperature with low loadings.

Overall, these results are a marked improvement over previous generations of silver precursor additives, as well as alternative high temperature lubrication techniques.

## Chapter 3: Organosilane Sand Dispersant

### 3.1 Introduction

Particle contamination is a of a major concern of friction and wear in lubricated systems<sup>80</sup>, and nearly all lubricants contain dispersant additives to mitigate contamination. Dispersants are typically made up of surfactant molecules with polar heads and long oil-soluble tails<sup>54</sup>. The polar end of the molecule is attracted by polar contaminant surfaces. When several surfactant molecules surround a contaminant, the combined effects of the hydrocarbon tails increase the particle's solubility in the base oil. The formation of these "molecular brushes" around contaminant particle reduces agglomeration and softens the impact between particles and surfaces. Conventionally, dispersant additives are designed for mitigation of contamination that is sourced from within a tribological system, such as soot, sludge, and wear debris<sup>80</sup>. As long as engine oils are routinely replaced to replenish these additives, soot, sludge, and wear debris contamination can be controlled using these additives. However, dispersants are not optimized for foreign contamination, which can also be a serious cause of friction and wear<sup>81-84</sup>. Sand and dust can enter tribological systems and cause contamination issues even with optimal use of oil filtration systems. The situation is more severe for machines in desert climates, which comprise 20 % of the planet's total land area<sup>85</sup>. Many parts of the world are affected by catastrophic sandstorms that can shut down transportation, drilling operations, manufacturing plants, and construction sites, leading to large economic losses<sup>82, 86</sup>. Furthermore, construction, drilling, or earthmoving projects can unsettle dust and sand that may easily enters engines and machinery. Sand and dust contamination is also a major concern in space travel, especially for missions to the moon and Mars<sup>87-88</sup>. Mineral particles like sand are covered with hydroxyl groups, which make them insoluble in oil. Without surface modification,

these particles will agglomerate in oil and lead to increased friction and wear. Current anti-contamination lubricant additives are not effective on sand or other external contaminants for numerous reasons. Dispersants are designed to be effective on particles around 1 $\mu\text{m}$  in diameter or less, while sand particle size ranges from 1 to 350 $\mu\text{m}$ . Increasing sand particle size has been shown to correlate with increasing wear damage for particles up to 100 $\mu\text{m}$ <sup>89-91</sup>. In addition to being larger than other contamination particles, sand is also a hard material. The chemical makeup of sand is mostly silica, which rates at around 7/10 on Mohr's hardness scale, making it slightly harder than the steel found in most bearings and engine components<sup>92</sup>. Therefore, sand contamination can cause embedded two-body abrasion in many tribological systems. Several studies have shown how lubricants, including fully formulated engine oil, exhibit a dramatic increase in friction and wear when contaminated with sand<sup>81, 83-84, 93</sup>.

A dispersant-like additive with reinforced surface-attraction has been developed to specifically treat sand particles. Like a dispersant, the additive coats the particle surface with long hydrocarbon chains to increase oil solubility and reduce particle agglomeration. However, instead of using polar attraction to attach the additive to contaminants, it is designed to react with the terminal hydroxyl groups covering the surface of sand particles to form a covalently bonded siloxane film on the particle surface, as illustrated in Figure 18. This hydrocarbon chains coat the surface *in situ*, or during tribological operation, with bonding energy an order of magnitude stronger than the polar interaction used in conventional dispersants<sup>94</sup>. Similar covalently bonded hydrocarbon brushes have been grafted to nanosilica substrates for use as an antifriction and antiwear additive<sup>64</sup>. Grafted

nanosilica has also been studied for drug delivery and advanced nanofiltering,<sup>95-96</sup> but this technique has not yet been studied as a surfactant treatment on contaminants.

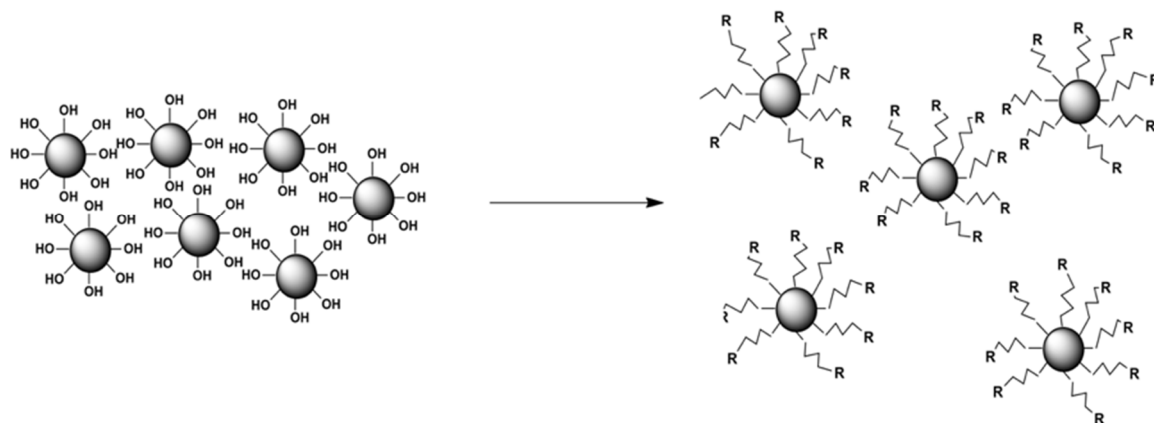


Figure 18: The reaction that converts the hydroxyl groups surrounding sand particles with long hydrocarbon chains, thus mitigating the effects of sand contamination in a tribological environment.

### 3.2 Materials and Methods

The additives developed for this technique involve alkyl functionalized silanols that bind with the terminal hydroxyl groups on the surface of sand. The additive was designed with the aid of molecular dynamics modeling, and it was characterized through a variety of chemical and tribological techniques, which are outlined in Figure 19 and described in the following sections.

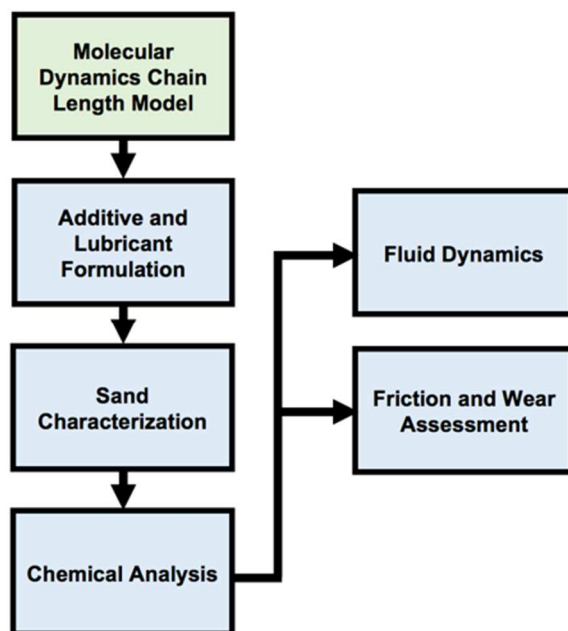


Figure 19: Diagram outlining the experimental procedure for organosilane sand surfactant. Blue boxes indicate physical experiments while green boxes indicate simulations and calculations.

### 3.2.1 Molecular Dynamics Model

The length of the functionalized hydrocarbon chain is an important variable in the design of this type of surfactant. Surfactant molecules with a reasonably long hydrocarbon chain exhibit better oil-solubility and agglomeration reduction, but when the chain is too long, additive mobility and particle affinity can be adversely affected<sup>54, 97</sup>. Because of the novelty of this type of surfactant, there was little information regarding the optimal chain length and the influence of chain length on the organosilane-silica reaction. A molecular dynamics (MD) model was developed to estimate the particle-particle repulsive interaction with increasing chain length. MD modelling is a computer simulation technique that simulates the physical movement and forces of atoms and

groups of atoms based on a prescribed model of interatomic potential energies. The goal of the MD simulations was to find the smallest chain length with sufficient particle-particle repulsion. The MD model was built on LAMMPS<sup>98</sup> and based on a model produced by Hong et al.<sup>96</sup> that studied nanosilica grafted with poly(ethylene oxide) oligomers. Hong's model is a modified version of Transferable Potential for Phase Equilibria United Atom Force Field (TraPPE-UA), which is a united-atom potential that has been validated with accurate predictions of density, vapor pressure, heat capacity, diffusivity, and many other physical properties for compounds containing oxygen, hydrogen, and carbon<sup>99-100</sup>. The model also incorporates a Buckingham force field for silicon atoms from a similar MD model<sup>101</sup>. A MATLAB script was developed to build input data files for LAMMPS that describe atom locations and bonding. The code generates two slabs of amorphous silica, and bonds alkane chains to the surface of the slabs. The slabs are separated by a prescribed distance in the z direction, and the molecules in x and y directions are periodic. This configuration, shown in Figure 20, simulates infinitely large, flat, silica surfaces that are nearly in contact.

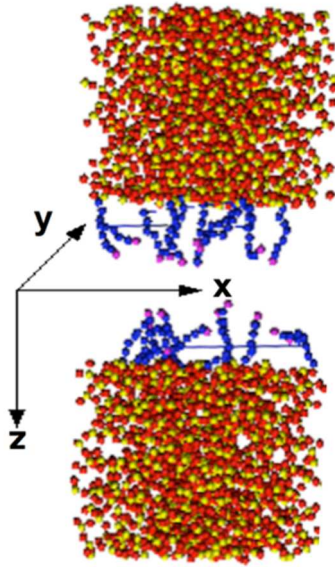


Figure 20: Configuration of the MD simulation, featuring two silica slabs grafted with hydrocarbon chains.

### 3.2.2 Sand Samples and Characterization

For physical experiments, the sand used for this study is classified following ISO12103-1, the standard for testing sand contamination in oil filters, engines, and other tribological applications.

The sand particle cumulative size distributions are shown in

Figure 21a, and the “medium” and “coarse” grades chosen for these tests have a mean particle size of 18 and 35  $\mu\text{m}$ . The chemical makeup of the sand, provided by the supplier and shown in

Figure 21b, consists of mostly silica, as well as other minerals and a small amount of metal oxides.

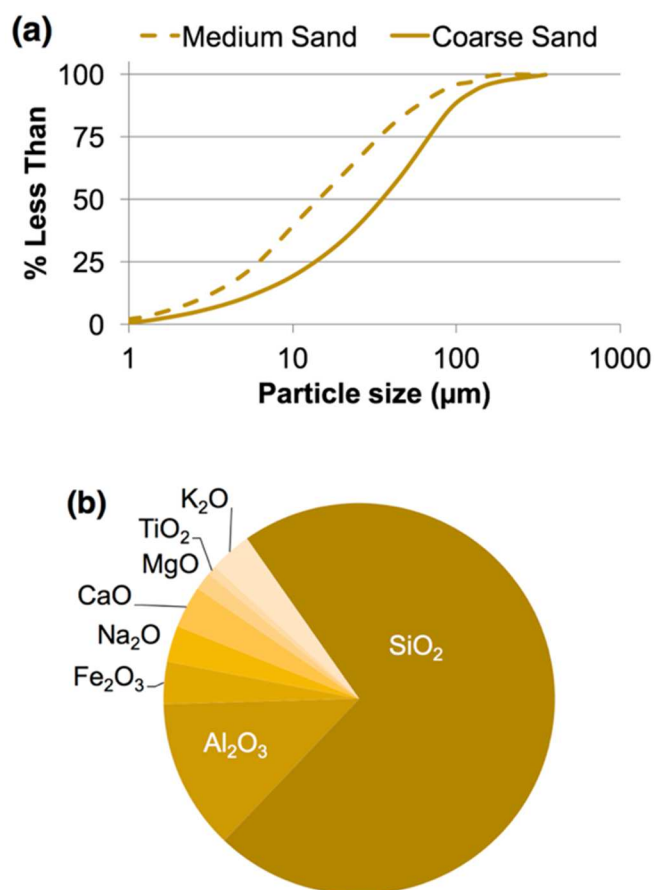


Figure 21: The cumulative size distribution of medium and coarse grade sand (a), and (b) the chemical constituents of sand.

### 3.2.3 Lubricant Formulation

Two different surfactant additives were formulated for testing: one with a 10 carbon alkyl chain, and another with an 18 carbon chain, as shown in Figure 22, based on insight from the MD model. Several formulations of lubricant samples, shown in Table 3, were created by mixing sand, additive molecules, and a catalyst into PAO4. For better control over formulation amounts, the reaction between sand and the additive was performed before tribometer testing in a simulated tribological environment.

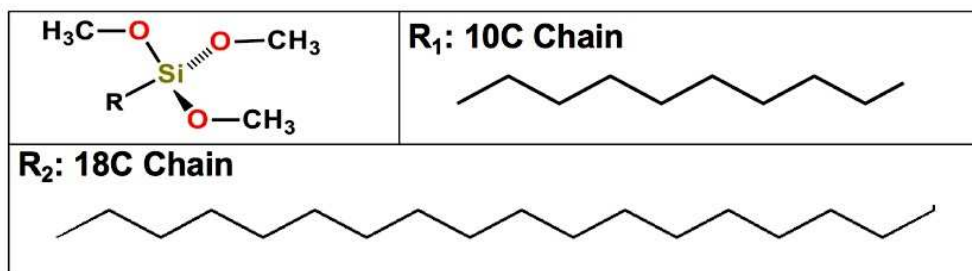


Figure 22: Organosilane additives for sand particle contamination control with 10 and 18 carbon chain lengths.

A round bottom flask was charged with sand particles (2g) and toluene (50mL), which mimics the non-polar environment of base oil and has a high boiling point. Under high speed magnetic stirring, first, 5 % of the catalyst, dimethylhydroxy(oleate)tin (DMHOT), was added followed by the desired amount of organosilane additive, n-decyl(trimethoxy)silane with a 10 carbon chain and an 18 carbon chain (C10 and C18). Dimethylhydroxy(oleate)tin is a condensation-cure catalyst commonly used to make silicone and urethane polymers<sup>102</sup>. Organoalkoxysilane precursors have been previously used in organosiloxane/siloxane co-condensation reactions<sup>103-104</sup>. The formulations were stirred for 12 hours at 90°C, the average temperature of an automotive engine<sup>23</sup>. Formulation was performed with assistance Prof. Tobin Marks's Northwestern Chemistry Lab.

Table 3. Formulations of lubricant samples for sand contamination tests.

Sample	Base Oil	Sand	Additive	Catalyst
1	PAO	-	-	-
2	PAO	1% Medium Grade	-	-
3	PAO	1% Medium Grade	1wt% C10	5% DMHOT
4	PAO	1% Medium Grade	1wt% C18	5% DMHOT
5	PAO	1% Coarse Grade	-	-
6	PAO	1% Coarse Grade	1wt% C10	5% DMHOT
7	PAO	1% Coarse Grade	1wt% C18	5% DMHOT

The reaction between the organosilane additive and the oxide surface of sand (silica), demonstrated in Figure 23, can be described in three steps. First, the additive's methoxy groups ( $\text{O}-\text{CH}_3$ ) surrounding the silicon atom are hydrolyzed in the presence of moisture, and the additive molecule is attracted to the oxide surface due to hydrogen bonding. The additive's silanol protons are more electrophilic than alcohol protons, which results in a high dipole moment for its silanol group. Therefore, the silanol group is oriented towards the oxide surface and hydrogen bonds are formed. Then, a condensation reaction then occurs, forming covalent bonds between the silica and the linked additive molecules. This generates a siloxane film on the silica surface, which can be functionalized with any desired R group. The siloxane film thickness depends on the water concentration of near the silica surface.

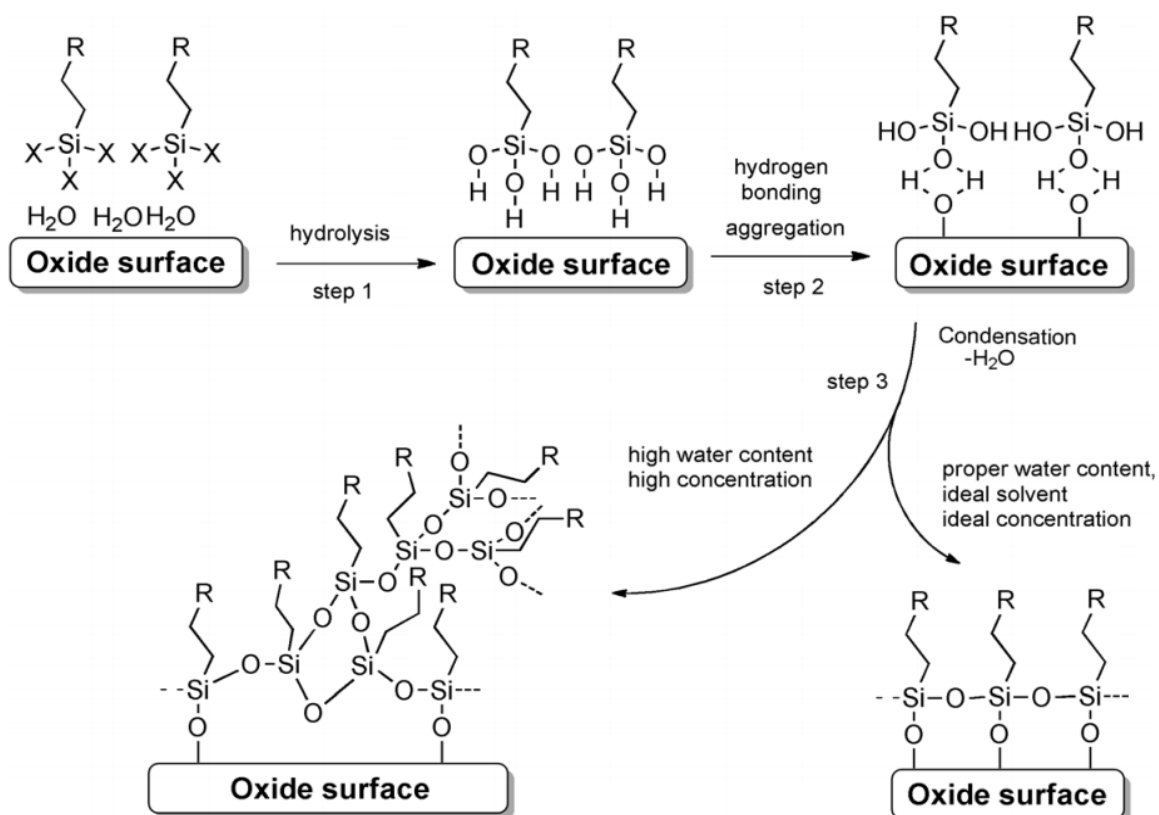


Figure 23: The reaction between the additive and the oxide surface of silica that forms a siloxane film on sand particle surfaces.

In order to confirm this reaction pathway, Fourier transform infrared spectroscopy (FTIR) and thermogravimetric analysis (TGA) were performed on a silica sample mixed with the additive and catalyst, and a reference sample that was left without the treatment.

### 3.2.4 Tribological Studies

Tribometer experiments were carried out in a CETR UMT-2 Tribometer, as described in the previous chapter. Again, the disk was made of 52100 steel, and the ball was made of M50 tool steel slightly harder than the disk, both with a roughness of 30 nm. For all tests, the Hertzian pressure was 1 GPa, and the tests ran at 1 m/s relative motion for 30 minutes. The BL regime was chosen to ensure tribological surfaces would be prone to abrasive wear and asperity contact. To prevent the sand from settling in the fluid before testing, the formulations were mixed and sonicated for 10 minutes and then immediately tested. Each tribometer test was repeated at least twice. The friction force was recorded, and wear measurements were taken on the wear scar of the worn disk after cleaning via WLI.

Table 4: Tribometer Test Conditions for the organosilane additive.

<b>Test Parameter</b>	<b>Value</b>
Applied load (N)	15
Hertzian Contact Pressure (GPa)	1.0
Disk rotation speed (rpm)	100
Radial location of contact (mm)	20
Sliding contact speed (m/s)	1
Total sliding distance (m)	754
Base oil	PAO4
Test duration (min)	30

### **3.2.5 Fluid Dynamics Tests**

The viscosity of the fluid from each formulation was measured using an Ostwald viscometer in a constant-temperature bath at room temperature and at the ambient vehicle engine temperature of 90°C. Dynamic Light Scattering (DLS) was performed on a Malvern Zetasizer to measure the size and stability of particles in the oil formulations. DLS measures the diffraction of a laser beam traveling through a fluid to estimate the range of particle sizes in the fluid. Fluid samples were thoroughly mixed and sonicated before measurement, and size distributions were calculated from 10 laser scans. Particle size was measured three times at a 60 second interval.

## **3.3 Results and Discussion**

### **3.3.1 MD Analysis for Chain Length**

Ideally, the hydrocarbon chain should be as short as possible while still providing sufficient particle-particle repulsion. Before experimentation, MD simulations were performed to provide insight into the ideal length of the additive's hydrocarbon chain. Each simulation involved two silica slabs with grafted alkane chains of varying length being together while measuring the repulsive force acting on one slab by the other. When the force vs. distance curve is integrated over displacement, the resultant energy value corresponds to the work required to bring two particles together. Figure 24(a) shows the force vs. distance curves for all simulations. Increasing the chain length corresponds to higher repulsive force for all cases, but the correlation is not linear, and the effect of increasing repulsive force diminishes with longer carbon chains. Figure 24(b) shows the integrated force-distance energy values for various chain lengths. Based on the MD results, the 18-carbon (C18) hydrocarbon chain length was chosen as the most reasonable option,

because chains longer than 18 carbon atoms long did not show a significant improvement in particle-particle repulsion. For comparison, a 10-carbon chain additive (C10) was also formulated and tested.

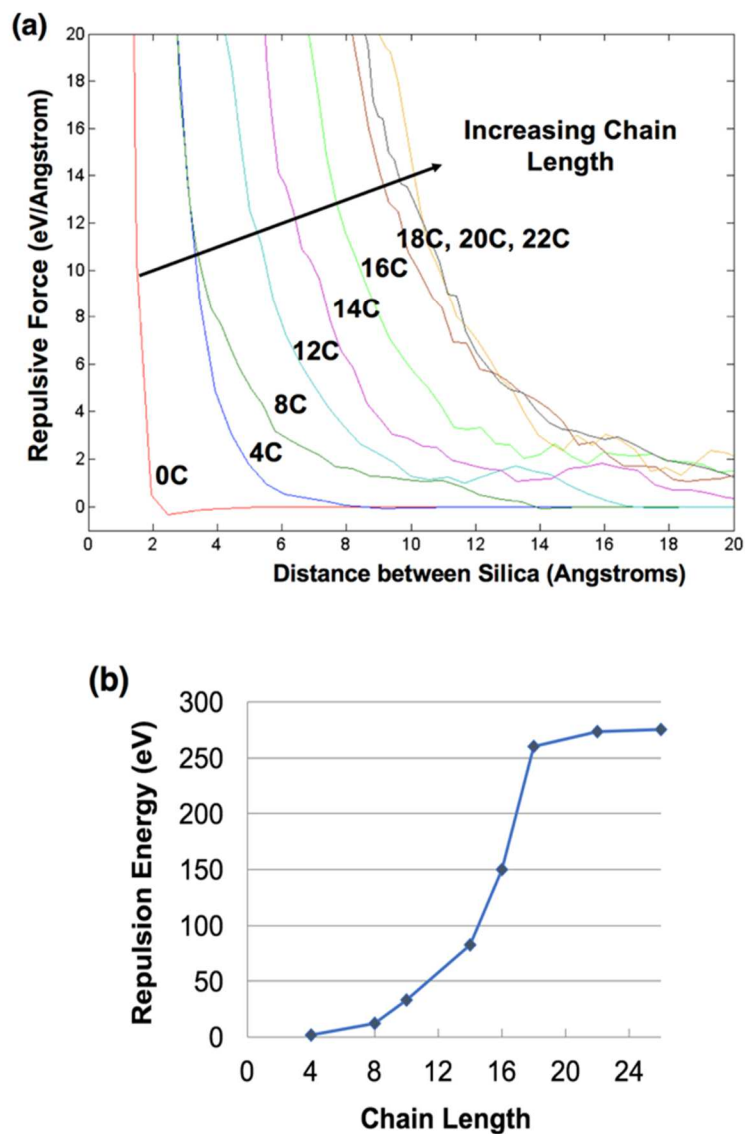


Figure 24: The MD model calculating repulsive force vs. distance curves (a) and total repulsive energies (b) for various hydrocarbon chain lengths of the organosilane molecule grafted to silica.

### 3.3.2 Reaction Analysis

Figure 25 shows the difference in appearance of the different lubricant samples. Adding sand particles to the clear base oil makes the fluid semi-opaque, but the effect is greatly reduced for PAO with sand particles treated with the additive.

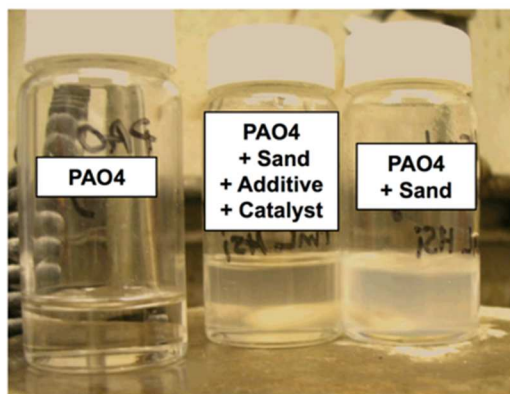


Figure 25: Visual difference between PAO4, PAO4 with sand particles, and PAO4 with sand particles and the additive package.

FTIR spectroscopy results are shown in Figure 26(a). At around  $1100\text{ cm}^{-1}$ , Si-O-Si peaks<sup>105</sup> are observed for both samples, confirming the presence silica. The silica sample mixed with the additive loses its hydroxyl peak<sup>106</sup> at around  $3500\text{ cm}^{-1}$ , and a faint alkyl peak<sup>107</sup> appears at around  $2700\text{ cm}^{-1}$ . The reaction was only proven between pure silica particles and the additive, because the FTIR signal for the additive–test sand mixture did not show any indication of a reaction in a non-tribological lab environment. The TGA results, shown in Figure 26(b), reveal a weight loss of 6 % in the reacted sample. This is due to thermolysis of the organosilane molecules at high temperature. The unreacted sample, consisting only of thermally stable silica, lost almost no weight.

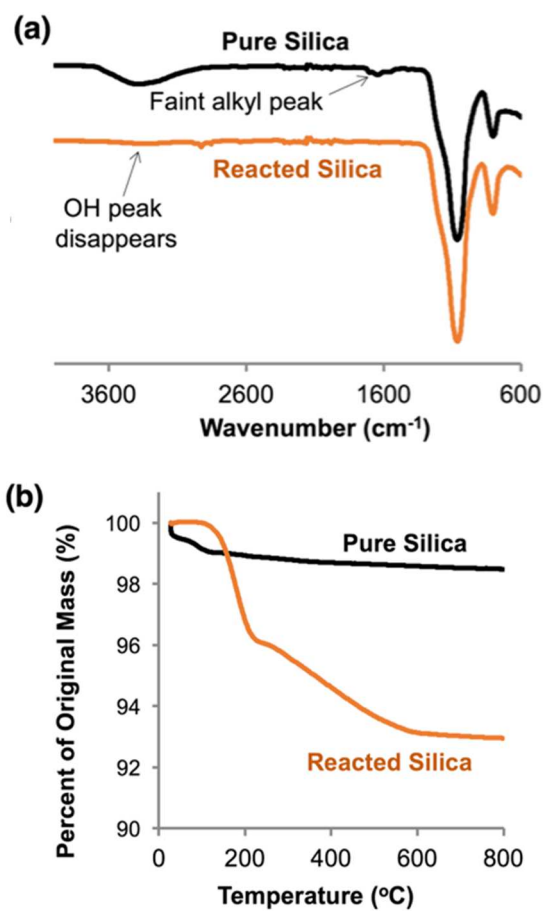


Figure 26: FTIR (a) and TGA (b) results for pure silica and silica mixed with the additive and catalyst. The peaks for Alkyl and OH features change after the reaction occurs, suggesting a successful reaction, and only the reacted silica experiences weight loss during heating.

### 3.3.3 Friction and wear results

The entire series of oil-sand-additive mixtures underwent tribological testing, and the friction and wear performance of each sample were evaluated. The wear results, shown in Figure 27, demonstrate a significant increase in wear with the addition of sand. Wear volume was increased by 73 and 82 % due the medium and coarse sand contamination, respectively. The coarse sand caused a higher wear rate, which is in agreement with the particle size effect reported in other studies<sup>89-91</sup>. Both additives types were successful in reducing the effect of contamination wear. Each additive sample was able to reduce wear back to wear level when lubricated with the pure PAO4, with the exception of the C10 sample with medium sand, which reveals the importance of sufficient alkane chain length of the additive.

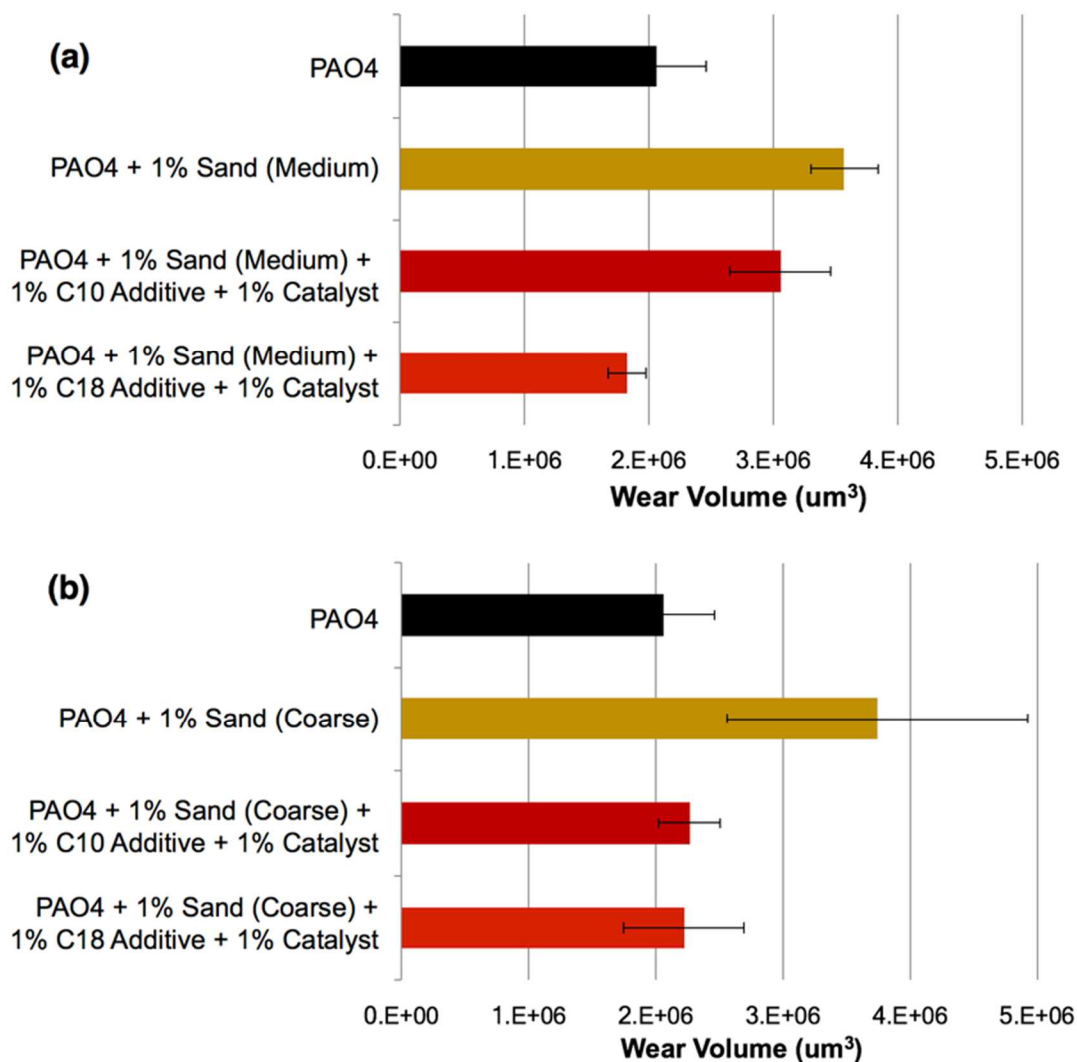


Figure 27: Wear results for disks lubricated with the pure PAO4 and contaminated PAO4 with and without the additives, using medium (a) and coarse (b) grade sand.

Figure 28 shows the time-averaged friction results for all tribometer tests. Sand contamination caused an equal increase in friction of about 15 % for the oils containing the medium or coarse grades of sand. Particle size is known to influence wear results, but not necessarily friction. The friction force is attributed to increased asperity contact by roughened surfaces, as well as sand

particles embedded in mating surfaces, which causes increased friction due to plowing<sup>108</sup>. Both the C10 and C18 additives were able to prevent these effects, and the C18 additive was able to lower friction comparable to that obtained using the pure PAO4.

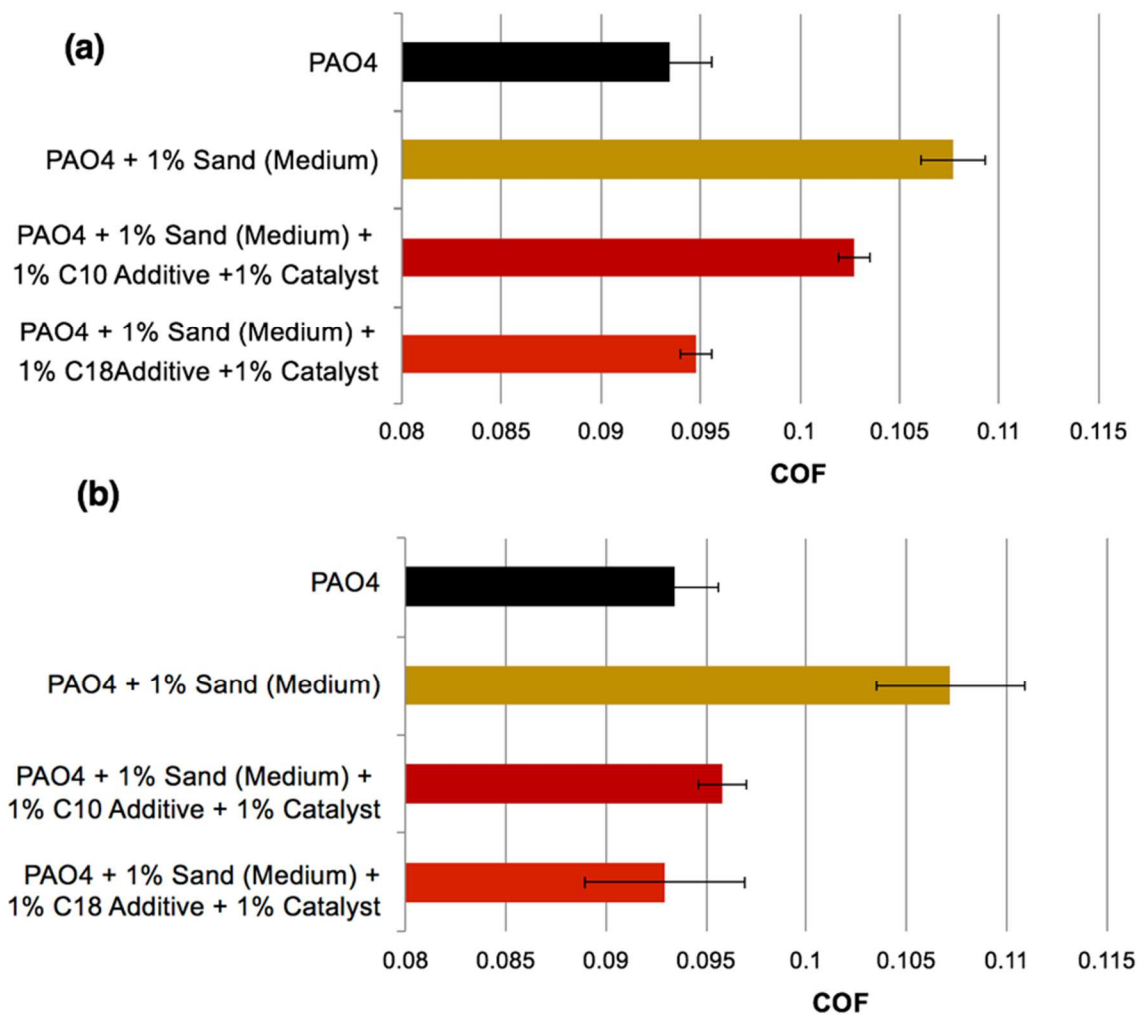


Figure 28: Average friction results for pure PAO4 and contaminated PAO4 with and without the additives, using medium grade sand (a) and coarse grade sand (b).

### 3.3.4 Fluid Dynamics

Figure 29 shows three DLS measurements of the formulations taken at one minute intervals. The Zetasizer is designed for small particles and does not successfully detect particles larger than  $10\mu\text{m}$ . Therefore, only the medium grade sand was tested with DLS. If particles larger than  $10\mu\text{m}$  are excluded from the cumulative size distribution of

Figure 21(a), the resulting average size of the detectable particles is around  $5\mu\text{m}$ , which corresponds well with the DLS measurements. The time-evolution of DLS measurements can be used qualitatively to observe the oil-solubility of sand. The first measurement was performed immediately after the sample was mixed and sonicated for accurate readings. As time proceeds, insoluble particles agglomerate and settle at the bottom of chamber<sup>80</sup>. Because the DLS sensor is unable to detect particle sediment, only smaller particle sizes were recorded, and the average particle size was underreported. The additive-free sample exhibits this underreporting behavior over time, suggesting insoluble sand particles in the fluid and agglomeration at the bottom of the chamber. Meanwhile, the C18 additive sample maintains a more constant DLS reading, which indicates improved solubility and the prevention of sand agglomeration.

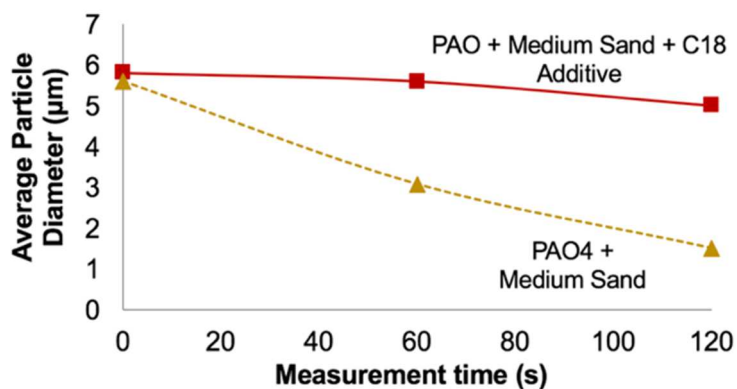


Figure 29: DLS measurements of the average particle size of 1 wt % of medium grade sand in PAOs with and without the C18 additive. Measurements were taken in one minute intervals.

Viscosity analysis, shown in Figure 30, was performed only for the more effective C18 additive, and excluded the C10 version. At room temperature, the coarse grade sand caused a 16 % increase in viscosity, while medium grade sand increased viscosity by 3 %. The 90°C viscometry tests show a much less significant change in viscosity. This is expected, as viscosity change from contamination is less severe at higher temperatures<sup>109</sup>. The additive appears to slightly reduce viscosity from sand contamination by improving the oil-solubility of sand particles. However, the grafted sand particles may also act as an oil thickener, which would counter the effect. The chemical morphology of a long chain alkane-grafted particle mimics that of high molecular-weight polymer viscosity modifying additives that are used to increase viscosity<sup>110</sup>.

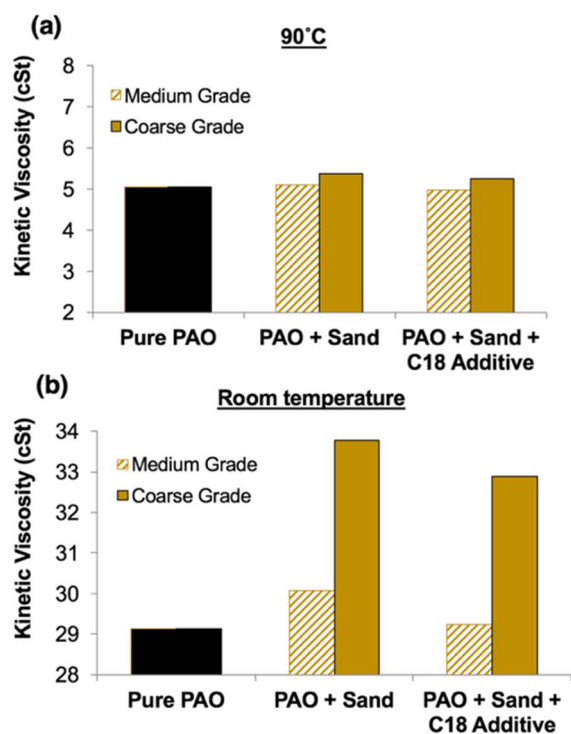


Figure 30: Viscosity of pure PAO and contaminated PAO, with and without the C18 additive, at room temperature (a) and 90°C (b).

### 3.4 Chapter 3 Conclusions

A new organosilane surfactant was developed to reduce the friction and wear from sand contamination, and the following conclusions were observed.

- 1) The additive is molecularly engineered to form *in situ* covalent bonds with the oxide surfaces as they enter a tribological system. The siloxane films on the particle surfaces are functionalized with hydrocarbon chains that increase the solubility of sand in oil and reduce agglomeration of sand particles. The reaction between silica and the additive was confirmed using FTIR and TGA.

- 2) Friction and wear increased due to contamination by about 15 and 75 %, respectively., and the friction and wear increases were mitigated through the addition of the silica surfactant additive.
- 3) The effect of the additive and sand on viscosity were analyzed, and the additive mitigated the viscosity increase due to medium sand at room temperature. DLS measurements revealed the ability of the additive to increase solubility of the sand in the oil.

Overall, the sand surfactant additive represents a promising alternative solution to sand contamination in lubricants.

## Chapter 4: Novel Carbon Tribofilm Additive

### 4.1 Introduction

Extreme-pressure (EP) additives, the additives designed specifically to protect surfaces in BL and ML conditions, work by harnessing the energetic and chemically active environment at asperity contacts to form lubricious and protective tribofilms. Despite its effectiveness, use of the EP additive ZDDP has been increasingly discouraged because phosphorus- and sulfur-containing residues from the decomposition of ZDDP can accumulate in catalytic converters<sup>50, 111</sup>, causing permanent damage<sup>112-115</sup>. Dozens of sulfur- and phosphorus-free EP functional alternatives to ZDDP have been developed over the years, but none have been cost-effective enough to replace it<sup>116</sup>, and a low-cost alternative has long been needed.

Carbon, specifically graphite, has been used for lubrication for centuries, but recent discoveries and developments have shed new light on carbon as a material of the future<sup>117</sup>. Some applications of carbon lubrication have been presented as a potential replacement for phosphorus- and sulfur-containing lubricant additives like ZDDP<sup>118-119</sup>. The lubricity of a carbon material depends on its environment and the hybridization of its carbon-carbon bonds. As shown in Figure 31,  $sp^3$ -bonded carbon has a three dimensional, rigid structure crystal structure that produces hard, inert, and non-conductive materials, while  $sp^2$ -bonded carbon exists in polycyclic two-dimensional crystal structures with weak inter-plane bonding between its lamellar structure.

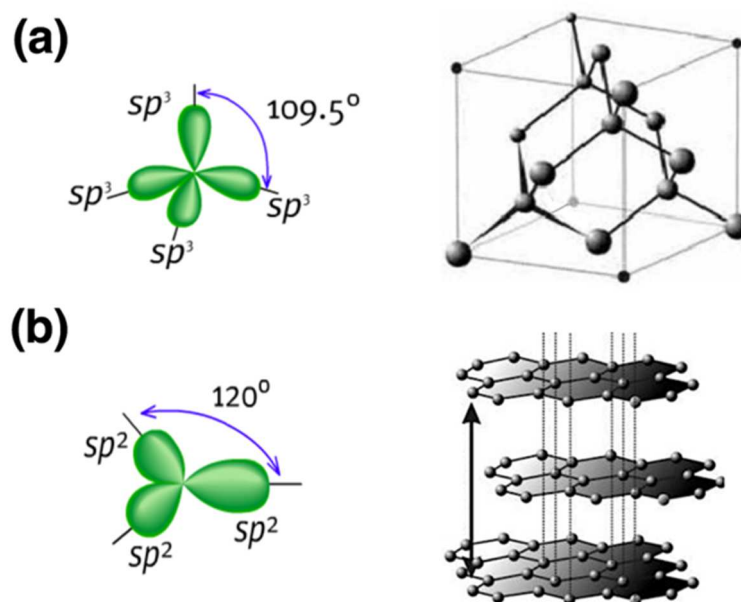


Figure 31: The bonds directions and crystalline structure of (a)  $sp^3$ - and (b)  $sp^2$ -bonded carbon<sup>120</sup>.

The traditional carbon lubricant, graphite, consists primarily of  $sp^2$ -bonded carbon. Graphite lubrication was used heavily in the Industrial Revolution, and was also one of the first vehicle lubricant additives<sup>121</sup>. Although its use as an additive has been phased out due to discoloration and agglomeration issues, graphite is still used as a solid lubricant<sup>122-125</sup>. The lubricity of graphite is derived from its lamellar polycyclic carbon structure, which has in-plane strength 100 times greater than its lateral shear strength. During contact, graphite basal planes orient parallel to the direction of contact lower friction by shearing across each other. The low shear strength of graphite is dependent on adsorption of water vapor between the planes, which passivates the outer carbon atoms and keeps the lamellae separated<sup>126</sup>. However, under extreme localized temperature and pressure, the intercalated vapor can desorb from the graphite layers, causing exposure of reactive

carbon edge sites that dramatically increase inter-plane attraction and cause a spike in friction<sup>127-</sup>  
<sup>128</sup>. This is also why graphitic lubricity is highly dependent moisture in the ambient air<sup>129</sup>.

A variety of novel carbon nanomaterials have also been adopted to tribological applications for friction and wear improvement. Carbon nanotubes are used in coatings and as lubricant additives to reinforce the strength of surfaces and serve as rolling spacers that prevent direct contact between asperities<sup>130</sup>. Single layer graphite sheets, known as graphene, can be chemically modified to have enhanced oil solubility, thereby increasing its effectiveness as a lubricant additive over graphite suspensions<sup>131</sup>. Although these nanomaterials have shown promising results, their wide-scale adoption has been restricted by cost, solubility issues, and complicated formulation procedures<sup>132</sup>.

Diamond-like-carbon (DLC) is another recently discovered carbon-based material used in tribology. DLC is a catch-all term for amorphous carbon materials containing a mixture of hydrogen,  $sp^2$ - and  $sp^3$ -bonded carbon, and other elements such as nitrogen and metals. It has been used industry-wide in protective overcoats for computer disk drive contact surfaces since the early 1990's<sup>133-137</sup>. More recently, DLC, has been applied as low-wear surface coating on bearings and cutting tools<sup>136</sup>. DLC has been shown to exhibit excellent tribological performance with ultra-low friction behavior. This behavior is attributed to lubricious graphitic films that slide between surfaces, much like graphite and graphene<sup>138-139</sup>. For automotive applications, a major problem for DLC is that it must be deposited on surfaces as a pre-treatment during manufacturing. Delamination, poor adhesion, and high internal stresses are among some of the challenges for DLC coatings in tribological applications<sup>140</sup>. Once the coating is worn away, it cannot be replenished

without complete disassembly of the system. Furthermore, DLC-coated surfaces are chemically inert, and therefore have poor compatibility with conventional lubricant additives<sup>19, 141-142</sup>.

One may circumvent the problems with DLC discussed in the preceding paragraph by producing carbon tribofilms *in situ*, rather than relying solely on a static DLC coating. Carbon tribofilms are known to form when hydrocarbons dissociate at asperity contacts<sup>143-144</sup>. Although properties of carbon tribofilms vary widely, they are generally formed through a distinct chemical pathway<sup>143</sup>. First, hydrocarbon adsorbed near the contact undergoes tribochemical oxidation, resulting in high-molecular-weight polymers that precipitate out of the fluid. The hydrocarbon macromolecules then dehydrogenate into amorphous carbon, and continued frictional energy input causes further transformation to graphitic carbon films. Graphitic carbon reduces friction and wear by providing a soft, low-shear-stress buffer material between mating surfaces<sup>15, 143, 145</sup>. Under certain conditions, including under vacuum conditions, and extreme temperature and loading conditions, carbon tribofilms can be as effective as ZDDP tribofilms<sup>144, 146-147</sup>. Erdemir and coworkers developed a catalytically active coating based on nanoscale copper that facilitates the dissociation of the lubricant's hydrocarbon base fluid into such lubricious carbon tribofilms<sup>146</sup>. Additional studies have documented carbon-based tribofilms with carbon derived from base fluids and carbon-containing vapors<sup>50, 148-153</sup>. These studies represent a promising alternative technique to conventional EP additives, but they are limited by various factors. The surfaces presented in these studies are often modified to create catalytically active environment necessary for lubricious carbon tribofilm formation. If such surface modification is worn away, or depleted at the locations

where such a film is demanded, the process to form lubricious carbon films cannot be reactivated without component disassembly and coating re-deposition.

The work reported in this paper represents a novel technology for EP lubricant additives designed to provide replenishable carbon films *in situ* at the location of contact, without any pre-treatment of the contact surfaces, under practical operating conditions. The additive is designed to undergo a tribochemical reaction that produces a lubricious carbon film. An example molecule embodying this concept has been demonstrated through tribotesting and surface analysis. Analysis of the tribochemistry and lubrication mechanisms will then be presented. Tribofilm success is dependent on a variety of factors, including load, shear stress, temperature, catalysis, and more. These factors can be difficult to disentangle, and extensive testing is required to understand the mechanism of tribofilm growth, and reveal key factors that are important to the additive's performance. The technique is also applied to applications for further illustration. The overall experimental design is outlined in Figure 32 and described in the following section.

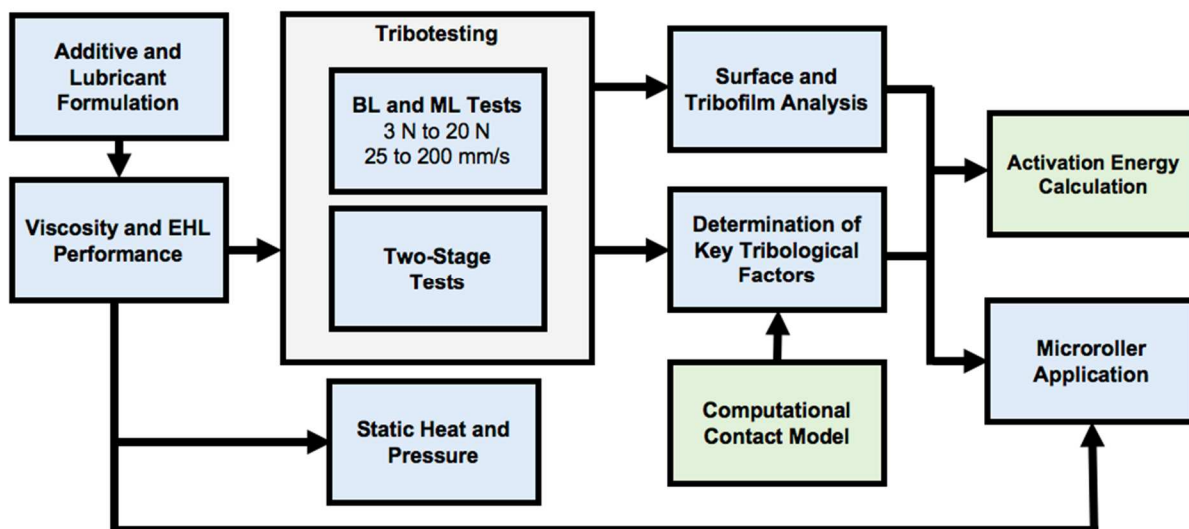


Figure 32: Diagram outlining the experimental procedure for carbon the tribofilm additive. Blue boxes indicate physical experiments while green boxes indicate simulations and calculations.

## 4.2 Materials and Methods

### 4.2.1 Additive and Lubricant Formulation

By principle, the carbon tribofilm precursor molecule must be soluble in base oil and have two key moieties. The first is a three- or four-carbon cycloalkane, which is metastable because the carbon-carbon bonds within the cycloalkane are highly strained and are therefore prone to dissociation, compared to linear hydrocarbons in base oil<sup>153</sup>. The second moiety is a surface-active group that binds the molecule to the surface via dipole forces, directly coupling the frictional energy to the precursor molecule<sup>143</sup>. Carboxylic (-COOH) and alcohol (-OH) groups are examples of such surface-active species. Cyclopropanecarboxylic acid (CPCa), shown in Figure 33(a), is an obvious choice of molecule for this concept for many reasons. The molecule is widely produced and commercially available at a low-cost<sup>154</sup>, and cyclopropane is the cycloalkane with the highest

amount of ring strain<sup>155</sup>. The bonding angle between three bonded carbon atoms is  $60^\circ$ , while the ideal tetrahedral angle is  $109.5^\circ$ , as shown in Figure 33(b). The irreversible ring-opening of cyclopropane is easily catalyzed by transition metals, and it has a low oxidation potential<sup>156</sup>. These factors make cyclopropane much more prone to release carbon in a tribological environment than its linear alkane counterpart, propane<sup>157</sup>. Figure 33(c) shows how the additive arranges itself on the contact surface and how frictional heat and pressure would be directly transferred from the surface to the metastable cyclopropane ring. The additive was added in 2.5 wt % concentration to PAO4 base oil, with no other additives included, in order to avoid misattribution of any effects from the CPCa.

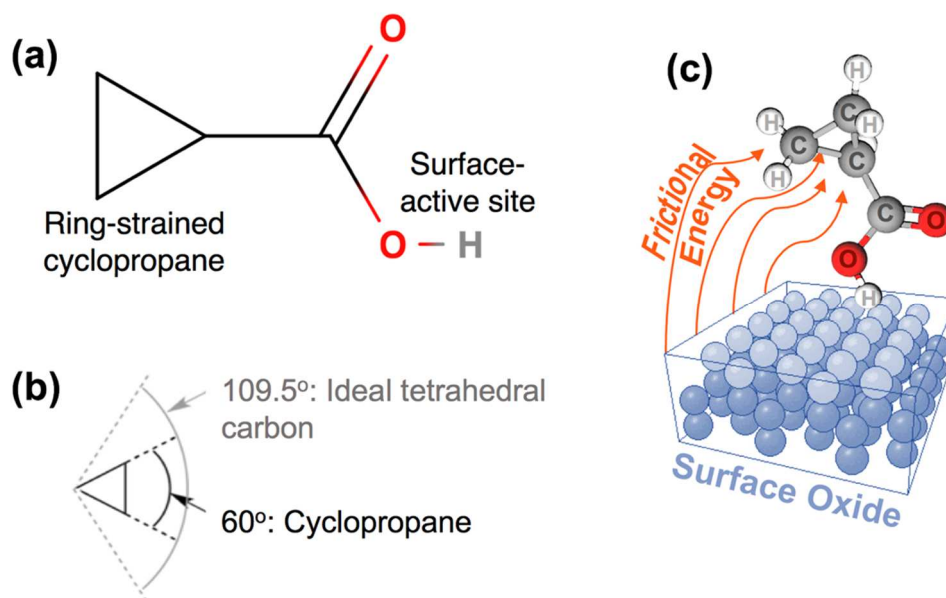


Figure 33: CPCa molecule containing a metastable carbon ring (cyclopropane) as the carbon source and a surface-active group ( $-\text{COOH}$ ) that provides adsorption to the surface.

#### 4.2.2 Fluid dynamics and solubility

Before testing BL and ML functionality, it must first be shown that the additive does not interfere with the lubricant's fluid properties and performance during EHL conditions. CPCa is fully miscible with PAO4. No phase separation was observed, even after leaving the fluid still for 48 hours, as shown in Figure 34.

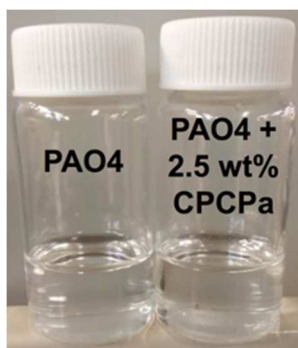


Figure 34: Picture of PAO4 and PAO4 + 2.5 wt % CPCa after sitting for 48 hours. No phase separation was observed.

Figure 35 shows that the addition of 2.5 % of CPCa has no influence on the shear stress–strain rate behavior, and only causes a slight increase in viscosity at low strain rates. Carboxylic acids are routinely used as additives in lubricant formulations, and this compatibility should be expected.

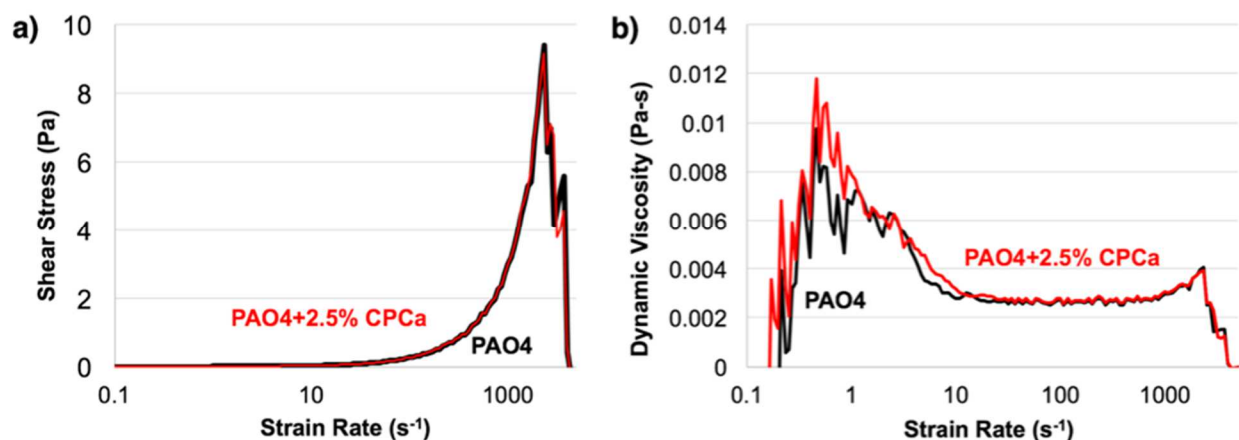


Figure 35: Shear stress (a) and dynamic viscosity (b) of PAO4 influenced by strain rate with and without the addition of 2.5 wt % CPCa.

#### 4.2.3 Tribological Studies

ML and BL ball-on-disk tests were performed under fully flooded lubrication in simple sliding for 30 minutes using a CETR UMT-2 tribometer, following similar methods from the previous chapters. For this series of tests, the ball and disk were both 52100 bearing steel with a hardness of 60 HRC, polished to root-mean-square roughness ( $R_z$ ) of 50 nm and 100 nm, respectively. Table 5 shows the test matrix consisting of 20 test conditions at different speed-load combinations, designed to reproduce a range of BL and ML conditions. An additional set of tests, referred to as the two-stage test, was designed to see the lasting effect of the carbon tribofilms on a surface after CPCa has been removed from the lubricant. For all tests, the friction force was measured in real time during tribotesting, while wear of the ball was evaluated after testing using WLI. The wear rate is defined as the volume removed from the surface divided by the distance traveled.

Table 5: Tribometer Test Conditions for the carbon tribofilm additive

<b>Test Parameter</b>	<b>Value</b>
Applied load (N)	3, 5, 10, 15, 20
Hertzian Contact Pressure (GPa)	0.5-1.4
Sliding contact speed (mm/s)	25, 50, 100, 200
Total sliding distance (m)	45-360
Base oil	PAO4
Additive concentration (wt %)	2.5
Temperature range (°C)	RT
Test duration (min)	30

#### 4.2.4 Computational Contact Model

Tests conditions were selected to cover the BL and ML regimes, based on film thickness predictions made using the same contact modeling software from Chapter 2<sup>77</sup>. The software model also predicts the maximum asperity flash temperature and the percentage of the total load supported by asperities, as opposed to fluid support.

#### 4.2.5 Determination of Key Tribological Factors

A large range of tribological test conditions were studied in order to isolate the most important factors influence friction and wear reduction for the carbon tribofilm. By combining the predicted information provided by the computational contact model with experimental results, the overall trends involving the relationship between friction, wear, fluid film thickness, asperity contact, temperature, and other properties can be determined.

#### 4.2.6 Surface and Tribofilm Analysis

Post-test surfaces were cleaned and then analyzed using optical microscopy, scanning electron microscopy (SEM), Raman spectroscopy, and nanoindentation. Nanoindentation was performed using a Berkovich tip. The roughness of the surfaces was also observed using WLI and the topography software SPIP. In the Raman spectrum, two features, the D and G bands, around 1360 and 1560  $\text{cm}^{-1}$  respectively, have been extensively discussed in the literature. The G band corresponds to carbon  $\text{sp}^2$  bond stretching within the crystalline graphite structure. The D band is linked to vibration at the edges of graphite or graphene structures, and is associated with disordered, non-crystalline carbon morphology<sup>158</sup>. The relationship between these properties and a sample's carbon peaks are shown in Figure 36. The Raman spectrum for unreacted CPCa does not exhibit peaks D or G peaks<sup>159</sup>.

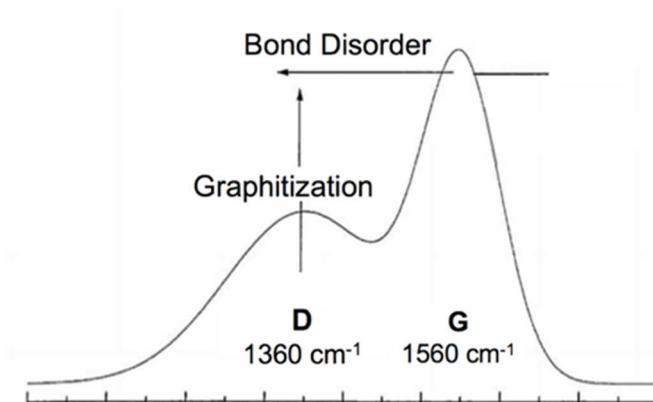


Figure 36: Characteristic peaks for Raman spectroscopy of carbon species, and how shifts in the peak can indicate properties of the peaks.

#### 4.2.7 Static Heat and Pressure Tests

In order to demonstrate that the formation of a carbon tribofilm from the additive is indeed tribologically induced, it must be shown that the same temperature and pressure under static loading will not produce a carbon tribofilm. The same ball-on-disk tribological test setup was used to apply a static 20 N load, with and without 100 °C ambient heating, for 30 minutes, with no relative motion between the ball and disk. The post-test surfaces were examined with Raman spectroscopy to search for evidence of carbon formation. To further understand the behavior of the thermal dynamics of the additive and base oil during simple heating, TGA with mass spectroscopy (TGA-MS) was performed on the PAO4 + 2.5 CPCa sample, revealing the precise reactants that might occur during static heating of the sample.

#### 4.2.8 Microroller Application

In addition to tribological testing, this research was applied to an experimental manufacturing project developed at Northwestern University's Advanced Manufacturing Processing Lab: the electrically assisted microrolling (EA $\mu$ R) mill<sup>160</sup>. The EA $\mu$ R rolls microscale patterns into small samples of sheet metal, while passing a high current through the workpiece, as shown as Figure 37. The current heats up the workpiece, softening it for enhanced forming. The roll on the device also features specialized surface textures, which transfer to the workpiece and generate multifunctional features, such as hydrophobicity and drag reduction. The EA $\mu$ R device provides a high-load, low-speed contact, heated contact surface that is suitable for our lubricant additive. The EA $\mu$ R project benefited from the implementation of lubrication to improve its forming process, and also the implementation of carbon coatings on the sample substrate during the micro-rolling process. Four sheet metal samples were rolled through the machine, creating a microscale channel pattern. One sample was dry, another had pure PAO4, another had just the CPCa additive, and the last was a mixture of POA4 with the additive. Raman was performed in the same spot on each workpiece after testing.

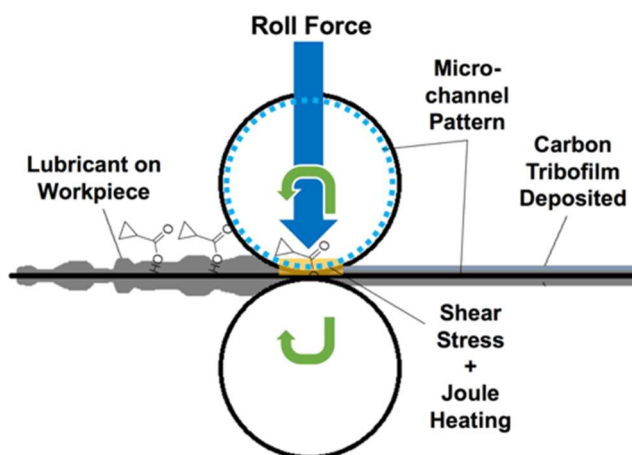


Figure 37: Illustration of the EA $\mu$ R functioning with the carbon precursor additive.

#### 4.2.9 Activation Energy

The energy required for activation of a tribofilm precursor additive is an important piece of information for lubrication engineers, but the kinetics of tribochemical reactions are complicated by the fact that the pressure of contact greatly influences the energy landscape of chemical reactions. Through analysis of this additive's friction performance and time evolution, a novel method for obtaining the activation energy of tribofilm formation was developed, using a data set compiled from a range of speed and load conditions. The method is used to calculate the activation energy of CPCa tribofilm formation, though the process could possibly be adopted for any friction-reducing tribofilm. The energy of tribofilm CPCa tribofilm formation is predicted for a range of loading conditions, and compared with literature values for non-tribochemical reactions.

## 4.3 Results and Discussion

### 4.3.1 Friction and Wear Performance

Figure 38 presents wear rates obtained from 20 tests using PAO4 as lubricant and 20 tests using PAO4+CPCa. When averaged over all 20 tests, PAO4+CPCa results in a 93 % reduction in wear rate compared with neat PAO4.

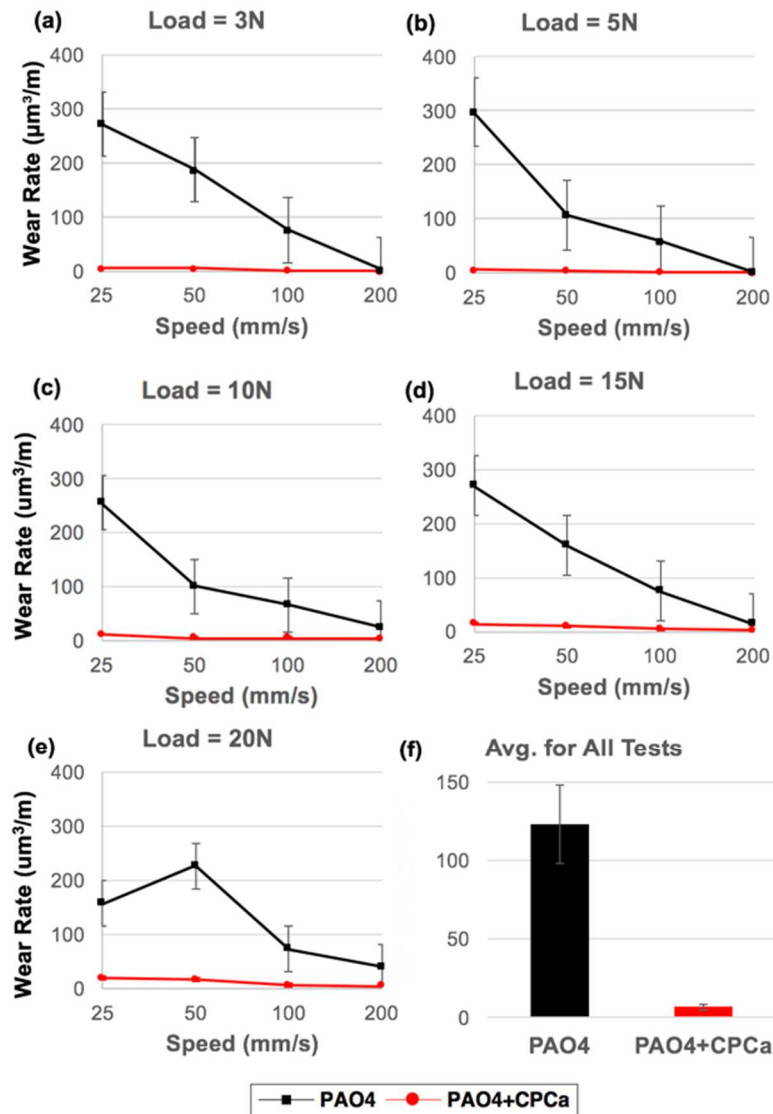


Figure 38: Wear rates for tests using PAO4 and PAO4+CPCa as lubricants, and a comparison of wear rates averaged over all 20 tests using these two lubricants.

Figure 39 shows results on coefficient of friction, averaged over 30 minutes, obtained from 20 tests using PAO4 as lubricant and 20 tests using PAO4+CPCa. When averaged over all 20 tests, PAO4+CPCa yields an 18 % reduction in coefficient of friction compared with neat PAO4. The more successful trials reach COF values matching those observed in DLC studies ( $\sim 0.06$ )<sup>161-162</sup>.

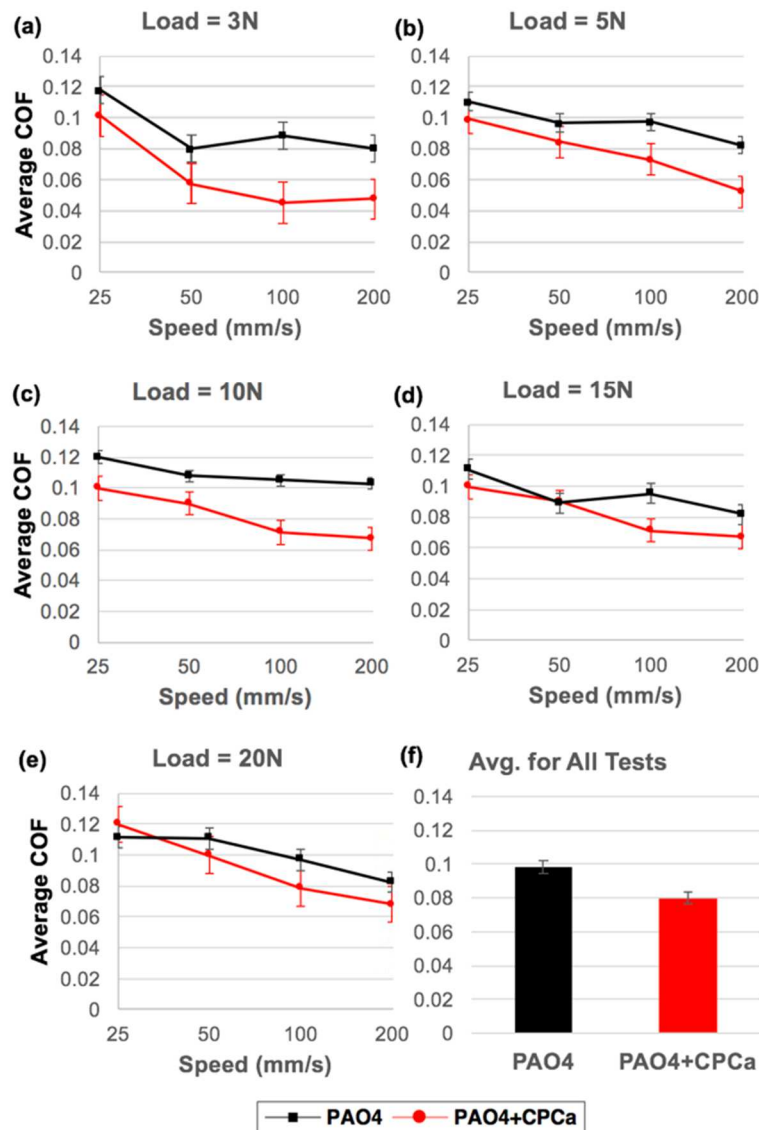


Figure 39: Time-averaged coefficient of friction for tests using PAO4 and PAO4+CPCa as lubricants, and a comparison of friction coefficients averaged over all 20 tests using these lubricants.

Figure 40 shows the time evolution of friction coefficient for a few representative tests. The friction curves for the PAO4+CPCa fluid have two notable features. First, they exhibit an exponential decay of friction from the neat PAO4 value to a lower steady-state value, within the first few minutes of the test. The shape of the curve is similar to what has been observed previously for other tribofilm-forming additives<sup>52, 163-165</sup>. The second feature, shown in Figure 40(c-d), is a sudden jump after in the coefficient of friction a few minutes of tribotesting. These friction spikes were also observed contacts lubricated by a graphene suspension in ethanol, suggesting the cause if related to graphitic carbon lubrication<sup>36, 51</sup>. All friction vs. time plots for PAO4+CPCa follow either the shape of Figure 40(a-b) or (c-d).

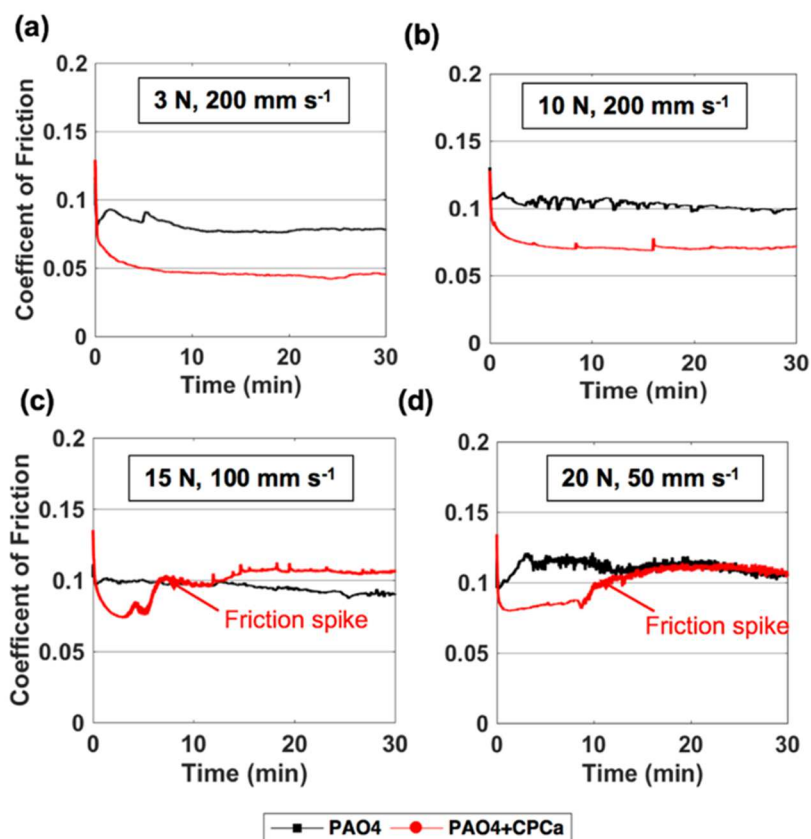


Figure 40: Friction-time curves, showing initial rapid friction reduction (a-b), in the presence of CPCa, and in some cases, followed by sudden friction increase, as noted in (c) and (d).

With significant friction and wear reduction demonstrated, the next tests aimed to examine if the carbon deposited by the CPCa remains effective even after the additive is no longer present in the lubricant. A 2-stage tribometer test was performed: In stage 1, boundary lubrication tests were performed on disk A, with PAO4 and disk B, with PAO4 + 2.5 wt % CPCa. Then, without removing the disks from the tribometer, the fluids were cleaned from the system, and in stage 2, the tests were repeated using pure PAO4 on both disks. Figure 41 shows that friction was reduced in Disk B, for both stage 1 and stage 2, showing that a coating of carbon generated in stage 1 provided lasting improvement in friction, even after the CPCa additive was removed. Figure 41 also shows wear reduction in disk B, as expected.

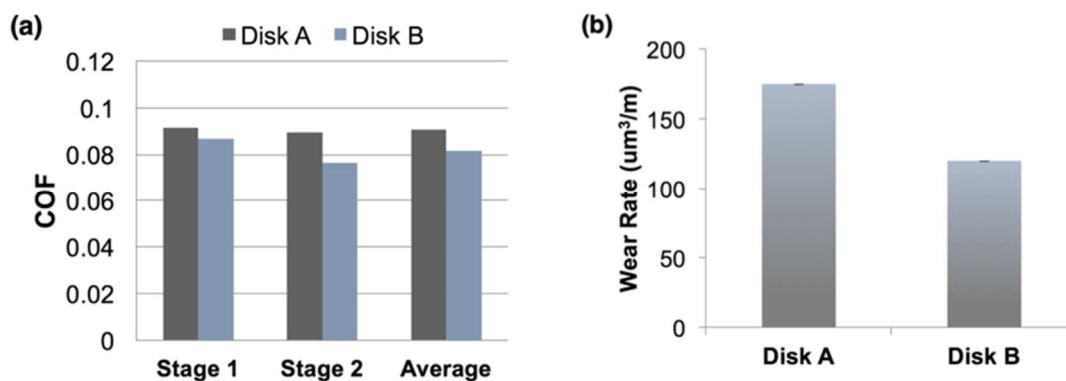


Figure 41: Friction and wear results from the 2-stage test. Disk A was lubricated with PAO4 for both stages, Disk B was lubricated with PAO4 + 2.5 wt % CPCa for stage 1, and pure PAO4 for stage 2.

### 4.3.2 Tribological Performance Factors

Figure 43 shows a series of interpolated heat maps plotting the trends of wear rate and average friction from the 20 experiments using PAO4 + CPCa. Black circles indicate points where the tests were actually performed, and the maps were filled in between those points through linear interpolation. The best performance in friction and wear occurs at low loads and high speeds. According to the Stribeck curve, these conditions are associated with greater load support from the fluid<sup>166</sup>. In graphite lubrication, smooth friction and low wear depend on a continuous oriented graphitic transfer layers, and these layers can be penetrated by wear debris and asperity contact<sup>167</sup>.

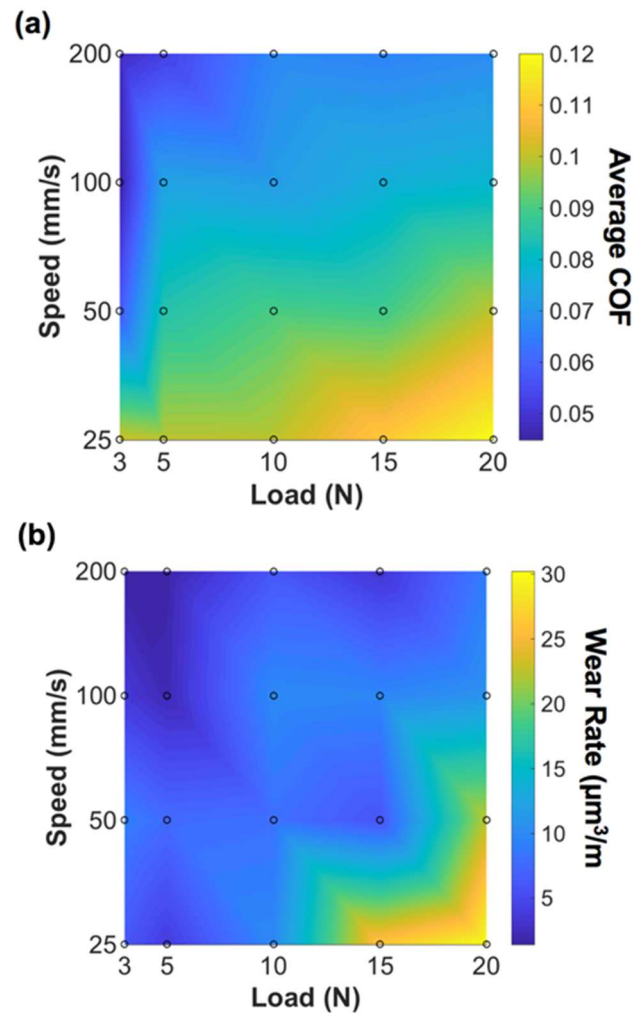


Figure 42: Interpolated maps of (a) friction and (b) wear results based on tests using PAO4+CPCa.

The friction and wear results show an especially strong correlation with the contact load ratio, which is the computationally predicted percentage of load supported by the solid, instead of through hydrodynamic support, as shown in Figure 42. Figure 42(a) is a heat map of contact load ratio for each of the tests, and superimposed onto this plot are indicators of which PAO4+CPCa tests resulted a friction spike, as seen in Figure 40(a-b). Figure 42(b) shows how the wear rate correlates with this percentage (contact load ratio).

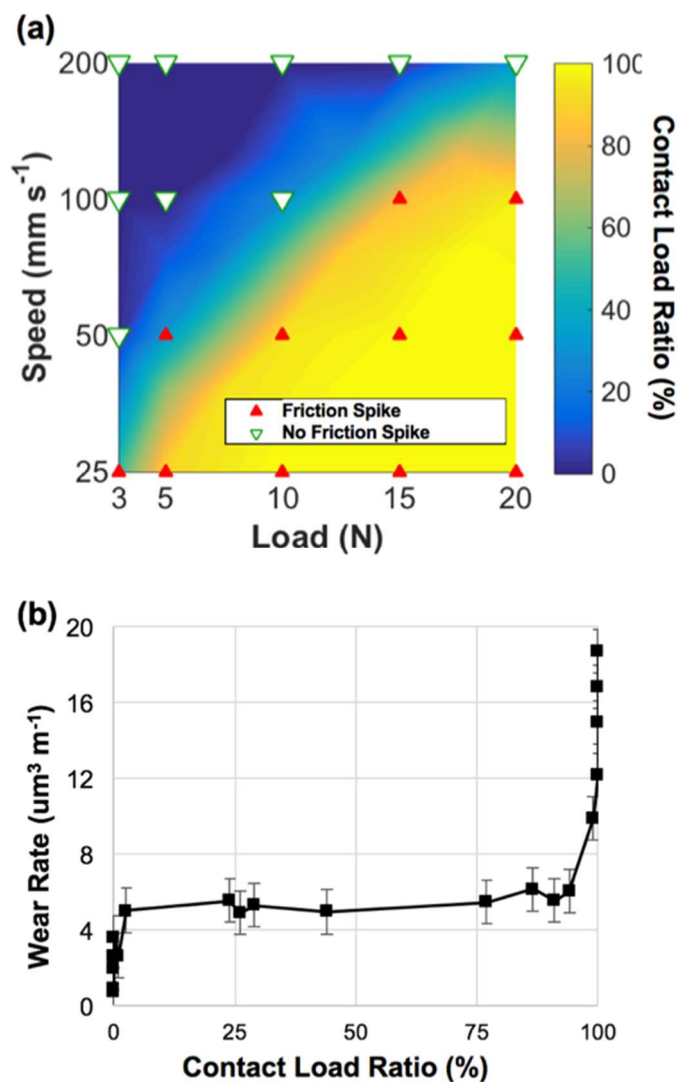


Figure 43: (a) Occurrence of tribofilm failure using PAO4+CPCa at certain speed-load combinations, with an overlay of the contact load ratio. (b) Wear rate vs. contact load ratio. Note the constant wear rate for  $L_c$  between 5 and 95 %.

There is a transition point of contact load ratio equal to about  $30 \pm 10$  %, at which point the friction spikes no longer occur. Also, the wear rate remains constant while the contact load ratio is between 5 and 95 %, and then sharply increases when the two surfaces come into complete contact and

there is no load support by the fluid. Some fluid load support is evidently necessary for the tribofilms to provide consistent friction and wear reduction. Carbon lubrication generate a large volume of transfer layers that move inside and outside of the contact area, and a low fluid film thickness could lead to agglomeration of carbon and wear debris near the contact area, which in turn inhibits fluid flow even further<sup>168</sup>. Partial fluid support also helps prevent localized loading on graphitic carbon from asperity contact, which can cause desorption of vapor between the graphite layers, and rapid friction increases in friction<sup>128, 169</sup>.

### 4.3.3 Tribofilm and Surface Properties

Figure 44 is an optical micrograph of the wear scar with carbon deposits on the disk surface after testing with PAO4+CPCa at 10 N load and 200 mm s<sup>-1</sup>. Carbon deposits from graphitic DLC transfer films have been reported as discontinuous particle clusters similar in appearance to the image<sup>170-172</sup>.

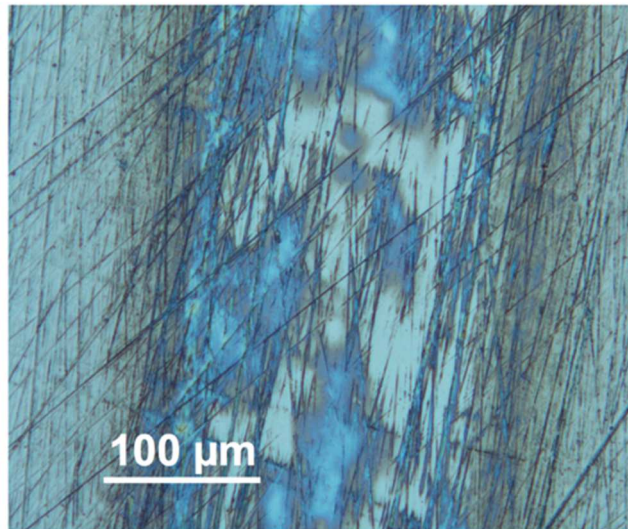


Figure 44: Optical micrograph obtained from the disk surface after tribotesting at 10 N and 200 mm s<sup>-1</sup> with PAO4+CPCa.

Figure 45 is a series of Raman spectra taken from the untested disk surface, the wear scar, a commercial DLC film, and the colored deposit seen in Figure 44. This comparison identifies the deposit as DLC-like carbon tribofilm, which is present only in samples tested with PAO4+CPCa. Its adhesion to the disk surface is not strong, and it is removed after five-minute sonication in hexane.

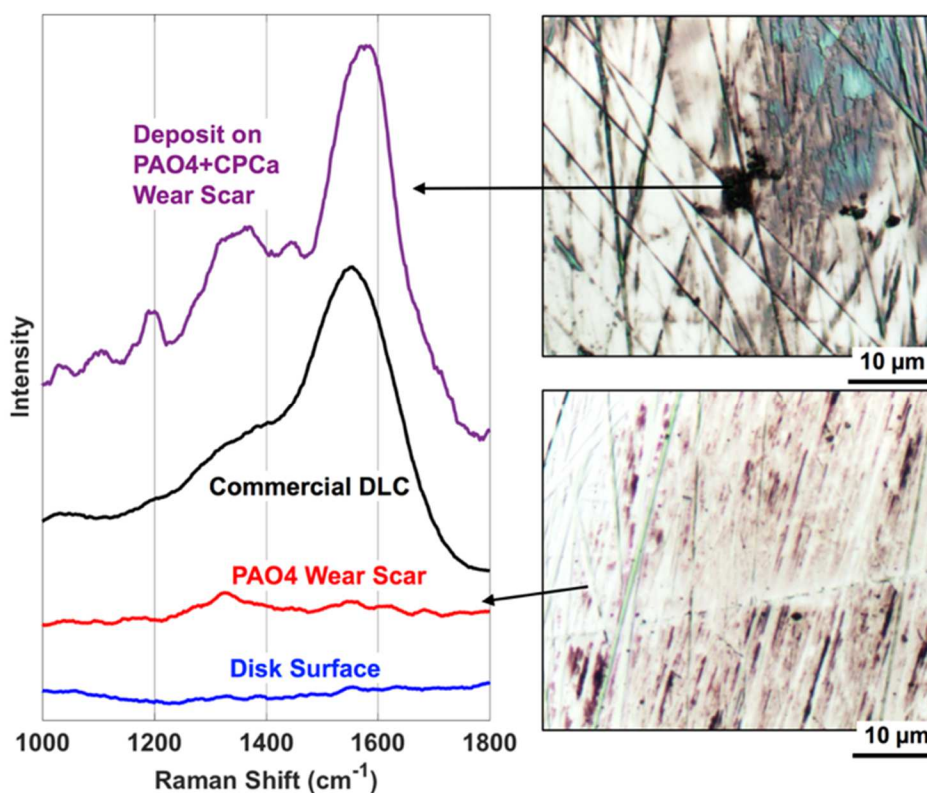


Figure 45: Raman spectra obtained from the untested disk surface, the wear scar, a commercial DLC film, and the colored deposit in the wear track.

The root-mean-square roughness of different regions on the surface were recorded using WLI and are presented in Figure 46. The carbon deposits, seen in the colored streaks Figure 44, are very smooth, and the entire PAO4+CPCa wear scar also had a lower roughness than the PAO4 sample's wear scar. The increased smoothness of carbon tribofilms has also been observed in graphite lubrication<sup>173</sup>. After sonicating in hexane, carbon was no longer visible on the surface, and the roughness increases to its original value.

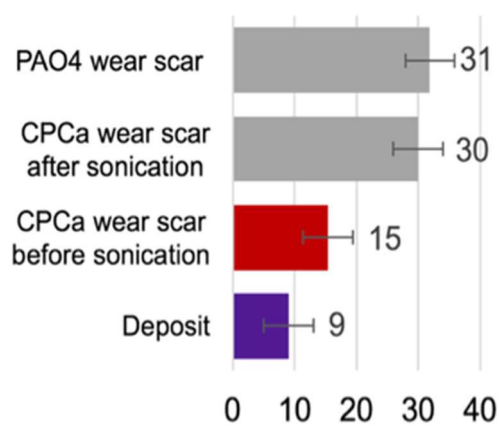


Figure 46: Surface roughness of various regions on the post-test surface.

Figure 47 compares the nanoindentation curve obtained from the PAO4 wear scar surface and the colored deposit (carbon tribofilm). The larger indentation depth on the carbon film at the same load shows that it is softer than the PAO4 only wear scar, which suggest a graphitic carbon layer on the surface after testing<sup>174</sup>.

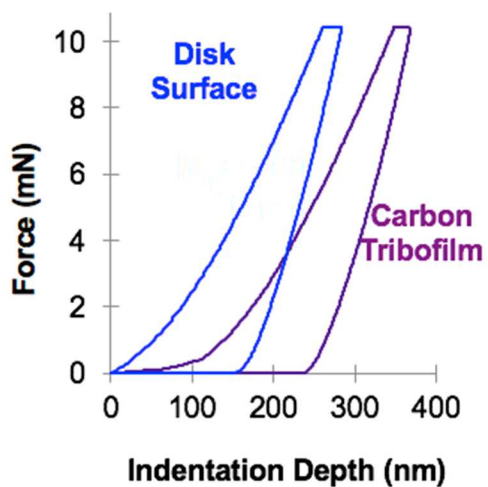


Figure 47: Nanoindentation curves obtained from the disk surface and the carbon tribofilm.

Figure 48-Figure 54 are a series of SEM images obtained from the disk surface after testing at 200 mm s<sup>-1</sup> and 10N. Figure 49 shows two wear tracks, one after testing in PAO4 and one in PAO4+CPCa. The streaks of dark material on the bottom wear scar were previously identified as a DLC-like material using Raman spectroscopy.

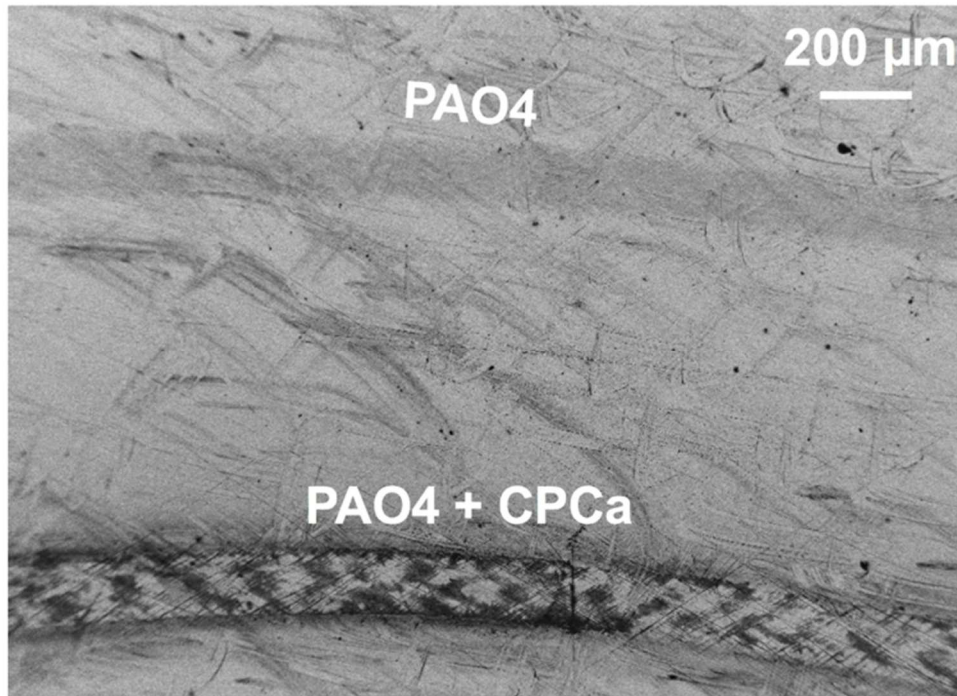


Figure 48: SEM image of the post-test disk, lubricated with PAO4 and PAO4+CPCa.

Figure 49 gives a more detailed look at the flaky appearance of the carbon material generated within the wear scar. The material is similar in appearance to DLC transfer layers and other carbon tribofilms previously reported<sup>50, 161</sup>.

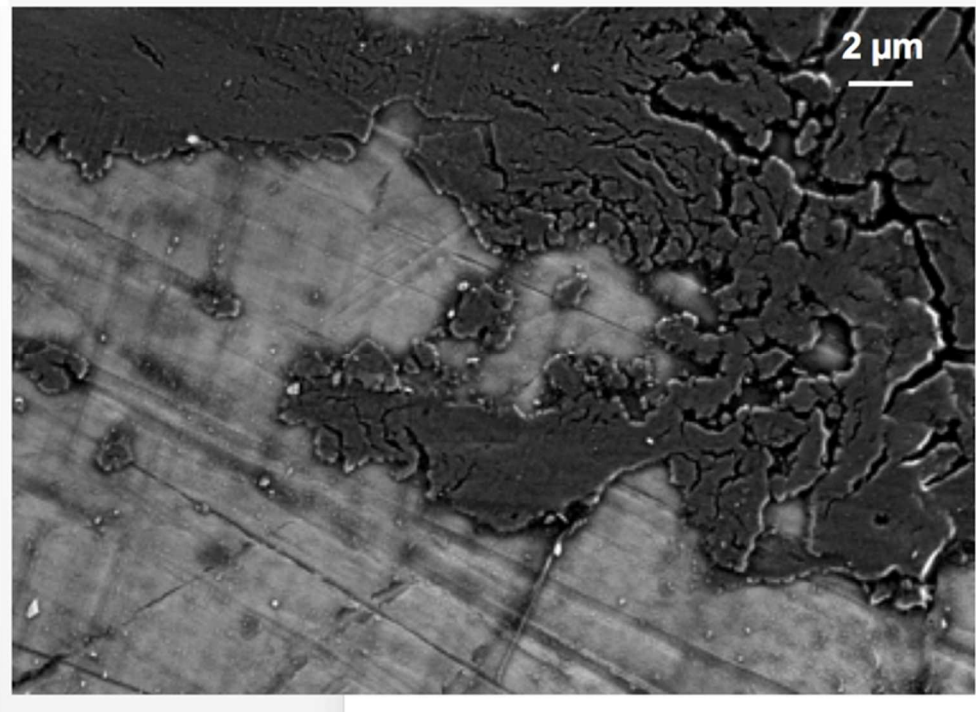


Figure 49: SEM image of the graphitic carbon tribofilm on the post-test surface.

Figure 50 highlights the higher concentration of the tribofilm specifically near areas of increased roughness of the disk, both near pre-existing scratches on the surface and near wear scratches in the direction of sliding.

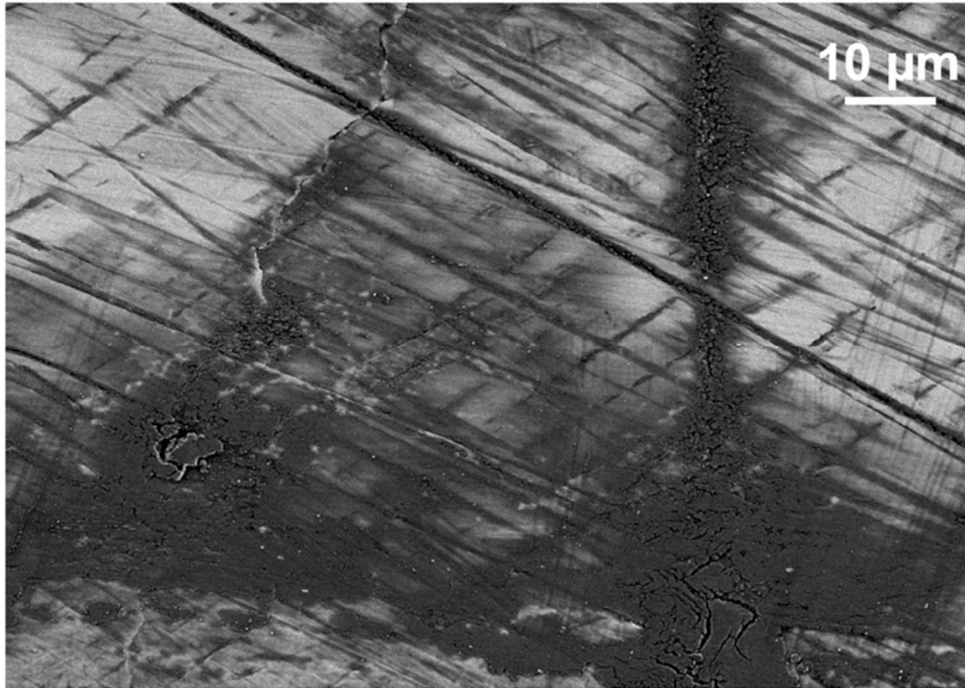


Figure 50: (a) SEM image of the post-test disk showing the carbon film filling in crevices and growing near scratches.

Figure 51 shows a closer view of the tribofilm growth on a surface scratch. The nucleation of the tribofilm seems to form at the raised ridge on the outside of the scratch, and the tribofilm grows outward, filling in the scratch and bridging the gap in some parts.

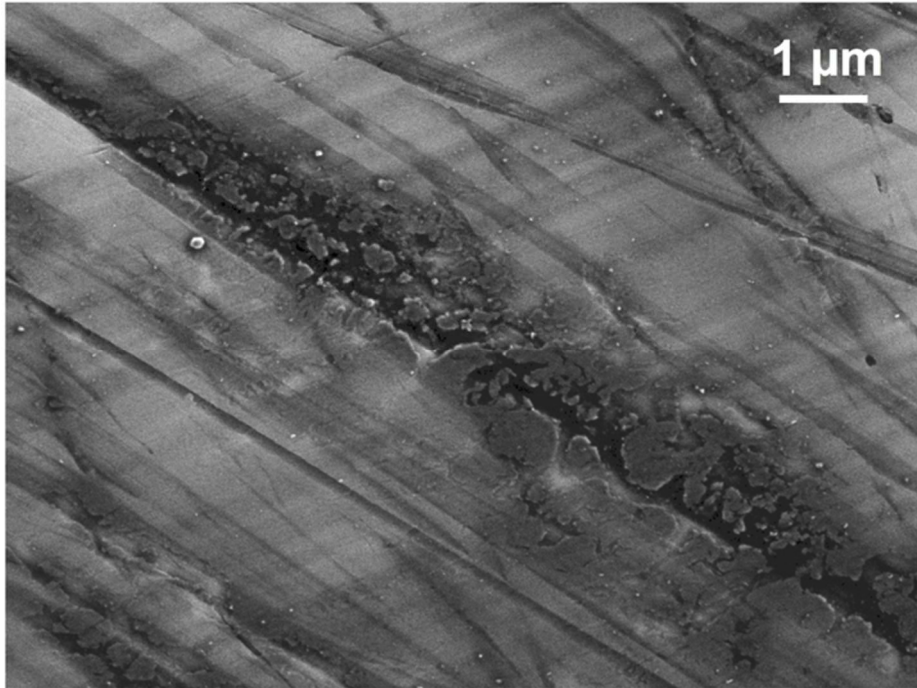


Figure 51: SEM image with a closer view of the carbon tribofilm growth near the rougher scratch on the post-test surface.

Figure 52 show the smearing of the film across the surface, filling in crevices and smoothing rough areas. The graphitic, low-shear stress carbon material is spread across the surface in the direction of motion. This shearing process is observed in other solid lubricants like silver and MoS<sub>2</sub>, and it is likely key to the friction and wear reduction of the additive, as well as the increase in smoothness of the tribofilm surface<sup>55, 173</sup>.

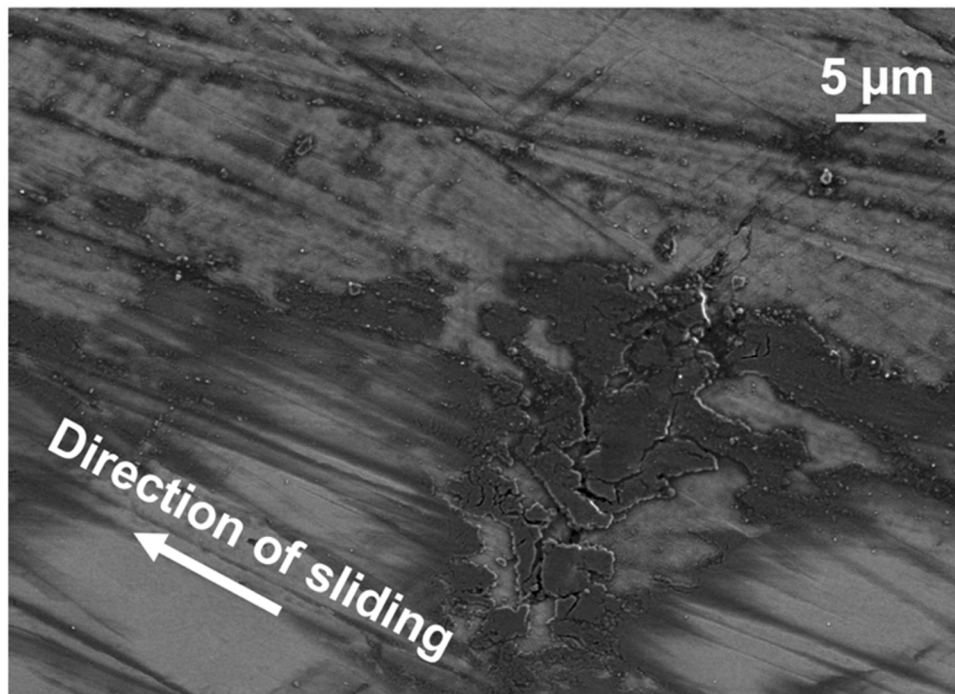


Figure 52: (a) SEM image of the post-test disk showing the smearing of the film along direction of sliding.

Figure 53 shows a high magnification image of the carbon deposit compared to a SEM image from another study on a graphite nanosheets EP additive formulation. The similarity between the two morphologies of carbon suggest that graphitic nanosheets are forming during sliding from the CPCa additive. The lubrication mechanisms reported in the nanosheets study is similar to what is found from the carbon tribofilm, but in comparison, the CPCa additive has the benefit of not requiring a dispersing agent<sup>122</sup>

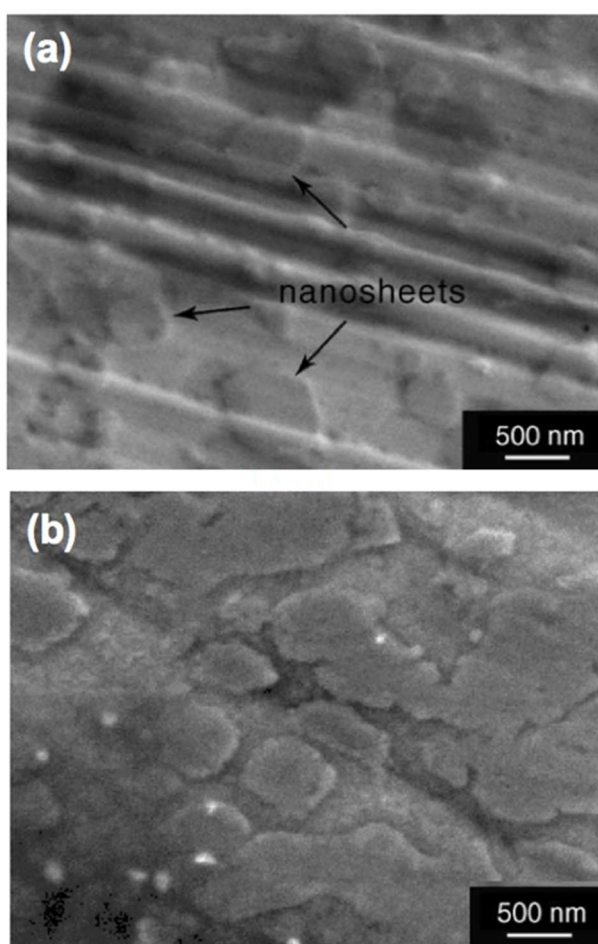


Figure 53: SEM images of dispersed graphitic nanosheets researched as an EP additive<sup>122</sup> (a) compared to the nanoscale carbon flakes present on the post-test disks (b).

Cross-sectional SEM images were also obtained using FIB milling on a disk that was lubricated with base oil and 2.5 wt % CPCa under 10 N and  $200 \text{ mm s}^{-1}$ . Figure 10 shows an SEM image taken at an approach angle of  $52^\circ$ , after milling. Before milling, a palladium overlayer was sputtered onto the surface to protect it from damage. A line-scan of EDS elemental analysis was performed across the boundary of the overlayer and the steel surface, revealing a carbon-rich tribofilm that is visible in the dark regions between the overlayer and the steel.

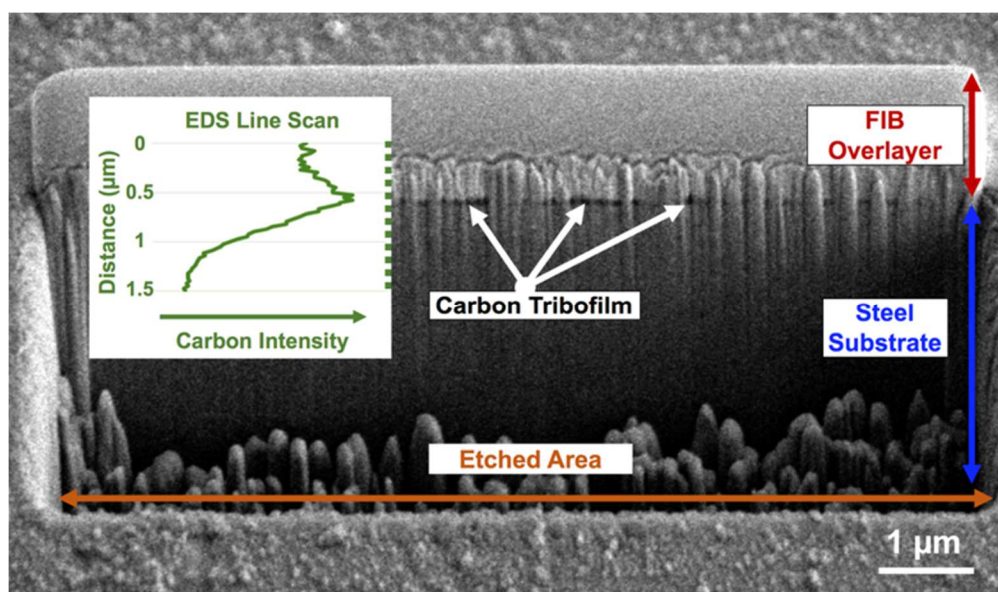


Figure 54: Cross-sectional SEM image of a post-test disk surface etched away using FIB milling, revealing the dark carbonaceous regions on the steel surface, with the protective palladium overlayer. The elemental analysis line scan for carbon is included across the surface boundaries.

Figure 55 shows Raman spectra obtained from the post-test ball surface for a variety of loading and speed conditions tested with PAO4+CPCa. Just outside the contact area, carbon films formed are thick enough to be readily detectable by Raman. Visual inspection shows that the D/G ratio increases with increasing speed and load, which indicates increasing graphiticity, consistent with previous observations made of carbon transfer layers from DLC coatings<sup>135, 161, 175</sup>. All D/G ratios indicate an amorphous carbon material similar to nanocrystalline graphite<sup>135</sup>. Also note the shift of the G peak from carbon tribofilms formed in our experiments to higher wavenumbers compared with the DLC reference sample. This shift is attributed to increased fraction of  $sp^2$  bonded carbon, indicating that carbon tribofilms formed in these experiments are more graphitic than the commercial DLC<sup>161</sup>.

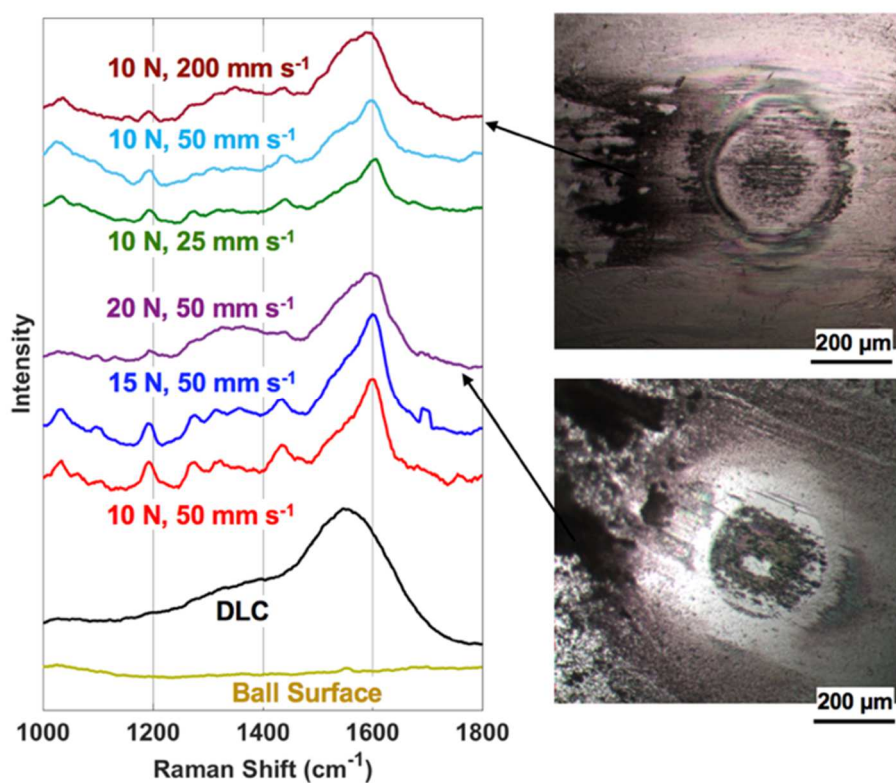


Figure 55: Raman spectra obtained from ball surfaces after testing with PAO4+CPCa

Figure 56 shows two optical micrographs of the ball surface tested with PAO4+CPCa at 15 N load and a speed of 100 mm s<sup>-1</sup>. This test condition yields a friction jump after about 10 minutes into the test as seen in Figure 40(c). Repeated tests were stopped before and immediately after the friction jump, so that images of the ball surface could be taken. Fig. 9(a) shows that before the friction jump, the surface contains a dark, mostly continuous tribofilm in the outlet area that has about the same width as the contact. Fig. 9(b) shows that after the friction jump, the film has become thinner and discontinuous.

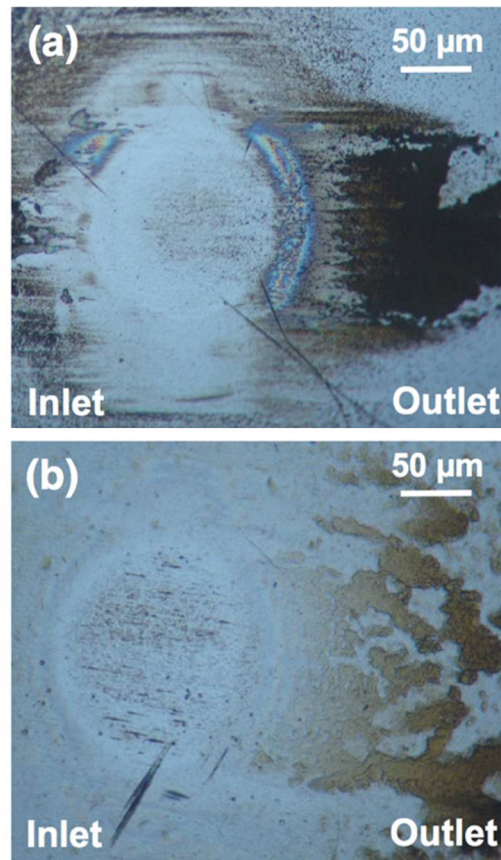


Figure 56: Optical micrographs of the ball surface after testing with PAO4+CPCa test at 15 N and 100 mm s<sup>-1</sup> (a) before the jump in friction, and (b) immediately after the jump in friction.

#### 4.3.4 Microroller Surface Analysis

Figure 57(a) shows Raman spectroscopy results and carbon peaks present for the samples containing the CPCa additives, indicating carbon produced on the surface during the microrolling process. Figure 57(b) shows how the addition of a lubricant fluid improves the consistency in width and depth of the microchannels produced the EA $\mu$ R.

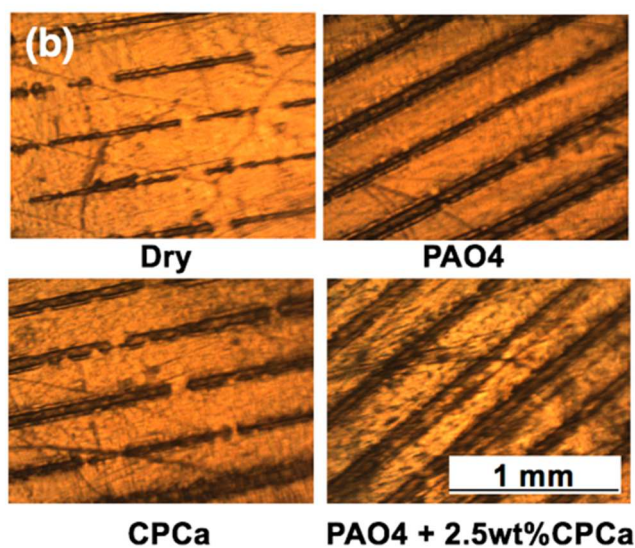
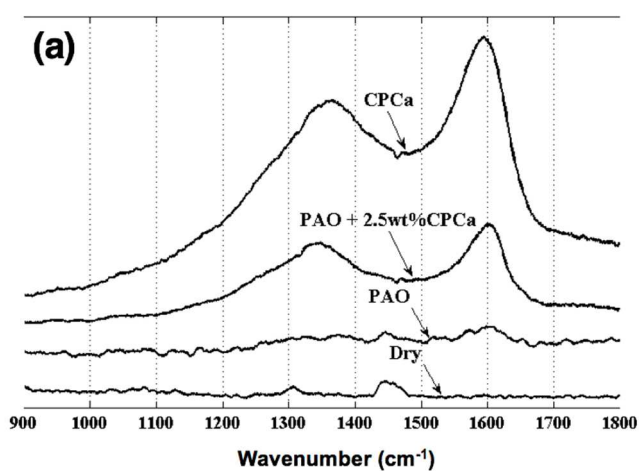


Figure 57: (a) Raman results for the steel EA $\mu$ R samples that were processed using no lubricant and lubricants with and without CPCa. (b) Microscope images of the microchannels for each sample.

### 4.3.5 Static Loading and Heating

Static tests were performed in the tribometer with apply heat and pressure and no relative motion. Raman spectroscopy for the static test ball surfaces are shown in Figure 58, with a commercial DLC surface included for comparison. The lower Raman spectrum experienced no contact pressure and 100 °C ambient temperature, and the other experience 100 °C with a downward pressure of 20 N. The Raman curves for the post-test surfaces show peaks associated with surface oxides<sup>176</sup>, but there is no significant D and G peak, and therefore no significant indication of the deposition of carbon. A similar conclusion was found in a static pressure test applied to ZDDP<sup>44</sup>. The surface that experience heat and pressure did show darkening in the contact area, due to oxidation of the metal surface.

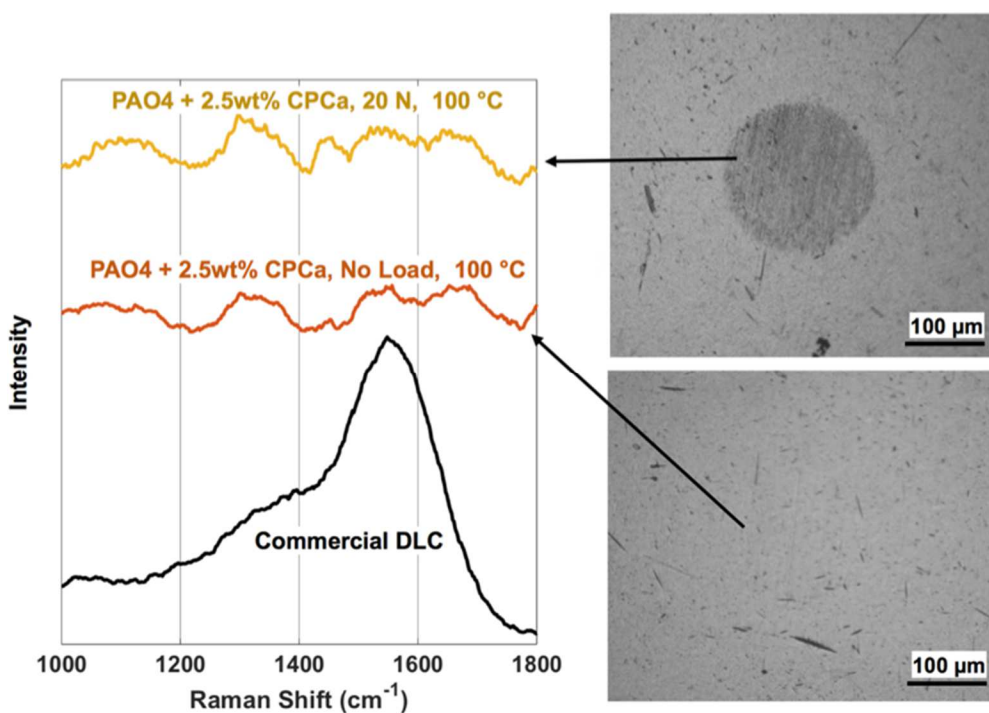


Figure 58: Surfaces and Raman spectroscopy after experiencing motionless contact at 100 °C for 30 minutes, with and without 20 N downward pressure.

The TGA-MS results shown in Figure 59 reveal what occurs when the PAO4 + 2.5 % CPCa sample is heated in ambient pressure to 300 °C. The TGA curve shows mass loss of 2.5 % at around 90 °C, which suggests removal of the CPCa from the fluid. According to the mass spectroscopy, the CPCa does not dissociate, but simply evaporates from the fluid. The MS pattern of the material leaving the chamber at 90 °C matches the standard for CPCa, as shown in Figure 59(b). The oxidation of PAO4 is also seen starting around 220 °C. This is further indication that shear stress and pressure are required for the release of carbon from the CPCa molecule.

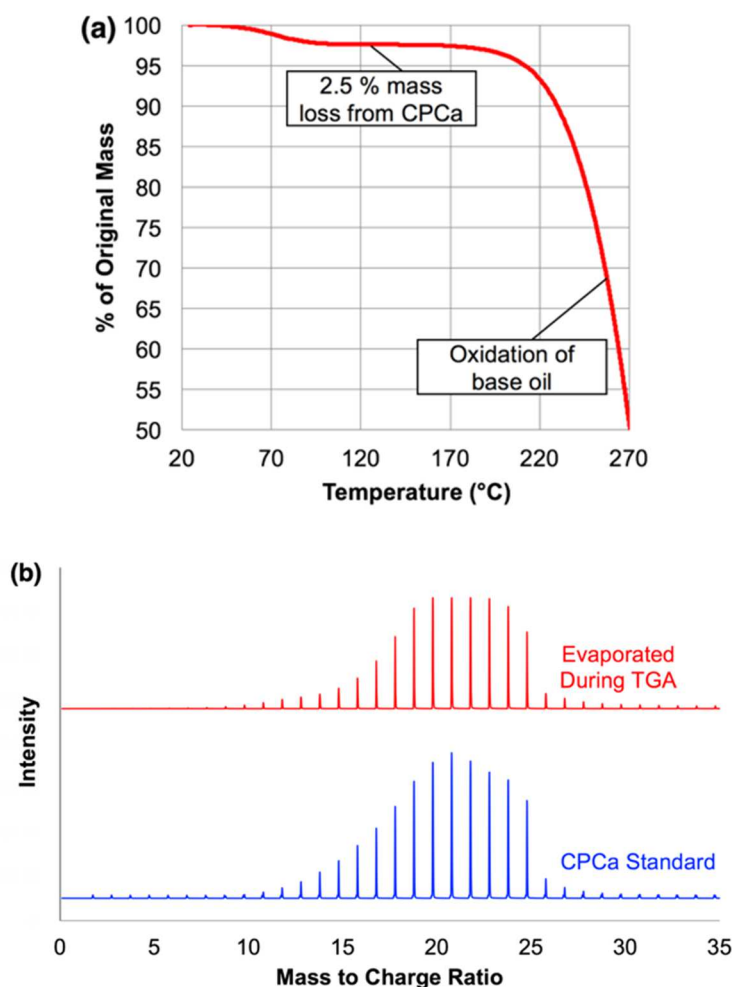


Figure 59: TGA (a) with MS (b) results for PAO4 + 2.5 wt % CPCa.

#### 4.3.6 Lubrication Mechanisms

Tribotesting and post-test analysis of the CPCa additive demonstrated the *in situ* tribochemical transformation into a carbon tribofilm that provides friction reduction and wear protection. This transformation is tribologically-induced at ambient temperatures. Based on these observations, we postulate a mechanism through which carbon films are formed from the carbon precursor additive, as shown in Figure 60. Once added to a lubricant, the precursor additive adsorbs onto the mating surfaces (Figure 60(a)). At asperity contacts, the high flash temperature and pressure trigger

fragmentation of the metastable cycloalkane (Figure 60(b)), which eventually results in the formation of carbon tribofilm (Figure 60(c)). The graphitic carbon's softness allows the films to be sheared to fill in crevices. These tribofilms are similar to previously reported graphitized DLC transfer layers in appearance, Raman signature, and friction performance<sup>143-144</sup>.

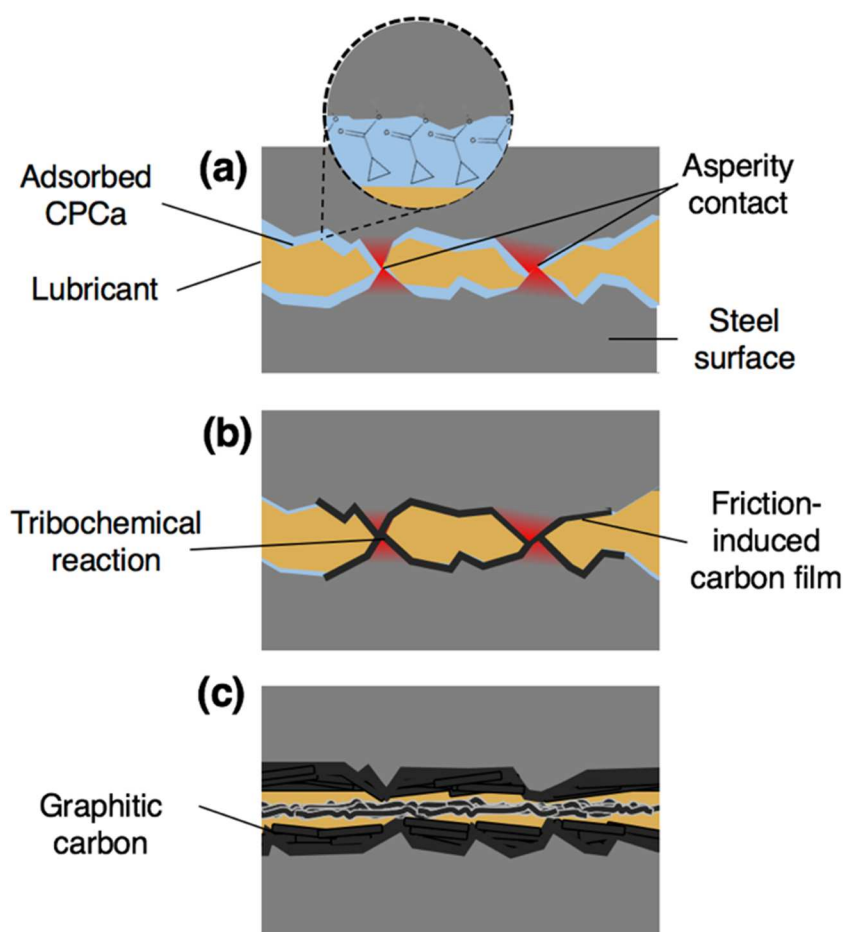


Figure 60: Mechanism of carbon formation from CPCa. (a) CPCa molecules adsorb on mating surfaces, (b) high flash temperature and pressure trigger tribochemical reaction that produces the carbon tribofilm, and (c) soft carbon tribofilm filling in the surface roughness.

### 4.3.7 Activation Energy

The activation energy for carbon tribofilm formation was approximated based on friction-time curves under a range of speed and load conditions. Steiner *et al.*<sup>165</sup> presented a model that predicts friction and wear performance of DLC that includes a method for correlating friction reduction over time with carbon tribofilm growth. It is based on the assumption that during contact, newly formed graphitic carbon accumulates inside roughness grooves of the surfaces, and friction is continually reduced until the roughness grooves are filled and coefficient of friction (COF) reaches a steady state value. Under this assumption, the difference in friction between the neat PAO4 sample and the PAO4+CPCa sample can be connected to the thickness of carbon filling in the surface roughness, as shown below.

$$\mu(t)_{PAO4+CPCa} \approx \mu_{PAO4}^{SS} - \frac{D_C}{R} \Delta\mu^{SS} \quad (4-1)$$

where  $D_C$  is the thickness of the carbon tribofilm formed within the contact area,  $\Delta\mu^{SS}$  the difference in the COF at the steady-state for the PAO4 and PAO4+CPCa samples, and  $R$  the surface roughness of the rougher surface. Figure 61 shows this relationship graphically for the 3 N, 100 mm s<sup>-1</sup> experiment.

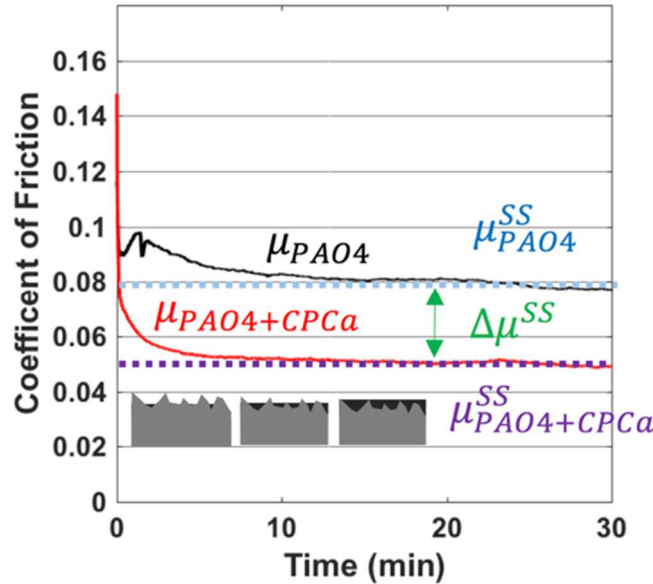


Figure 61: An example ( $3\text{N}$ ,  $200\text{mm s}^{-1}$ ) of the COF-time curve that demonstrates the difference between the PAO4 and PAO4 + CPCa samples attributed to carbon tribofilm formation.

Additionally, the friction curve for PAO4+CPCa in Figure 61 can be approximated with an exponential decay function, as shown below:

$$\mu(t)_{PAO4+CPCa} \approx \Delta\mu^{SS} e^{-\lambda t} + \mu_{PAO4+CPCa}^{SS} \quad (4-2)$$

where  $\lambda$  is the exponential decay constant, and  $t$  time of the experiment. Setting eq. 1 equal to eq. 2, one can solve for the carbon tribofilm thickness  $D_C$ :

$$D_C = R(1 - e^{-\lambda t}) \quad (4-3)$$

If  $t_{1/2}$  as the time it takes for carbon to fill in half of the surface roughness, then it can be readily shown that  $t_{1/2} = \ln 2/\lambda$ . We approximate the average growth rate of carbon  $k$  as the growth rate at  $t = t_{1/2}$  to be

$$k = \left( \frac{dD_C}{dt} \right)_{t=t_{1/2}} = \frac{R \ln 2}{2 t_{1/2}} \quad (4-4)$$

The Arrhenius plot is then constructed by plotting the natural log of  $k$  against the inverse of the flash temperature  $T^{-1}$  for each tribotest, based on the Arrhenius equation, shown in eq. 5.

$$k = k_o \exp \left( - \frac{\Delta E_{act}}{k_b T} \right) \quad (4-5)$$

where  $\Delta E_{act}$  is the activation,  $k_o$  is a pre-exponential factor,  $k_b$  is the Boltzmann constant, and  $T$  is the predicted flash temperature. A valid Arrhenius plot should have a linear trend, the slope of which is used to find the activation energy of a reaction. In order to validate the assumptions made for obtaining  $k$ , additional tribotests were performed on disks polished to different roughness values, which are plugged in to eq. 3. The Arrhenius plot, shown in Figure 62, remains linear regardless of surface roughness, which reinforces the validity of the tribofilm growth model.

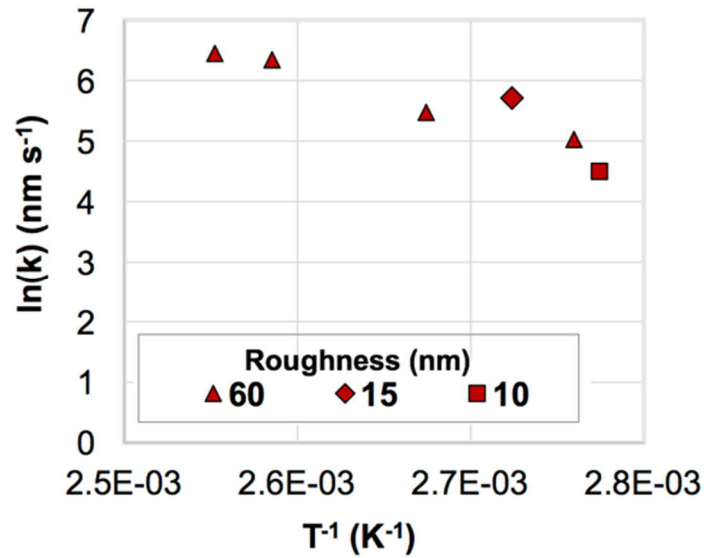


Figure 62: Arrhenius plot of the natural log of the growth rate against the inverse of the absolute temperature, for the 10 N tests performed with disks polished to different roughnesses.

A collection of these Arrhenius plots is shown in Figure 63(a) for each testing load. In tribochemical reactions, including those involving carbon<sup>143</sup>, shear stress decreases the activation energy barrier for the reaction<sup>147, 177-180</sup>, thus accelerating the tribochemical reaction. Therefore, this factor was incorporated the calculation. The shear stress affects activation energy based on the following equation,

$$\Delta E_{act} = \Delta E_{act,o} - \sigma \Delta V_{act} \quad (4-6)$$

where  $\Delta E_{act}$  is the activation energy with shear stress,  $\Delta E_{act,o}$  is activation energy without stress,  $\sigma$  is the shear stress,  $\Delta V_{act}$  the activation volume<sup>18, 180</sup>. Shear stress for each test was approximated by multiplying the normal contact stress by the steady-state coefficient of friction<sup>181</sup>. Here, the

activation volume depends on molecular deformation, and the shape of the potential energy surfaces associated with initial and transition states of such a tribochemical reaction, not any physical volume of the molecule. For each test,  $\Delta E_{\text{act}}$  is determined from the slopes on the Arrhenius plots in Figure 63(a). Figure 63(b) shows how the  $\Delta E_{\text{act}}$  varies with shear stress. Based on eq. 6, the y-intercept of this plot is  $\Delta E_{\text{act},0}$ , the activation energy under zero shear stress, which is approximated to be 223.5 kJ/mole. Remarkably, this value compares well with the reported value of C-C bond dissociation within cyclopropane (257 kJ/mole)<sup>182</sup>, and also the dissociation energy of CPCa (249 kJ/mole)<sup>183</sup>. This match suggests that the opening of the cyclopropane ring is the rate-limiting step in carbon tribofilm formation from the decomposition of CPCa.

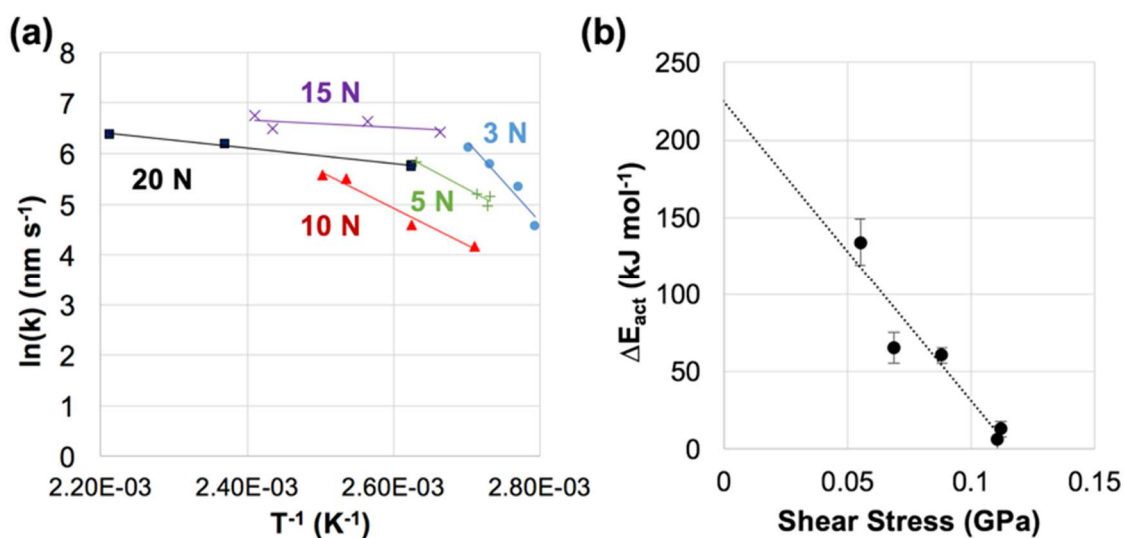


Figure 63: (a) Arrhenius plots of the natural log of growth rate against the inverse of temperature for different loads; (b) Variation of activation energy for carbon tribofilm formation versus contact pressure.

#### 4.4 Chapter 4 Conclusions

This chapter reported the development of a novel technique for carbon tribofilm lubrication using cyclopropanecarboxylic acid (CPCa), a carbon precursor additive molecule that dissolves in oil, adsorbs on contact surfaces, and undergoes a tribochemical transformation into a lubricious graphitic tribofilm. The following can be concluded.

- 1) Addition of 2.5 wt % of CPCa to PAO4 results in an average 18 % reduction in friction and 93 % reduction in wear rate. SEM images of the post-test surfaces show that carbon is generated near areas of high asperity contact, filling in rough areas of the surface. The tribofilm is also sheared across the surface in the direction of sliding.
- 2) Raman spectroscopy and nanoindentation confirmed that the tribofilm consists of a relatively soft and amorphous graphitic material.
- 3) The activation energy of carbon tribofilm formation was determined to be  $223.5 \text{ kJ mol}^{-1}$ , which is close to the C-C bond dissociation energy in cyclopropane within CPCa.

This study suggests a new strategy to providing replenishable carbon films for on-demand lubrication without resorting to special surface modification methods.

## Chapter 5: Conclusions

The research in this dissertation is part of a recent shift in focus in the development of lubricant additives where empirical guesswork is being replaced by more precise, fundamental knowledge, and more consideration is being given to the environmental impact of the additives. This advancement is the result of an increased understanding of the thermodynamic, chemical, and mechanical phenomena at the contacting interfaces in relative motion, and the aid of advanced computer modeling and MD simulations. The results of this research can be summarized as follows:

1. Three lubricant additives presented in this report are direct results of that process. Each additive was designed to perform a specialized function, and the molecule structure of each additive was carefully selected based on its expected behavior in the tribological environment.
2. The organosilver solid lubricant additive provides a combination of extreme temperature solid lubrication with strong oil solubility, giving a best-of-both-worlds option to any application that requires on-demand high temperature lubrication. Temperature-ramped ball-on-disk experiments revealed the additive's low-friction performance at temperatures greater than  $\sim 275$  °C, after both the PAO4 and FF oil failed. The transition from oil as primary lubricant to metallic silver as primary lubricant is seamless. SEM and EDS analyses show that metallic silver is primarily deposited in wear scars, indicating that high temperature caused by asperity contacts increases the probability of thermolysis for the additive. The metallic silver acts as a protective buffer material between the contacting surfaces.

3. The organosilane sand dispersant additive works towards solving potentially damaging external contamination issues by bonding to silica surfaces and reducing abrasiveness and agglomeration. The additive is molecularly engineered to form *in situ* covalent bonds with the oxide surfaces as they enter a tribological system, increase the solubility of sand in oil and reducing agglomeration of sand particles. Friction and wear increases from contamination of two sizing grades of test sand were mitigated by the use of the additive.
4. A novel technique for carbon tribofilm lubrication was demonstrated using cyclopropanecarboxylic acid (CPCa), a carbon precursor additive molecule that dissolves in oil, adsorbs on contact surfaces, and undergoes a tribochemical transformation into a lubricious graphitic tribofilm. The addition of 2.5 wt % of CPCa to PAO4 results in an average 18 % reduction in friction and 93 % reduction in wear rate. SEM, Raman Spectroscopy and nanoindentation confirmed that the tribofilm consists of a relatively soft and amorphous graphitic material. The activation energy of carbon tribofilm formation was determined to be  $223.5 \text{ kJ mol}^{-1}$ , which is close to the C-C bond dissociation energy in cyclopropane within CPCa. The low-cost additive has boundless potential, both as an engine lubrication additive, and in other applications like manufacturing and surface coatings.
5. The three proposed additive technologies show promising potential, and with continued development, their benefits can be appreciated in more and more applications.

## **Chapter 6: Future Work**

### **6.1 Organosilver Solid Lubricant Precursor Molecule**

The continuing objective of the research into the organosilver solid lubricant precursor will involve the design, synthesis, and characterization of new organometallic complexes that are quicker and easier to synthesize and more efficient at depositing lubricious metallic films than the previous Gen. IV additive. Silver is an expensive raw material, and increased efficiency is persistently an objective. Also, exploration will also be made into incorporation of other non-toxic soft, lubricious metals, such as In, Cu, Ni, and Au.

### **6.2 Organosilane Sand Dispersant**

Future work on sand surfactants will involve continued improvement in the molecular design of the additive in order to enable an easier reaction with sand particle and enhanced oil-solubility. Additionally, the additive will be coupled with specialized catalytic nanoparticle air filters that promote the tribochemical reaction and provide a complete contamination solution. Another future task is the evaluation of the additive in a fully formulated oil, in order to investigate whether functional interference will occur with other additives in formulated oils.

### **6.3 Novel Carbon Tribofilm Additive**

As the carbon tribofilm additive is continually developed, a molecular dynamics model should be conducted to reveal explicit details into the reaction pathway between a given additive molecule and the resulting carbon tribofilm. Additionally, extended timescale tribometer test (>24hrs)

should examine how long the effectiveness of the carbon coating lasts under boundary lubrication. One additional design choice for the additive that will be explored is size of the additive molecule. Since thermal energy is coupled to the metastable carbon ring from the surface, if one or more organic groups  $R$  such as  $-\text{CH}_2$  are inserted between the metastable carbon ring and the surface-active, then the  $R$  group spacer would dissipate some of the thermal energy coming from the surface and away from the metastable carbon ring, making the latter more stable against thermal decomposition. This allows the control of the decomposition kinetics by simply changing the number of such spacers between the surface-active end and the metastable carbon ring for partial thermal energy dissipation.

## References

1. Schwarz, U. D., Tracking antiwear film formation. *Science* **2015**, *348* (6230), 40-41.
2. Nosonovsky, M.; Bhushan, B.; SpringerLink (Online service), *Green tribology : biomimetics, energy conservation and sustainability*. Springer: Berlin ; New York, 2012; p online resource (1 volume.).
3. Holmberg, K.; Andersson, P.; Nylund, N.-O.; Mäkelä, K.; Erdemir, A., Global energy consumption due to friction in trucks and buses. *Tribol. Int.* **2014**, *78* (0), 94-114.
4. Holmberg, K.; Siilasto, R.; Laitinen, T.; Andersson, P.; Jäsberg, A., Global energy consumption due to friction in paper machines. *Tribol. Int.* **2013**, *62* (0), 58-77.
5. Russell, L. S. D. J. A., A Review of DOE ECUT Tribology. *J. Tribol* **1986**, *108* (4), 497-501.
6. McFadden, C.; Soto, C.; Spencer, N. D., Adsorption and surface chemistry in tribology. *Tribology International* **1997**, *30* (12), 881-888.
7. Jost, H. P., Tribology—origin and future. *Wear* **1990**, *136* (1), 1-17.
8. Jost, H. P.; Schofield, J., Energy saving through tribology: a techno-economic study. *Proceedings of the Institution of Mechanical Engineers* **1981**, *195* (1), 151-173.
9. Wang, Q.; Chung, Y.-w., *Encyclopedia of tribology*. Springer New York: 2013.
10. Habchi, W.; Matta, C.; Joly-Pottuz, L.; De Barros, M.; Martin, J.; Vergne, P., Full film, boundary lubrication and tribochemistry in steel circular contacts lubricated with glycerol. *Tribology Letters* **2011**, *42* (3), 351.
11. Felts, J. R.; Oyer, A. J.; Hernández, S. C.; Whitener Jr, K. E.; Robinson, J. T.; Walton, S. G.; Sheehan, P. E., Direct mechanochemical cleavage of functional groups from graphene. *Nature communications* **2015**, *6*.
12. Nakayama, K.; Martin, J.-M., Tribochemical reactions at and in the vicinity of a sliding contact. *Wear* **2006**, *261* (3), 235-240.
13. Nakayama, K., The plasma generated and photons emitted in an oil-lubricated sliding contact. *Journal of Physics D: Applied Physics* **2007**, *40* (4), 1103.
14. Nakayama, K., Triboemission of charged particles from various solids under boundary lubrication conditions. *Wear* **1994**, *178* (1-2), 61-67.

15. Hsu, S.; Klaus, E.; Cheng, H., A mechano-chemical descriptive model for wear under mixed lubrication conditions. *Wear* **1988**, *128* (3), 307-323.
16. Kajdas, C. K., Importance of the triboemission process for tribochemical reaction. *Tribology International* **2005**, *38* (3), 337-353.
17. Ghasemi, H.; Furey, M.; Kajdas, C., Surface temperatures and fretting corrosion of steel under conditions of fretting contact. *Wear* **1993**, *162*, 357-369.
18. Gosvami, N.; Bares, J.; Mangolini, F.; Konicek, A.; Yablon, D.; Carpick, R., Mechanisms of antiwear tribofilm growth revealed in situ by single-asperity sliding contacts. *Science* **2015**, *348* (6230), 102-106.
19. Haque, T.; Morina, A.; Neville, A.; Kapadia, R.; Arrowsmith, S., Study of the ZDDP antiwear tribofilm formed on the DLC coating using AFM and XPS techniques. *Journal of ASTM International* **2007**, *4* (7), 1-11.
20. Archard, J. In *Elastic deformation and the laws of friction*, Proceedings of the Royal Society of London A: Mathematical, Physical and Engineering Sciences, The Royal Society: 1957; pp 190-205.
21. Moras, G.; Pastewka, L.; Gumbsch, P.; Moseler, M., Formation and oxidation of linear carbon chains and their role in the wear of carbon materials. *Tribology Letters* **2011**, *44* (3), 355.
22. Felts, J. R.; Oyer, A. J.; Hernández, S. C.; Whitener Jr, K. E.; Robinson, J. T.; Walton, S. G.; Sheehan, P. E., Direct mechanochemical cleavage of functional groups from graphene. *Nature communications* **2015**, *6*, 6467.
23. Priest, M.; Taylor, C., Automobile engine tribology—approaching the surface. *Wear* **2000**, *241* (2), 193-203.
24. Bishop, J.; Nedungadi, A.; Ostrowski, G.; Surampudi, B.; Armiroli, P.; Taspinar, E. *An engine start/stop system for improved fuel economy*; SAE Technical Paper: 2007.
25. Tanaka, K.; Korematsu, K.; Yamazaki, Y. In *Study on intelligent idling stop system*, 2000 FISITA World Automotive Congress: Automotive Innovation for the New Millennium, Seoul, 2000; pp 1-4.
26. Holmberg, K.; Erdemir, A., Influence of tribology on global energy consumption, costs and emissions. *Friction* **2017**, *5* (3), 263-284.
27. Outlook, A. E., Energy information administration. *Department of Energy* **2010**, *92010* (9), 1-15.
28. Holmberg, K.; Andersson, P.; Erdemir, A., Global energy consumption due to friction in passenger cars. *Tribol. Int.* **2012**, *47* (0), 221-234.

29. Tung, S. C.; McMillan, M. L., Automotive tribology overview of current advances and challenges for the future. *Tribol. Int.* **2004**, *37* (7), 517-536.
30. Taylor, C., Automobile engine tribology—design considerations for efficiency and durability. *Wear* **1998**, *221* (1), 1-8.
31. Khorramian, B.; Iyer, G.; Kodali, S.; Natarajan, P.; Tupil, R., Review of antiwear additives for crankcase oils. *Wear* **1993**, *169* (1), 87-95.
32. Marr, L. C.; Kirchstetter, T. W.; Harley, R. A.; Miguel, A. H.; Hering, S. V.; Hammond, S. K., Characterization of polycyclic aromatic hydrocarbons in motor vehicle fuels and exhaust emissions. *Environmental science & technology* **1999**, *33* (18), 3091-3099.
33. Carnes, K., Additive Trends: Zapping SAPS, Cutting Costs & Tackling Toxins. *Tribology & lubrication technology* **2005**, *61* (9), 32.
34. Doig, M.; Warrens, C. P.; Camp, P. J., Structure and friction of stearic acid and oleic acid films adsorbed on iron oxide surfaces in squalane. *Langmuir* **2013**, *30* (1), 186-195.
35. Neville, A.; Haque, T.; Morina, A., Friction and its importance in fuel economy—probing the nanoscale characteristics of surfaces in order to understand lubricant/surface interactions. *Journal of Physics: Condensed Matter* **2008**, *20* (35), 354019.
36. Barthel, A. J.; Kim, S. H., Lubrication by physisorbed molecules in equilibrium with vapor at ambient condition: effects of molecular structure and substrate chemistry. *Langmuir* **2014**, *30* (22), 6469-6478.
37. Kajdas, C., On a negative-ion concept of EP action of organo-sulfur compounds. *ASLE transactions* **1985**, *28* (1), 21-30.
38. Moon, M., How clean are your lubricants? *Trends in Food Science & Technology* **2007**, *18*, Supplement 1, S74-S79.
39. Williams, J. A., Wear and wear particles—some fundamentals. *Tribology International* **2005**, *38* (10), 863-870.
40. Archard, J., Contact and rubbing of flat surfaces. *Journal of applied physics* **1953**, *24* (8), 981-988.
41. Zum Gahr, K.-H., Wear by hard particles. *Tribology International* **1998**, *31* (10), 587-596.
42. Eyre, T., Wear characteristics of metals. *Tribology International* **1976**, *9* (5), 203-212.
43. George, S.; Balla, S.; Gautam, V.; Gautam, M., Effect of diesel soot on lubricant oil viscosity. *Tribology international* **2007**, *40* (5), 809-818.

44. Martin, J. M.; Onodera, T.; Minfray, C.; Dassenoy, F.; Miyamoto, A., The origin of anti-wear chemistry of ZDDP. *Faraday discussions* **2012**, *156* (1), 311-323.
45. Zhang, J.; Spikes, H., On the mechanism of ZDDP antiwear film formation. *Tribology Letters* **2016**, *63* (2), 1-15.
46. Pawlak, Z., *Tribochemistry of Lubricating Oils*. Elsevier: Amsterdam London, 2003; p xiv, 368 p.
47. Kalin, M.; Mora, F. G., *Advances in boundary lubrication and boundary surface films*. Elsevier: 2011.
48. Hermance, H.; Egan, T., Organic deposits on precious metal contacts. *Bell Labs Technical Journal* **1958**, *37* (3), 739-776.
49. Gunsel, S.; Klaus, E.; Bruce, R. *Friction characteristics of vapor deposited lubricant films*; 0148-7191; SAE Technical Paper: 1989.
50. Elo, R.; Jacobson, S., Formation and breakdown of oil residue tribofilms protecting the valves of diesel engines. *Wear* **2015**, *330*, 193-198.
51. Morina, A.; Neville, A., Understanding the composition and low friction tribofilm formation/removal in boundary lubrication. *Tribology International* **2007**, *40* (10), 1696-1704.
52. Totolin, V.; Ripoll, M. R.; Jech, M.; Podgornik, B., Enhanced tribological performance of tungsten carbide functionalized surfaces via in-situ formation of low-friction tribofilms. *Tribology International* **2016**, *94*, 269-278.
53. Sliney, H. E., Solid lubricant materials for high temperatures—a review. *Tribology International* **1982**, *15* (5), 303-315.
54. Rudnick, L. R., *Lubricant Additives: Chemistry and Applications*. CRC Press: 2010.
55. Clauss, F. J., *Solid lubricants and self-lubricating solids*. Elsevier: 2012.
56. Scharf, T. W.; Prasad, S. V., Solid Lubricants: A Review. *Journal of Materials Science* **2013**, (48), 511-531.
57. Inman, I. A.; Datta, S.; Du, H. L.; Burnell-Gray, J. S.; Luo, Q., Microscopy of Glazed Layers Formed During High Temperature Sliding Wear at 750° C. *Wear* **2003**, *254* (5), 461-467.
58. Mulligan, C. P.; Papi, P. A.; Gall, D., Ag Transport in CrN–Ag Nanocomposite Coatings. *Thin Solid Films* **2012**, *520* (22), 6774-6779.
59. Erck, R. A.; Erdemir, A.; Fenske, G. R., Effect of Film Adhesion on Tribological Properties of Silver-Coated Alumina. *Surface and Coatings Technology* **1990**, *43* (44), 577-587.

60. Baraket, M.; Mercks, D.; Zhang, Z. G.; Coddet, C., Mechanical and Tribological Properties of CrN/Ag and CrSiN/Ag Nanoscale Multilayers. *Surface and Coatings Technology* **2010**, *204* (15), 2386-2391.
61. McCain, M. N.; Schneider, S.; Salata, M. R.; Marks, T. J., Tris(phosphino)borato Silver(I) Complexes as Precursors for Metallic Silver Aerosol-Assisted Chemical Vapor Deposition. *Inorganic Chemistry* **2008**, *47* (7), 2534-2542.
62. Baoyu, S.; Feng, Z.; Xining, W.; Jianjun, Q., Study of Anti-Contact Fatigue Performance of Lubricant with Nano Silver Particles. *Lubrication Engineering* **2004**, *5* (165), 23-24.
63. Sun, L.; Zhang, Z. J.; Wu, Z. S.; Dang, H. X., Synthesis and Characterization of DDP Coated Ag Nanoparticles. *Materials Science and Engineering A* **2004**, *379* (1), 378-383.
64. Li, X.; Cao, Z.; Zhang, Z.; Dang, H., Surface-modification in situ of nano-SiO<sub>2</sub> and its structure and tribological properties. *Applied Surface Science* **2006**, *252* (22), 7856-7861.
65. Ma, J.; Mo, Y.; Bai, M., Effect of Ag Nanoparticles Additive on the Tribological Behavior of Multialkylated Cyclopentanes (MACs). *Wear* **2009**, *266* (7-8), 627-631.
66. Sun, L.; Tao, X.; Zhao, Y.; Zhang, Z., Synthesis and Tribology Properties of Stearate-Coated Ag Nanoparticles. *Tribology Transactions* **2010**, *53* (2), 174-178.
67. Williams, J.; Hyncica, A., Mechanisms of abrasive wear in lubricated contacts. *Wear* **1992**, *152* (1), 57-74.
68. Twist, C.; Bassanetti, I.; Snow, M.; Delferro, M.; Bazzi, H.; Chung, Y.-W.; Marchió, L.; Marks, T.; Wang, Q. J., Silver-Organic Oil Additive for High-Temperature Applications. *Tribology Letters* **2013**, *52* (2), 261-269.
69. Bassanetti, I.; Twist, C. P.; Kim, M.-G.; Seyam, A. M.; Bazzi, H. S.; Wang, Q. J.; Chung, Y.-W.; Marchió, L.; Delferro, M.; Marks, T. J., Synthesis and Characterization of Silver(I) Pyrazolylmethylpyridine Complexes and Their Implementation as Metallic Silver Thin Film Precursors. *Inorganic Chemistry* **2014**, *53* (9), 4629-4638.
70. Twist, C. P.; Seyam, A. M.; Chen, C.; Kim, M.-G.; Weberski, M. P.; Ren, N.; Marks, T. J.; Chung, Y.-W.; Wang, Q. J., Molecularly-Engineered Lubricants: Synthesis, Activation, and Tribological Characterization of Silver Complexes as Lubricant Additives. *Advanced Engineering Materials* **2012**, *14* (1-2), 101-105.
71. Twist, C. P.; Seyam, A. M.; Chen, C.; Kim, M.-G.; Weberski, M. P.; Ren, N.; Marks, T. J.; Chung, Y.-W.; Wang, Q. J., Molecularly-Engineered Lubricants: Synthesis, Activation, and Tribological Characterization of Silver Complexes as Lubricant Additives. *Adv. Eng. Mater.* **2012**, *14* (1-2), 101-105.

72. Twist, C. P.; Bassanetti, I.; Snow, M.; Delferro, M.; Bazzi, H.; Chung, Y.-W.; Marchió, L.; Marks, T. J.; Jane Wang, Q., Silver-Organic Oil Additive for High-Temperature Applications. *Tribol. Lett.* **2013**, *52* (2), 261-269.
73. Bassanetti, I.; Twist, C. P.; Kim, M.-G.; Seyam, A. M.; Bazzi, H. S.; Wang, Q. J.; Chung, Y.-W.; Marchió, L.; Delferro, M.; Marks, T. J., Synthesis and characterization of silver(I) pyrazolylmethylpyridine complexes and their implementation as metallic silver thin film precursors. *Inorg. Chem.* **2014**, *53* (9), 4629-4638.
74. Asseff, P. A. Lubricant. US 2261047 A, 1941.
75. Desanker, M.; Johnson, B.; Seyam, A. M.; Chung, Y.-W.; Bazzi, H. S.; Delferro, M.; Marks, T. J.; Wang, Q. J., Oil-Soluble Silver–Organic Molecule for in Situ Deposition of Lubricious Metallic Silver at High Temperatures. *ACS applied materials & interfaces* **2016**, *8* (21), 13637-13645.
76. Liu, S.; Wang, Q., A three-dimensional thermomechanical model of contact between non-conforming rough surfaces. *Journal of tribology* **2001**, *123* (1), 17-26.
77. Zhu, D.; Cheng, H., Effect of surface roughness on the point contact EHL. *Journal of tribology* **1988**, *110* (1), 32-37.
78. Spikes, H. A., Mixed Lubrication — an Overview. *Lubrication Science* **1997**, *9* (3), 221-253.
79. Khorramian, B. A.; Iyer, G. R.; Kodali, S.; Natarajan, P.; Tupil, R., Review of Antiwear Additives for Crankcase Oils. *Wear* **1993**, *169* (1), 87-95.
80. Maru, M. M.; Castillo, R. S.; Padovese, L. R., Study of solid contamination in ball bearings through vibration and wear analyses. *Tribology International* **2007**, *40* (3), 433-440.
81. Qi, J.; Wang, L.; Wang, Y.; Pu, J.; Yan, F.; Xue, Q., The tribological performance of selected solid lubricant films in sand-dust environments. *Wear* **2011**, *271* (5), 899-910.
82. Liu, M.; Jiang, G.; Li, L.; Li, Y.; Gao, L.; Niu, S., Control of sandstorms in Inner Mongolia, China. *Environmental Conservation* **2004**, *31* (04), 269-273.
83. Qi, J.; Liu, H.; Luo, Y.; Zhang, D.; Wang, Y., Influences of added sand-dust particles on the tribological performance of graphite-like coating under solid–liquid lubrication. *Tribology International* **2014**, *71*, 69-81.
84. Woldman, M.; Van Der Heide, E.; Schipper, D.; Tinga, T.; Masen, M., Investigating the influence of sand particle properties on abrasive wear behaviour. *Wear* **2012**, *294*, 419-426.

85. Durant, S.; Wachter, T.; Bashir, S.; Woodroffe, R.; Ornellas, P.; Ransom, C.; Newby, J.; Abáigar, T.; Abdelgadir, M.; El Alqamy, H., Fiddling in biodiversity hotspots while deserts burn? Collapse of the Sahara's megafauna. *Diversity and Distributions* **2014**, *20* (1), 114-122.
86. Miri, A.; Ahmadi, H.; Ghanbari, A.; Moghaddamnia, A., Dust storms impacts on air pollution and public health under hot and dry climate. *Int J Energy Environ* **2007**, *2* (1), 101-105.
87. Gaier, J. R., The effects of lunar dust on EVA systems during the Apollo missions. *NASA/TM* **2005**, *213610*, 2005.
88. Gies, J. V., Effect of the lunar surface environment upon machinery. *ASCE, NEW YORK, NY,(USA)*. **1996**, *1*, 639-645.
89. Sin, H.; Saka, N.; Suh, N., Abrasive wear mechanisms and the grit size effect. *Wear* **1979**, *55* (1), 163-190.
90. Gählin, R.; Jacobson, S., The particle size effect in abrasion studied by controlled abrasive surfaces. *Wear* **1999**, *224* (1), 118-125.
91. Misra, A.; Finnie, I., On the size effect in abrasive and erosive wear. *Wear* **1981**, *65* (3), 359-373.
92. Broz, M. E.; Cook, R. F.; Whitney, D. L., Microhardness, toughness, and modulus of Mohs scale minerals. *American Mineralogist* **2006**, *91* (1), 135-142.
93. Mohan, N.; Sharma, M.; Singh, R.; Kumar, N. *Tribological Performance of Lubricating Oil Contaminated with Fine Dust Particles*; 0148-7191; SAE Technical Paper: 2014.
94. Alcock, N. W., *Bonding and structure: structural principles in inorganic and organic chemistry*. Ellis Horwood Limited: 1990.
95. Molazemhosseini, A.; Tourani, H.; Naimi-Jamal, M.; Khavandi, A., Nanoindentation and nanoscratching responses of PEEK based hybrid composites reinforced with short carbon fibers and nano-silica. *Polymer Testing* **2013**, *32* (3), 525-534.
96. Hong, B.; Panagiotopoulos, A. Z., Molecular dynamics simulations of silica nanoparticles grafted with poly (ethylene oxide) oligomer chains. *The Journal of Physical Chemistry B* **2012**, *116* (8), 2385-2395.
97. Rudnick, L. R., *Lubricant additives: chemistry and applications*. CRC Press: 2009.
98. Plimpton, S., Fast parallel algorithms for short-range molecular dynamics. *Journal of computational physics* **1995**, *117* (1), 1-19.

99. Wick, C. D.; Martin, M. G.; Siepmann, J. I., Transferable potentials for phase equilibria. 4. United-atom description of linear and branched alkenes and alkylbenzenes. *The Journal of Physical Chemistry B* **2000**, *104* (33), 8008-8016.
100. Martin, M. G.; Siepmann, J. I., Transferable potentials for phase equilibria. 1. United-atom description of n-alkanes. *The Journal of Physical Chemistry B* **1998**, *102* (14), 2569-2577.
101. Barbier, D.; Brown, D.; Grillet, A.-C.; Neyertz, S., Interface between end-functionalized PEO oligomers and a silica nanoparticle studied by molecular dynamics simulations. *Macromolecules* **2004**, *37* (12), 4695-4710.
102. Pujari, S. P.; Scheres, L.; Marcelis, A.; Zuilhof, H., Covalent surface modification of oxide surfaces. *Angewandte Chemie International Edition* **2014**, *53* (25), 6322-6356.
103. Stein, A.; Melde, B. J.; Schroden, R. C., Hybrid inorganic–organic mesoporous silicates—nanoscopic reactors coming of age. *Advanced Materials* **2000**, *12* (19), 1403-1419.
104. Huh, S.; Wiench, J. W.; Yoo, J.-C.; Pruski, M.; Lin, V. S.-Y., Organic functionalization and morphology control of mesoporous silicas via a co-condensation synthesis method. *Chemistry of materials* **2003**, *15* (22), 4247-4256.
105. Britcher, L. G.; Kehoe, D. C.; Matisons, J. G.; Swincer, A. G., Siloxane coupling agents. *Macromolecules* **1995**, *28* (9), 3110-3118.
106. Haukka, S.; Lakomaa, E. L.; Root, A., An IR and NMR study of the chemisorption of titanium tetrachloride on silica. *The Journal of Physical Chemistry* **1993**, *97* (19), 5085-5094.
107. Sander, L. C.; Callis, J. B.; Field, L. R., Fourier transform infrared spectrometric determination of alkyl chain conformation on chemically bonded reversed-phase liquid chromatography packings. *Analytical Chemistry* **1983**, *55* (7), 1068-1075.
108. Bhushan, B.; Nosonovsky, M., Comprehensive model for scale effects in friction due to adhesion and two-and three-body deformation (plowing). *Acta materialia* **2004**, *52* (8), 2461-2474.
109. Esangbedo, C.; Boehman, A. L.; Perez, J. M., Characteristics of diesel engine soot that lead to excessive oil thickening. *Tribology International* **2012**, *47*, 194-203.
110. Bhushan, B., *Introduction to tribology*. John Wiley & Sons: 2013.
111. Dake, L.; Russel, J.; Debrodt, D., A review of DOE ECUT tribology surveys. *Journal of tribology* **1986**, *108* (4), 497-501.
112. Speed, L., Engine oils. *Engine Professional* **2009**, 46-47.

113. Guinther, G. H.; Danner, M. M. *Development of an Engine-Based Catalytic Converter Poisoning Test to Assess the Impact of Volatile ZDDP Decomposition Products from Passenger Car Engine Oils*; 0148-7191; SAE Technical Paper: 2007.
114. Bardasz, E. A., 26 Crankcase Lubricants. *Synthetics, Mineral Oils, and Bio-Based Lubricants: Chemistry and Technology* **2013**, 433.
115. Parekh, K.; Mourhatch, R.; Aswath, P. In *ZDDP-additive-catalyst interactions in engine oil*, World Tribology Congress III, American Society of Mechanical Engineers: 2005; pp 661-662.
116. Hu, J.-Q.; Wei, X.-Y.; Dai, G.-L.; Fei, Y.-W.; Xie, F.; Zong, Z.-M., Tribological behaviors and mechanism of sulfur-and phosphorus-free organic molybdate ester with zinc dialkyldithiophosphate. *Tribology International* **2008**, 41 (6), 549-555.
117. Burchell, T. D., *Carbon materials for advanced technologies*. Elsevier: 1999.
118. Grill, A., Diamond-like carbon: state of the art. *Diamond and related materials* **1999**, 8 (2), 428-434.
119. de Barros' Bouchet, M.; Martin, J.; Le-Mogne, T.; Vacher, B., Boundary lubrication mechanisms of carbon coatings by MoDTC and ZDDP additives. *Tribology International* **2005**, 38 (3), 257-264.
120. Chang, R., *Essential chemistry*. McGraw-Hill Science, Engineering & Mathematics: 1996.
121. Miyoshi, K., *Solid lubrication fundamentals and applications*. CRC Press: 2001.
122. Huang, H.; Tu, J.; Gan, L.; Li, C., An investigation on tribological properties of graphite nanosheets as oil additive. *Wear* **2006**, 261 (2), 140-144.
123. Bill, R. C., Friction and wear of carbon-graphite materials for high-energy brakes. **1978**.
124. Sugishita, J.; Fujiyoshi, S., The effect of cast iron graphite on friction and wear performance III: The lubricating effect of graphite under rolling-sliding contacts. *Wear* **1982**, 77 (2), 181-193.
125. Scharf, T.; Prasad, S., Solid lubricants: a review. *Journal of materials science* **2013**, 48 (2), 511-531.
126. Rabinowicz, E.; Imai, M., Frictional properties of pyrolytic boron nitride and graphite. *Wear* **1964**, 7 (3), 298-300.
127. Savage, R. H., Graphite lubrication. *Journal of applied physics* **1948**, 19 (1), 1-10.
128. Clark, W.; Lancaster, J., Breakdown and surface fatigue of carbons during repeated sliding. *Wear* **1963**, 6 (6), 467-482.

129. Erdemir, A., Design criteria for superlubricity in carbon films and related microstructures. *Tribology International* **2004**, *37* (7), 577-583.
130. Chen, W.; Li, F.; Han, G.; Xia, J.; Wang, L.; Tu, J.; Xu, Z., Tribological behavior of carbon-nanotube-filled PTFE composites. *Tribology Letters* **2003**, *15* (3), 275-278.
131. Lin, J.; Wang, L.; Chen, G., Modification of graphene platelets and their tribological properties as a lubricant additive. *Tribology letters* **2011**, *41* (1), 209-215.
132. Baughman, R. H.; Zakhidov, A. A.; De Heer, W. A., Carbon nanotubes--the route toward applications. *science* **2002**, *297* (5582), 787-792.
133. Grill, A., Review of the tribology of diamond-like carbon. *Wear* **1993**, *168* (1-2), 143-153.
134. Grill, A., Tribology of diamondlike carbon and related materials: an updated review. *Surface and Coatings Technology* **1997**, *94*, 507-513.
135. Ferrari, A. C.; Robertson, J., Raman spectroscopy of amorphous, nanostructured, diamond-like carbon, and nanodiamond. *Philosophical Transactions of the Royal Society of London A: Mathematical, Physical and Engineering Sciences* **2004**, *362* (1824), 2477-2512.
136. Lemoine, P.; Quinn, J.; Maguire, P.; McLaughlin, J., Mechanical characterisation and properties of DLC films. In *Tribology of Diamond-Like Carbon Films*, Springer: 2008; pp 83-101.
137. Chung, Y.-W.; Bhatia, S., Tribological behavior of amorphous carbon nitride overcoats for magnetic thin-film rigid disks. *Journal of Tribology* **1996**, *118*, 543.
138. Kovalchenko, A.; Ajayi, O. O.; Erdemir, A.; Fenske, G. R. *Friction and wear performance of low-friction carbon coatings under oil lubrication*; 0148-7191; SAE Technical Paper: 2002.
139. Singer, I. L.; Dvorak, S. D.; Wahl, K. J.; Scharf, T. W., Role of third bodies in friction and wear of protective coatings. *J. Vac. Sci. Technol. A* **2003**, *21* (5), S232.
140. Bull, S., Tribology of carbon coatings: DLC, diamond and beyond. *Diamond and related materials* **1995**, *4* (5-6), 827-836.
141. Gupta, P. *Iron-Doped Diamond-Like Carbon Coatings (Fe-DLCs): Synthesis, Characterization, and Tribology*. Northwestern University, 2016.
142. Vlad, M.; Szczerek, M.; Michalczewski, R.; Kajdas, C.; Tomastik, C.; Osuch-Słomka, E., The influence of antiwear additive concentration on the tribological behaviour of aC: H: W/steel tribosystem. *Proceedings of the Institution of Mechanical Engineers, Part J: Journal of Engineering Tribology* **2010**, *224* (10), 1079-1089.
143. Hoffman, E. E.; Marks, L. D., Graphitic Carbon Films Across Systems. *Tribology Letters* **2016**, *63* (3), 32.

144. Erdemir, A.; Ramirez, G.; Eryilmaz, O. L.; Narayanan, B.; Liao, Y.; Kamath, G.; Sankaranarayanan, S. K., Carbon-based tribofilms from lubricating oils. *Nature* **2016**, *536* (7614), 67-71.
145. Hsu, S. M.; Gates, R. S., Effect of materials on tribochemical reactions between hydrocarbons and surfaces. *Journal of Physics D: Applied Physics* **2006**, *39* (15), 3128.
146. Erdemir, A. a. E., O., , Tribochemically Driven Diamond-like Carbon Boundary Films from Base Lubricating Oils. *2013 STLE Annual Meeting* **2013**.
147. Gao, F.; Furlong, O.; Kotvis, P.; Tysoe, W., Tribological properties of films formed by the reaction of carbon tetrachloride with iron. *Tribology Letters* **2005**, *20* (2), 171-176.
148. Yu, Y.; Gu, J.; Kang, F.; Kong, X.; Mo, W., Surface restoration induced by lubricant additive of natural minerals. *Applied surface science* **2007**, *253* (18), 7549-7553.
149. Yuansheng, J.; Shenghua, L., Superlubricity of in situ generated protective layer on worn metal surfaces in presence of Mg<sub>6</sub>Si<sub>4</sub>O<sub>10</sub>(OH)<sub>8</sub>. *Superlubricity* **2007**, 447.
150. Yuansheng, J.; Shenghua, L.; Zhengye, Z.; He, Y.; Feng, W., In situ mechanochemical reconditioning of worn ferrous surfaces. *Tribology International* **2004**, *37* (7), 561-567.
151. Blanchet, T.; Lauer, J.; Liew, Y.-F.; Rhee, S.; Sawyer, W., Solid lubrication by decomposition of carbon monoxide and other gases. *Surface and Coatings Technology* **1994**, *68*, 446-452.
152. Yeon, J.; He, X.; Martini, A.; Kim, S. H., Mechanochemistry at solid surfaces: Polymerization of adsorbed molecules by mechanical shear at tribological interfaces. *ACS Applied Materials & Interfaces* **2017**, *9* (3), 3142-3148.
153. He, X.; Barthel, A. J.; Kim, S. H., Tribochemical synthesis of nano-lubricant films from adsorbed molecules at sliding solid interface: Tribo-polymers from  $\alpha$ -pinene, pinane, and n-decane. *Surface Science* **2016**, *648*, 352-359.
154. Yan, J.-H.; Dai, L.-Y.; Wang, X.-Z.; Chen, Y.-Q., Densities and viscosities of binary mixtures of cyclopropanecarboxylic acid with methanol, ethanol, propan-1-ol, and butan-1-ol at different temperatures. *Journal of Chemical & Engineering Data* **2009**, *54* (3), 1147-1152.
155. Faust, R., Fascinating natural and artificial cyclopropane architectures. *Angewandte Chemie International Edition* **2001**, *40* (12), 2251-2253.
156. Wong, H. N.; Hon, M.-Y.; Tse, C. W.; Yip, Y. C.; Tanko, J.; Hudlicky, T., Use of cyclopropanes and their derivatives in organic synthesis. *Chem. Rev* **1989**, *89* (1), 165-198.

157. Engstrom, J.; Goodman, D.; Weinberg, W., Reaction of Cyclopropane, Methylcyclopropane, and Propylene with Hydrogen on the (1 11) and (1 10)-(1 X2) Surfaces of Iridium. *J. Phys. Chem* **1990**, *94*, 396-409.
158. Bhushan, B.; Fuchs, H.; Tomitori, M., *Applied scanning probe methods VIII : scanning probe microscopy techniques*. Springer: Berlin ; New York, 2008; p lix, 465 p.
159. Tabacik, V.; Maillols, J., Vibrational spectra in cyclopropane series—III. Fundamental modes of cyclopropanecarboxylic acid monomer and of its-OD species. *Spectrochimica Acta Part A: Molecular Spectroscopy* **1978**, *34* (3), 315-329.
160. Ng, M.-K.; Fan, Z.; Gao, R. X.; Smith, E. F.; Cao, J., Characterization of electrically-assisted micro-rolling for surface texturing using embedded sensor. *CIRP Annals-Manufacturing Technology* **2014**, *63* (1), 269-272.
161. Kim, D.-W.; Kim, K.-W., Effects of sliding velocity and normal load on friction and wear characteristics of multi-layered diamond-like carbon (DLC) coating prepared by reactive sputtering. *Wear* **2013**, *297* (1), 722-730.
162. Vengudusamy, B.; Mufti, R. A.; Lamb, G. D.; Green, J. H.; Spikes, H. A., Friction properties of DLC/DLC contacts in base oil. *Tribology International* **2011**, *44* (7), 922-932.
163. Erdemir, A.; Eryilmaz, O.; Kim, S., Effect of tribochemistry on lubricity of DLC films in hydrogen. *Surface and Coatings Technology* **2014**, *257*, 241-246.
164. Field, S.; Jarratt, M.; Teer, D., Tribological properties of graphite-like and diamond-like carbon coatings. *Tribology International* **2004**, *37* (11), 949-956.
165. Steiner, L.; Bouvier, V.; May, U.; Hegadekatte, V.; Huber, N., Modelling of unlubricated oscillating sliding wear of DLC-coatings considering surface topography, oxidation and graphitisation. *Wear* **2010**, *268* (9), 1184-1194.
166. Wang, Y.; Wang, Q. J.; Lin, C.; Shi, F., Development of a set of Stribeck curves for conformal contacts of rough surfaces. *Tribology transactions* **2006**, *49* (4), 526-535.
167. Haque, T.; Morina, A.; Neville, A.; Kapadia, R.; Arrowsmith, S., Effect of oil additives on the durability of hydrogenated DLC coating under boundary lubrication conditions. *Wear* **2009**, *266* (1), 147-157.
168. Hisakado, T.; Tsukizoe, T.; Yoshikawa, H., Lubrication mechanism of solid lubricants in oils. *ASME, Transactions, Journal of Lubrication Technology (ISSN 0022-2305)* **1983**, *105*, 245-252.
169. Lancaster, J. K., Instabilities in the frictional behaviour of carbons and graphites. *Wear* **1975**, *34* (3), 275-290.

170. Romero, P. A.; Pastewka, L.; Von Lautz, J.; Moseler, M., Surface passivation and boundary lubrication of self-mated tetrahedral amorphous carbon asperities under extreme tribological conditions. *Friction* **2014**, *2* (2), 193-208.
171. Liu, Y.; Erdemir, A.; Meletis, E., A study of the wear mechanism of diamond-like carbon films. *Surface and Coatings Technology* **1996**, *82* (1-2), 48-56.
172. Liu, Y.; Erdemir, A.; Meletis, E., An investigation of the relationship between graphitization and frictional behavior of DLC coatings. *Surface and Coatings Technology* **1996**, *86*, 564-568.
173. Liu, Y. B.; Lim, S. C.; Ray, S.; Rohatgi, P. K., Friction and wear of aluminium-graphite composites: the smearing process of graphite during sliding. *Wear* **1992**, *159* (2), 201-205.
174. Whitehead, A. J.; Page, T. F., Nanoindentation studies of thin film coated systems. *Thin solid films* **1992**, *220* (1-2), 277-283.
175. Ferrari, A. C.; Robertson, J., Interpretation of Raman spectra of disordered and amorphous carbon. *Physical Review B* **2000**, *61* (20), 14095-14107.
176. Farrow, R.; Benner, R.; Nagelberg, A.; Mattern, P., Characterization of surface oxides by Raman spectroscopy. *Thin Solid Films* **1980**, *73* (2), 353-358.
177. Furlong, O.; Gao, F.; Kotvis, P.; Tysoe, W., Understanding the tribological chemistry of chlorine-, sulfur- and phosphorus-containing additives. *Tribology international* **2007**, *40* (5), 699-708.
178. Lara, J.; Surerus, K.; Kotvis, P.; Contreras, M.; Rico, J.; Tysoe, W., The surface and tribological chemistry of carbon disulfide as an extreme-pressure additive. *Wear* **2000**, *239* (1), 77-82.
179. Spikes, H.; Tysoe, W., On the commonality between theoretical models for fluid and solid friction, wear and tribochemistry. *Tribology Letters* **2015**, *59* (1), 21.
180. Tysoe, W., On Stress-Induced Tribochemical Reaction Rates. *Tribology Letters* **2017**, *65* (2), 48.
181. Hirani, H., *Fundamentals of Engineering Tribology with applications*. Cambridge University Press: 2016.
182. Anslyn, E. V.; Dougherty, D. A., *Modern physical organic chemistry*. University Science Books: 2006.
183. Steele, W.; Chirico, R.; Knipmeyer, S.; Nguyen, A., Measurements of vapor pressure, heat capacity, and density along the saturation line for  $\epsilon$ -caprolactam, pyrazine, 1, 2-propanediol,

triethylene glycol, phenyl acetylene, and diphenyl acetylene. *Journal of Chemical & Engineering Data* **2002**, 47 (4), 689-699.

## **Author Vita**

### **Blake Johnson**

Email | blakejohnson424@gmail.com

### **EDUCATION**

PhD in Mechanical Engineering, Northwestern University, 2014-2017

MS in Mechanical Engineering, Northwestern University, 2012-2014

BS in Mechanical Engineering, University of Texas at Austin, 2008-2012

### **WORK EXPERIENCE**

Test Engineer, BASF Corporation, 2017

Lab Manager, Northwestern University, 2012-2017

Mechanical Engineer, Intel Corporation, 2012

Test Engineer, Lineage Power, 2008

Tutor, University of Texas, 2009-2010

### **RESEARCH EXPERIENCE**

Center for Surface Engineering & Tribology, Northwestern University, 2012-2017

Polymer Nanocomposite Research Group, University of Texas, 2011-2012

Honors Capstone Design Program, University of Texas, 2011-2012

### **AWARDS**

DAAD RISE Professional Scholarship Recipient, 2017

BASF Science Competition, 1st Place, 2016

NSF Graduate Research Fellowship, Honorable Mention, 2014

Northwestern University PSED Fellow, 2014

### **INVOLVEMENT**

Society of Tribologists and Lubrication Engineers

Mechanical Engineering Graduate School Society, Northwestern University

SAMPE, Vice President, University of Texas

Pi Tau Sigma Mechanical Engineering Honors Society

**PUBLICATIONS**

Johnson, B; Wu, H; Desanker, M; Pickens, D; Wang, Q J; Chung, Y W, Direct Formation of Lubricious and Wear-Protective Carbon Films from Phosphorus- and Sulfur-Free Oil-Soluble Additives, *Tribology Letters* 2017, (Accepted for publication).

Desanker, M; He, X; Lu, J; Johnson, B; Liu, Z; Delferro, M; Ning, Ren; Lockwood, F; Greco, A; Erdemir, A; Marks, T; Wang, Q; Chung, YW, High-Performance Heterocyclic Friction Modifiers for Boundary Lubrication, *Tribology Letters* 2017, (Under review for publication).

Wu, H; Johnson, B; Wang, L; Dong, G; Yang, S; Zhang, J, High-efficiency preparation of oil-dispersible MoS<sub>2</sub> nanosheets with superior anti-wear property in ultralow concentration, *Journal of Nanoparticle Research* 2017, 19 (10), 339.

Wu, H; Wang, L; Johnson, B; Yang, S; Zhang, J; Dong, G, Investigation on the lubrication advantages of MoS<sub>2</sub> nanosheets compared with ZDDP using block-on-ring tests, *Wear* 2017, 394-395, 40-49.

Desanker\*, M; Johnson\*, B; Seyam, A M; Chung, YW; Bazzi, H S; Delferro, M; Marks, T J; Wang, Q J, Oil-Soluble Silver–Organic Molecule for in Situ Deposition of Lubricious Metallic Silver at High Temperatures, *ACS Applied Materials & Interfaces* 2016, 8 (21), 13637-13645. (\* co-first authors)

Koo, J H; Pinero, D; Hao, A; Lao, S C; Johnson, B; Baek, M G; Lee, J; Pilato, L, Methodology for Assessment of Morphological and Thermal Characteristics of Nanographene Platelets, *The American Institute of Aeronautics and Astronautics* 2013, 1548, 1-35.

## PRESENTATIONS

Johnson, B., Pickens, D., Chung, Y. W., and Wang, Q., "A Cycloalkane-based Lubricant Additive for the Formation of Lubricious Carbon Tribofilms," Poster presentation at the 2016 STLE Annual Meeting, Las Vegas.

Johnson, B., Chung, Y. W., and Wang, Q., "Lubricant Additive for In Situ Formation of Lubricious Carbon," Presented at the 2015 Tribology Frontiers Conference, Denver

He, X., Desanker, M., Lu, J., Johnson, B., Lockwood, F., Ren, N., Chung, Y. W., Marks, T. J., and Wang, Q., "Novel Heterocyclic Friction Modifiers for Boundary Lubrication," Presented at the 2015 STLE Annual Meeting, Dallas

Johnson, B., Desanker, M., Delferro, M., Shu, D., Seyam, A., Bazzi, H., Twist, C., Chung, Y. W., Marks, T. J., and Wang, Q., "An Organo-Silane Lubricant Additive for Mitigation of Sand Particle Contamination," Presented at the 2014 Tribology Frontiers Conference, Chicago.

Johnson, B., He, H., Jin, D., Liu, J., Desanker, M., Song, C., Greco, A., Delferro, M., Erdemir, A., Chung, Y. W., Marks, T. J., and Wang, Q., "Novel Friction Modifiers for Steel Contact," Presented at the 2014 Tribology Frontiers Conference, Chicago.

## PATENTS

Marks, T. J., Delferro, M., Wang, Q., Chung, Y. W., Bazzi, H. S., Seyam, A. B., Desanker, M., Johnson, B., Jin, D., Oil Soluble Organo-Silver Materials as High-Temperature Lubricant Additives, in process, US Patent Appl. 15/013, 8780.

Chung, Y. W., Johnson, B., and Wang, Q., Lubricant Additives, Lubricant Compositions, and Applications of Same, in process, PCT/US2015/056965.